Journal of Modeling & Simulation in Electrical & Electronics Engineering (MSEEE)

Semnan University

Volume 6, Issue 1 - Serial Number 23, March 2026, Pages 1-65

Contents

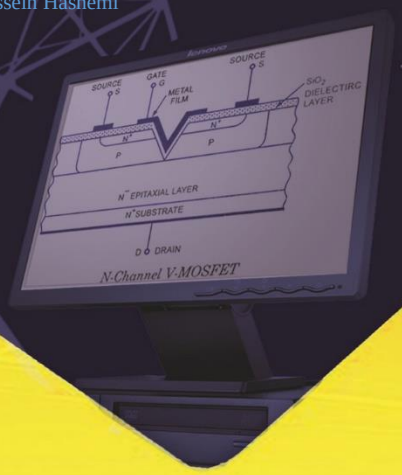

- **Frequency** Quarterly
- **Online ISSN** 2821-0786

Volume 6, Issue 1 - Serial Number 23, March 2026, Pages 1-65

Contents

Semnan University

Journal of Modeling & Simulation in Electrical & Electronics Engineering (MSEEE)

Journal homepage: **https://mseee.semnan.ac.ir/**

ISSN: 2821-0786

A Peer-to-Peer Energy Trading Optimization for Peak Load Management in Energy Internet Systems

Leila Mohammadian [1]

***Abstract*--The convergence of widespread renewable energy sources (RES) and Internet of Things (IoT) technologies has catalyzed the development of the Energy Internet (EI), enabling advanced energy management paradigms. The EI framework facilitates the integration of numerous distributed generation units and leverages digital intelligence to enhance energy sharing, optimize grid asset utilization, and bolster overall power system security. Concurrently, rapid socio-economic growth has intensified global energy demand, leading to periodic shortages that challenge grid reliability. These scarcity conditions are predominantly manifested during peak load periods of the system. Consequently, a significant body of research is dedicated to peak load shifting and shaving to mitigate this issue. Nevertheless, few studies have systematically exploited the full capabilities of the EI framework to achieve this critical objective. This research, therefore, aims to develop and propose an EI-based optimization problem specifically designed to solve the peak load shifting problem with the primary goal of minimizing total system cost. The proposed methodology achieves this by optimizing the scheduled charging and discharging cycles of end-user Energy Storage Systems (ESS). Within this formulated problem, each prosumer—an entity that is both a consumer and a potential supplier—participates in a localized energy market. The operational cost model must comprehensively account for the costs of power sourced from the conventional grid and local RES, the storage dynamics within the ESS, and the accurate application of Real-Time Pricing (RTP) signals to all generated and consumed energy.**

***Index Terms*- Energy Internet, Energy Storage System, Peak Load Shifting, Prosumer, Real-Time Pricing.**

TABLE I
Abbreviations

Abbreviation	Full Term
EI	Energy Internet
RES	Renewable Energy Sources
IoT	Internet of Things
ESS / BESS	(Battery) Energy Storage System
DSM	Demand-Side Management
RTP	Real-Time Pricing
P2P	Peer-to-Peer
PV	Photovoltaic
PCS	Power Conversion System
BOP	Balance of Plant
MIP	Mixed-Integer Programming
SPM	Smart Polygeneration Microgrid
SEB	Smart Energy Building
PAR	Peak-to-Average Ratio

I. INTRODUCTION

THE Modern power systems stand on the brink of a historic transformation. The rapid increase in energy demand, growing environmental concerns, and the imperative to enhance reliability have created unprecedented challenges [1]. These challenges necessitate a fundamental transition from traditional, centralized, and passive generation paradigms toward the utilization of distributed and renewable resources within an integrated, intelligent system framework [2-3]. In this context, significant advancements in the IoT and renewable energy sources have catalyzed the emergence of a new paradigm: the EI [4-5].

Received; 2025-10-29 Revised; 2025-12-28 Accepted; 2026-01-06

1. Department of Electrical Engineering, Shab.C., Islamic Azad University, Shabestar, Iran.
*Corresponding author: le.mohammadian@iau.ac.ir

Cite this article as:
Mohammadian, L. (2026). A Peer-to-Peer Energy Trading Optimization for Peak Load Management in Energy Internet Systems. *Journal of Modeling & Simulation in Electrical & Electronics Engineering (MSEEE)*. Semnan University Press . 6 (1), 1-11.
DOI: https://doi.org/10.22075/MSEEE.2026.39530.1234

Within the EI framework, all components of the energy system—from large-scale generators and microgrids to end-users and distributed energy storage units—are interconnected via digital platforms [6]-[7]. This connectivity enables intelligent, integrated, and real-time management of energy production, storage, distribution, and consumption [8]. The primary goals of the EI are to increase energy utilization efficiency, facilitate the widespread and secure integration of renewables, and ultimately establish a resilient, sustainable, and efficient energy system [9]-[10]. In this transformed energy landscape, IoT technology, with its capability for large-scale, real-time data collection, processing, and exchange, serves as the backbone [11]. One of the most pressing challenges in contemporary power systems is the phenomenon of "peak load." Energy shortages, particularly during peak hours, can occur due to total demand exceeding available generation capacity, outages of generation units, or fuel shortages in conventional power plants [12]. This issue not only threatens grid reliability but also drastically increases operational costs [13]. In this regard, the "peak load shifting" strategy is recognized as an effective solution to alleviate grid stress during peak hours and enhance system stability [14]-[15].

This research aims to propose a comprehensive framework within the EI to address the peak load shifting problem. The proposed model integrates active participation from end-users (who can act as prosumers), distributed battery energy storage systems, and renewable sources, while employing a real-time pricing mechanism. Its objective is to minimize the total energy cost for consumers and optimize the charging and discharging scheduling of storage units.

Numerous studies have investigated various strategies for demand management and peak load shifting, primarily focusing on Demand-Side Management (DSM), RTP, and the deployment of BESS. The theoretical foundations and benefits of DSM have been extensively explored in the literature [16]-[17]. At the end-user level, studies such as [18] have focused on reducing energy consumption and prioritizing power scheduling to achieve load shifting. Ref. [19] has integrated residential electricity management with solar power generation units. In [20], the use of smart meters and small-scale storage units in homes encouraged users to manage their energy consumption. The development of intelligent controllers based on neural networks for coordinating distributed energy resources and household appliances represents a further step in optimizing building energy use [21].

Dynamic price signals are recognized as a key driver for modifying consumer behavior [22]. Research [23] introduced an energy system based on real-time pricing for the automatic adjustment of user consumption. Study [24] also integrated smart grids and electric vehicles using optimization models to reduce grid operational costs. Realistic demand response models have been developed for effective market interaction [25-26].

The use of BESS has also received significant attention. This includes BESS scheduling in competitive markets [27] and power management in grid-connected systems with PV and batteries [28]. For instance, [29] utilized BESS to store energy during low-load conditions and supply power during peak demand, thereby improving grid reliability. In [30], a mathematical model for BESS was presented that can smooth load variations. Considerations related to battery lifecycle characteristics have also been addressed in the optimization of isolated power systems [31]. Study [32] further demonstrated how BESS can maximize profit for its owners by storing energy during low-price periods and selling it when prices are high.

Various optimization techniques, including Artificial Intelligence [33], Evolutionary Algorithms [34-35], as well as Robust [36] and Stochastic [37-38] approaches, have been employed to manage uncertainty in power systems. These methods provide a solid foundation for developing energy management models in complex environments. Furthermore, concepts such as Networked Microgrids [39] and business models for microgrid aggregators [40] have opened new horizons for optimized energy management .As evident from the literature review, a significant research gap exists in the simultaneous integration of these three strategies (DSM, RTP, BESS) within a unified, decentralized EI framework. Most studies have focused on only one or two aspects, often overlooking the active and bidirectional role of end-users in a dynamic energy market. By addressing this gap, this paper proposes a comprehensive optimization problem where end-users can trade energy with one another and the grid within an intelligent platform influenced by real-time price signals.

While the existing body of work provides robust foundations in DSM, RTP-based mechanisms, and BESS scheduling, a critical synthesis within a fully decentralized EI framework is lacking. Studies such as [19] and [21] optimize building-level energy use with local RES but do not integrate a dynamic P2P market. Research like [27] and [32] focuses on BESS arbitrage in wholesale markets, often neglecting the proactive role of prosumers at the distribution level. Furthermore, models incorporating RTP [23]-[24] typically treat consumers as price-takers rather than proactive traders. This paper bridges these gaps by proposing a holistic optimization model that simultaneously integrates: (1) a prosumer-centric P2P energy market, (2) RTP-driven DSM, and (3) coordinated BESS scheduling—all within a unified EI architecture. The proposed formulation distinctively models the complete cost structure for prosumers (grid purchase, RES generation, ESS capital/maintenance). It enforces operational constraints based on real-time market signals, enabling a more realistic assessment of peak shaving and cost-saving potentials.

To validate the proposed optimization problem, a series of numerical simulations was conducted. The results demonstrate a significant reduction in the system's peak-to-average ratio, confirming the method's efficacy in flattening the load profile. Furthermore, the proposed energy trading mechanism among prosumers results in a measurable decrease in their aggregate electricity costs, while also enhancing the utilization rate of distributed renewable energy within the network.

The structure of this paper is as follows: Following the introduction, Section 2 provides a literature review and a precise problem statement. Section 3 is dedicated to detailing the problem formulation and the mathematical model. The simulation environment and obtained results are presented and analyzed in Section 4. Finally, Section 5 offers conclusions and suggestions for future research.

II. Problem Formulation & Mathematical Model

The proposed EI framework is illustrated in Fig. 1. In this model, energy is conceptualized as a tradable commodity whose price is dynamically determined by real-time market demand. This establishes a direct correlation where peak demand periods correspond to the highest energy prices, whereas the lowest prices occur during off-peak periods.

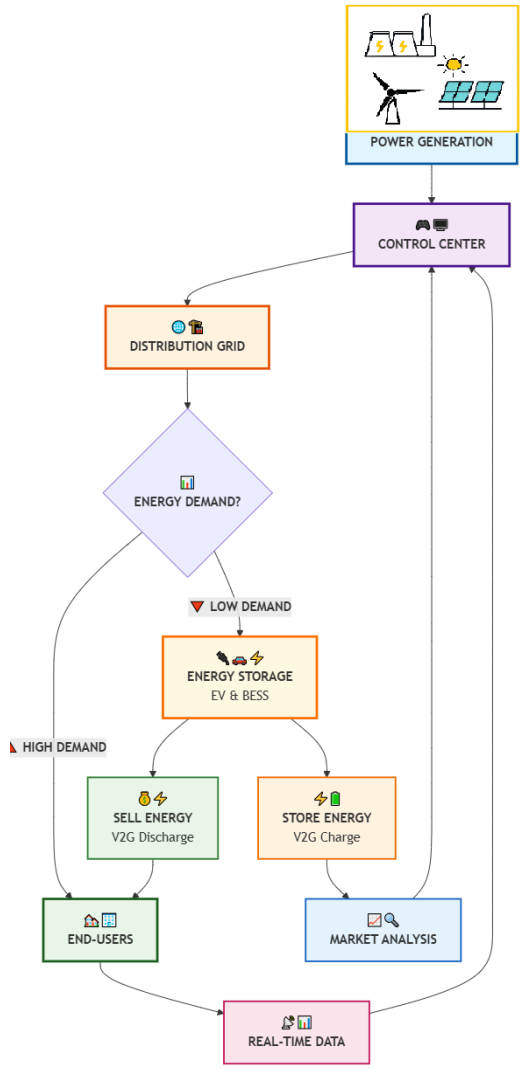

Fig 1. The EI framework

Within the EI network, user demand is accurately quantified through smart metering infrastructure, with this data transmitted to a central control center. This system enables a more realistic and granular representation of load patterns. The control center is then responsible for dispatching energy based on the aggregated requested load.

A key feature of this framework is its bidirectional communication capability. The control center's dispatch logic, detailed in Fig. 2, moves beyond simple price thresholds to incorporate both economic and grid-stability signals.

Fig. 2(a) illustrates the charging logic. The control center continuously monitors real-time load $L(t)$ and price $RTP(t)$. A charging signal is broadcast to prosumers only when two concurrent conditions are met: (1) The $RTP(t)$ is at or below a dynamic charging threshold $T_{ch}(t)$, and (2) The grid load $L(t)$ is below the daily average load L^{-}. This prevents charging from exacerbating grid stress during periods of low price but high absolute demand. The primary threshold is $T_{ch}(t) = RTP_{min}^{i-1} + \gamma\Delta_{i-1}$. To ensure robustness during periods of low price volatility (e.g., $\Delta_{i-1} \approx 0$), a fallback mechanism is implemented. If Δ_{i-1} is below a defined minimum (e.g., 5% of RTP_{min}^{i-1}), the system defaults to a secondary threshold based on a rolling 7-day average RTP, maintaining system responsiveness.

Fig. 2(b) outlines the discharging logic. Discharge is triggered when the grid load $L(t)$ exceeds L^{-} and the $RTP(t)$ surpasses a dynamic discharging threshold $T_{dis}(t) = RTP_{min}^{i-1} + \beta\Delta_{i-1}$, where $\beta > \gamma$ (e.g., $\beta = 0.8$). This ensures prosumers capitalize on high prices while directly contributing to peak shaving. Upon receiving the signal, prosumers schedule energy injection from their BESS, either to the grid or to other consumers via the P2P market.

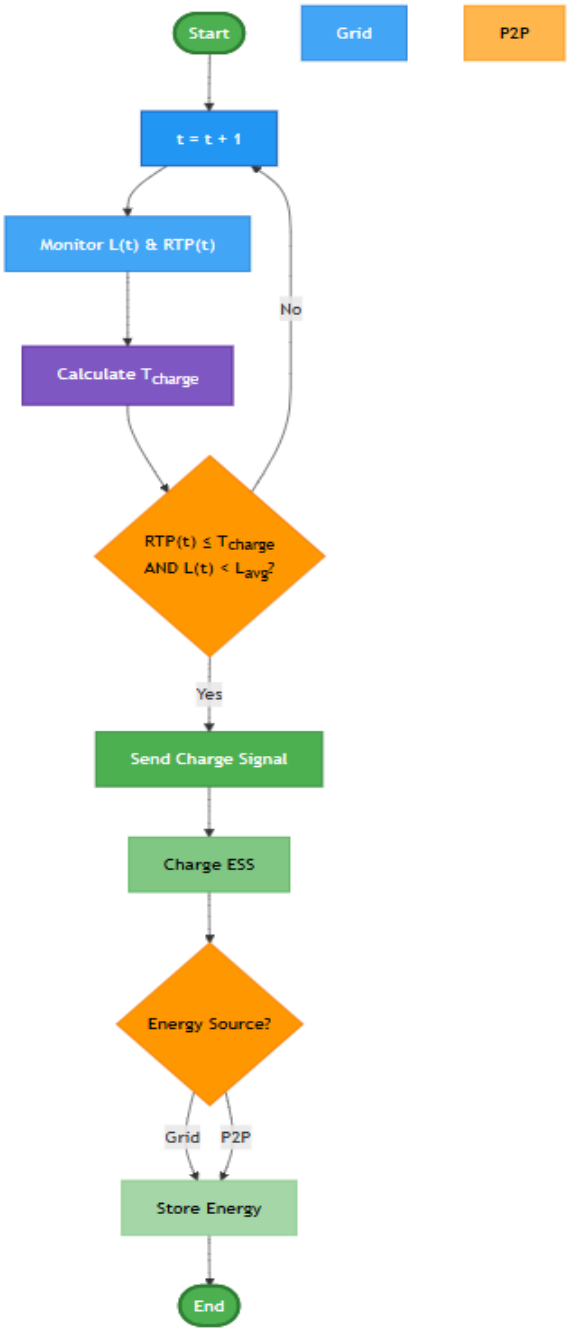

(a)

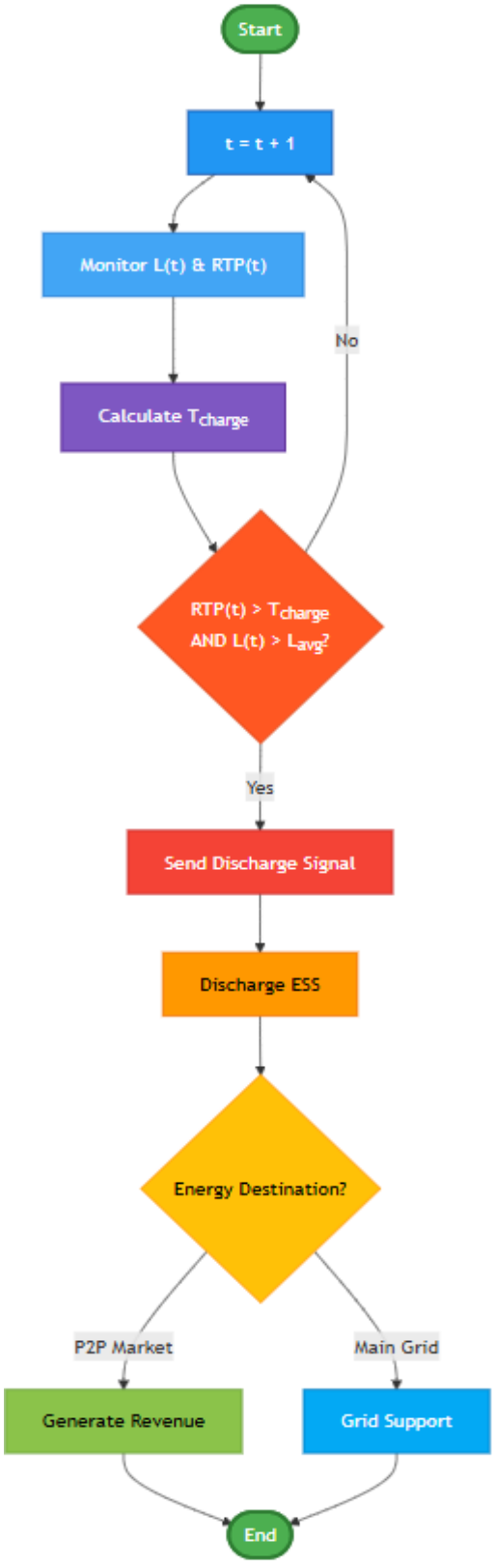

(b)

Fig 2. Decision flowcharts for the proposed energy management strategy: (a) ESS charging mode, (b) ESS discharging mode.

This section presents the mathematical formulation for the load shifting problem introduced previously. The investigation focuses on peak load management within the EI framework, incorporating a novel peer-to-peer energy market among end-users—a distinctive feature that is not comprehensively addressed in the existing literature.

The proposed model employs a comprehensive, system-wide approach that integrates the complete generation portfolio with all consumption nodes. The proposed formulation includes the base foundation, incorporating the charging dynamics of energy storage systems from renewable sources—specifically, wind and PV generation.

Furthermore, the model establishes and analyzes the synergistic relationship between the Energy Internet infrastructure and distributed energy storage resources for managing energy from the main grid, wind turbines, and solar PV installations. Table II brings all the parameters needed in this research.

TABLE II
Simulation Parameters

Parameter	Definition
C_{grid}	The total cost of energy procured from the main grid by all consumers
C_m	Aggregate capital and maintenance cost of consumer-owned energy storage systems
C_{res}	levelized cost of energy from consumer-owned renewable generation assets
B_{store}	A revenue stream from energy arbitrage via storage system participation in market operations.
i	Index of the day under analysis
t	Time index
$RTP_i(t)$	RTP at hour *t* of the *i*th day
$RTP_{\min}^{i-1}$	Minimum RTP on the previous day
$RTP_{\max}^{i-1}$	Maximum RTP on the previous day
Δ_{i-1}	Maximum RTP variation on the previous day
γ	Parameter indicating the peak-to-off-peak load ratio
$E_{store}^{\max}$	Maximum capacity of energy storage devices
P_{PCS}^{u}	Unit price of PCS (Power Conversion System)
P_{Store}^{u}	Unit price of energy storage
P_{BOP}^{u}	Unit price of BOP (Balance of Plant)
P	Energy capacity of PCS and BOP
C_{wind}	Cost of generated wind energy
C_{pv}	Cost of generated PV energy
E_{store}	Total energy stored in energy storage devices
μ	Charge/discharge efficiency of energy storage devices
$E_{wind,t}$	The amount of wind energy stored in the energy storage
E_{PV}	Amount of PV energy stored in the energy storage
E_{grid}	Amount of grid energy stored in the energy storage
M_{wind}	Daily maintenance cost of the wind turbine generator
M_{PV}	Daily maintenance cost per unit area of solar energy equipment
$E_L^i(t)$	Grid energy consumed by users at hour *t* of the *i*th day
$E_{ES,t}$	Grid energy used by users for charging at hour *t* of the *i*th day
Decision Variable	
$\delta_{grid,t}$	Binary parameter indicating whether a user charges using grid energy at hour *t*

The core objective function is formulated to minimize the total daily energy cost for all users, expressed as follows:

$$\text{Minimize} \quad C_{grid} + C_m + C_{res} - B_{store} \tag{1}$$

It is noteworthy that wind and photovoltaic generation can be either directly consumed or stored for later use. Consequently, storage systems are prohibited from grid charging during peak load intervals to prevent network congestion.

The complete optimization framework is subject to constraints defined in equations (2), (5), (6), and (9). The grid energy cost component is formulated as:

$$C_{grid} = \sum_{t=1}^{24} RTP_i(i).E_L^i(t) + \sum_{t=1}^{24} RTP_i(i).E_{ES,t}^i(t).\delta_{grid,t} \tag{2}$$

The first term represents the cost of energy directly consumed from the grid, while the second term quantifies the cost of grid energy used specifically for storage charging. $\delta_{grid,t}$ is a binary decision variable that specifies the charging process from the grid as follows:

$$\delta_{grid,t} = \begin{cases} 1, \ if \ \ RTP_i(t) \le RTP_{\min}^{i-1} + \gamma.\Delta_{i-1} \\ 0, \ otherwise \end{cases} \tag{3}$$

The storage system cost is modeled as:

$$C_m = P_{PCS}^u.P + P_{store}^u.E_{store} + P_{BOP}^u.P \tag{4}$$

This encompasses:

- Power Conversion System (PCS) capital cost
- Energy storage medium cost
- Balance of Plant (BOP) components cost, where P denotes the power rating (kW) and E_{store} the energy capacity (Wh).

The price threshold for peak/off-peak classification is derived from:

$$\Delta_{i-1} = RTP_{\max}^{i-1} - RTP_{\min}^{i-1} \tag{5}$$

Peak load conditions are identified when $RTP_i(t) > RTP_{\min}^{i-1} + \gamma$, prohibiting storage charging. The parameter $\gamma \in [0,1]$ determines the peak load duration.

Renewable energy costs are separated as:

$$C_{res} = C_{wind} + C_{pv} = M_{wind}.N + M_{PV}.S_{PV} \tag{6}$$

representing operational expenditures for wind (N turbines) and solar (SPV area) assets.

Storage revenue from energy arbitrage is calculated as:

$$B_{store} = \sum_{t=1}^{24} \left[RTP_i(t).E_{store}(t).(1-\delta_{grid,i}(t)).\mu \right] \tag{7}$$

Where μ represents round-trip efficiency.

The total stored energy is constrained by:

$$E_{store} = E_{grid} + \sum_{t=1}^{24} E_{wind,t} + E_{PV} \le E_{store}^{\max} \tag{8}$$

$$E_{store} = \sum_{t=1}^{24} E_{ES,t}^i + \sum_{n=1}^{N} f_n(v_t) + S_{pv}.\eta_{pv}.p_f.\eta_{pc}.G_t \tag{9}$$

with renewable contributions calculated using established power curve and solar radiation models.

Key differentiators from prior research include:

- Comprehensive cost modeling encompassing all consumer energy resources
- Explicit incorporation of renewable energy generation costs
- Integration of real-time pricing mechanisms within the Energy Internet architecture
- Advanced storage operational constraints based on market signals
- Holistic energy balance considering both grid and renewable sources

III. Simulation Results

A comprehensive numerical analysis is conducted to validate the proposed mathematical framework. This section first details the simulation environment and dataset generation methodology, followed by a systematic analysis of the obtained results

The model was validated using operational data from the Savona Campus microgrid, incorporating smart energy building and smart polygeneration microgrid infrastructures with hybrid renewable-storage systems.

Key simulation parameters are summarized in Table III.

TABLE III
Simulation Parameter settings

Parameter	Value	Unit
Charging/discharging efficiency of energy storage facilities (μ)	85	%
Unit price of PCS, P_{PCS}^u	256	€/kW
Unit price of energy storage, P_{Store}^u	171	€/kWh
Unit price of BOP, P_{BOP}^u	53	€/kW
Highest previous day RTP, $RTP_{\max}^{i-1}$	141	€/MWh
Lowest previous day RTP, $RTP_{\min}^{i-1}$	67	€/MWh
Peak identification parameter (γ)	0.25, 0.5, 0.75	-
Discharge trigger parameter (β)	0.8	-
Max storage capacity (E_{max})	141	kWh
Wind turbine daily maintenance cost (M_{wind})	10	€/turbine
PV daily maintenance cost per unit area (M_{PV})	0.5	€/m²

A comprehensive numerical analysis is conducted to validate the proposed mathematical framework. This section first details the simulation environment and dataset generation methodology, followed by a systematic study of the obtained results.

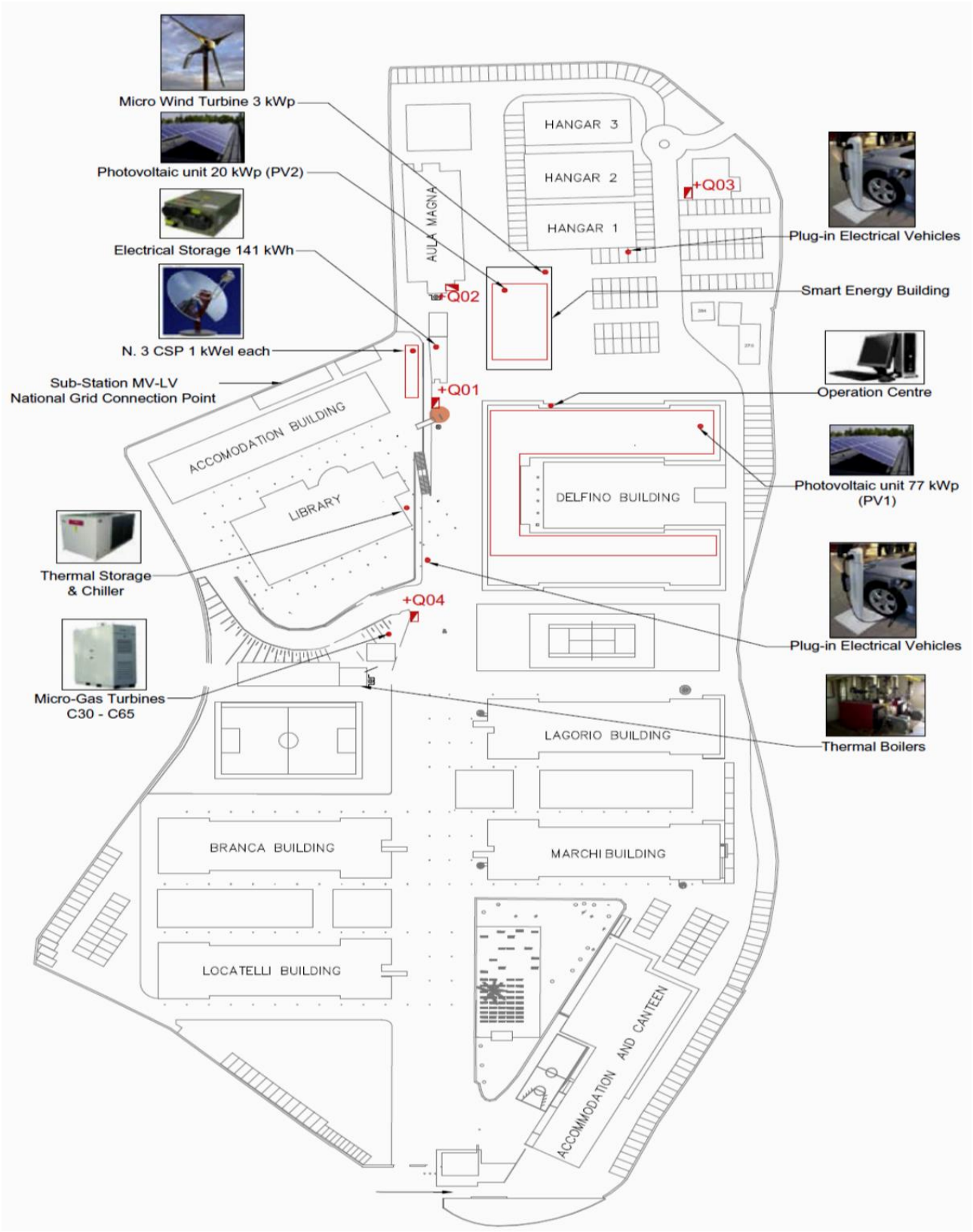

Fig. 3. Campus layout map and SPM and SEB equipment

A. *Performance Analysis*

Within the Energy Internet framework, the control center receives real-time data streams from both consumption nodes and generation assets to optimize energy dispatch decisions. Distributed energy storage systems continuously monitor local demand patterns and renewable generation availability to support operational planning.

The simulation employs the following dataset configurations, derived from the Savona Campus microgrid:

- **Load Profile**: Fig. 4 illustrates the 24-hour load profile for the end-user community, exhibiting characteristic diurnal patterns with elevated demand during daytime operational hours. The profile shows significantly higher consumption during 06:00-17:00, coinciding with commercial and industrial activity periods, while nighttime hours (03:00 and 18:00-24:00) demonstrate substantially reduced demand. A

pronounced peak demand of 1,376 kWh occurs at hour 17:00, representing the critical target for load shifting interventions. This consumption pattern provides essential baseline data for optimizing storage system dispatch strategies and evaluating the effectiveness of peak shaving methodologies within the proposed Energy Internet framework.

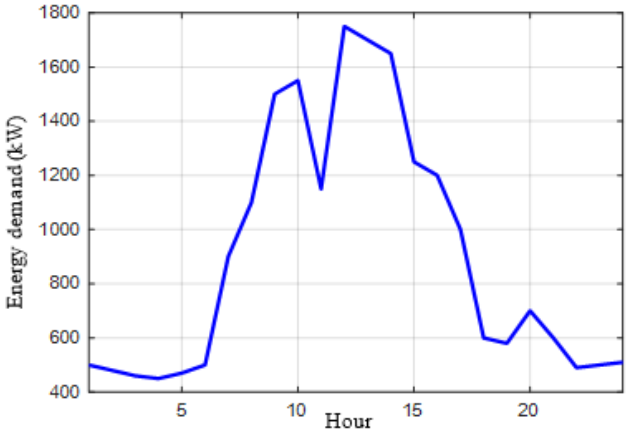

Fig. 4. The energy demand of end-users in 24 hours of one day.

- **Renewable Generation** (Fig. 5): Combined output from Smart Polygeneration Microgrid (SPM) and Smart Energy Building (SEB) assets, featuring time-varying generation profiles influenced by meteorological conditions.

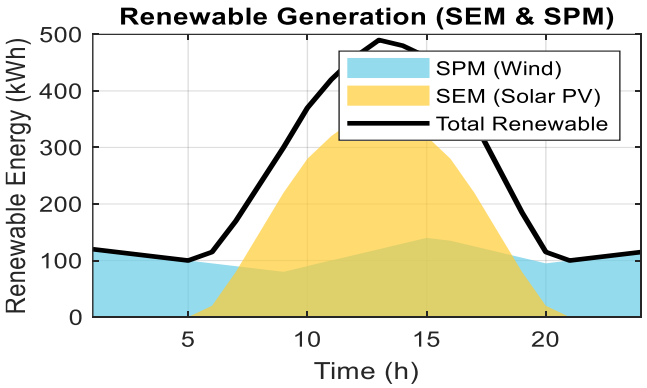

Fig. 5. Daily renewable energy generations for SPM and SEM

- **Price Signals** (Fig. 6): The real-time pricing trajectory reflects market dynamics, with maximum prices occurring at hour 11:00 and minimum prices at hour 03:00, corresponding to system demand patterns.

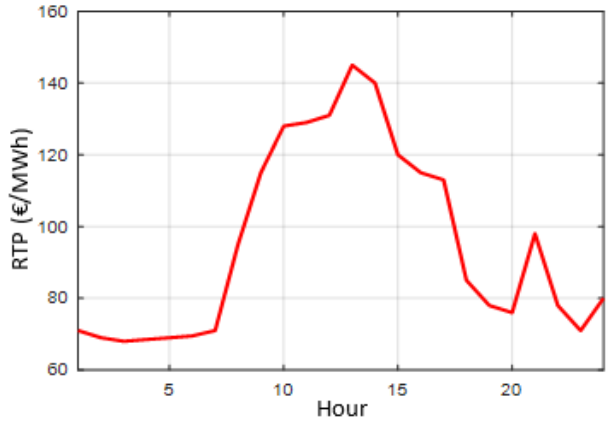

Fig. 6. The RTPs of 24 hours of one day in the energy trading market.

For economic analysis, the aggregate daily renewable generation cost is established at $1,640, based on infrastructure specifications from reference [13], providing a baseline for cost-benefit assessment of storage operations.

The proposed optimization problem is formulated as a Mixed-Integer Programming (MIP) model, which is solved using the optimization toolbox in MATLAB software. To analyze the sensitivity of system performance to peak load identification, parametric studies were conducted for different values of γ, which determines the threshold for peak/off-peak period classification.

The total system cost demonstrates a decreasing trend with increasing γ values. This relationship emerges because higher γ values narrow the classification window for peak load periods, thereby expanding the temporal flexibility for storage charging during lower-cost intervals. Consequently, the optimization algorithm can leverage extended off-peak durations to minimize energy procurement costs while maintaining effective peak shaving capability through strategic discharge scheduling.

The parameter γ directly influences storage operational patterns by governing the charging schedule, state-of-charge levels, and discharge timing during peak conditions. This systematic variation enables the identification of optimal trade-offs between capital utilization of storage assets and energy arbitrage benefits.

Fig. 7 illustrates the charge-discharge patterns of energy storage systems across three γ values (0.65, 0.70, 0.75), where binary states represent discharging (0) and charging (1) operations. The analysis reveals an inverse relationship between γ values and charging duration, with higher γ parameters resulting in compressed charging windows. This occurs because elevated γ thresholds classify fewer hours as peak periods, consequently expanding the operational flexibility for storage charging during off-peak conditions. So, Fig. 7 reveals reduced charging durations with increasing γ, effectively shifting peak loads.

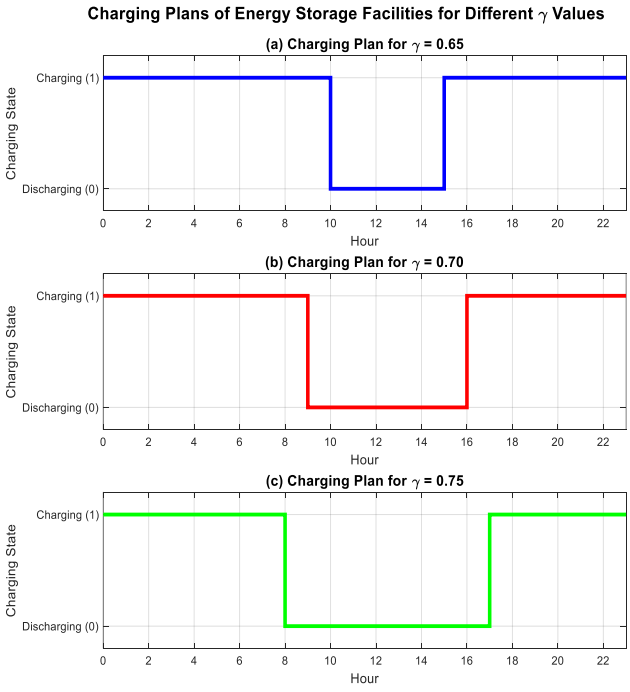

Fig. 7. The charging plans of energy storage facilities in 24 hours when γ = 0.65, 0.70, and 0.75, respectively

The load shifting effectiveness is quantitatively demonstrated in Fig. 8 for $\gamma = 0.65$. The optimized operational strategy employs storage discharge during peak hours (10:00-15:00), successfully reducing the original peak load of 1,376 kWh to 1,406 kWh. Concurrently, strategic charging during off-peak hours elevates the minimum load from 392 kWh to 819 kWh, effectively flattening the load profile. The implemented peak shaving strategy achieves a significant reduction in peak-to-average ratio, with total energy loss decreasing from 1,376 kWh to 868 kWh, representing a 37% improvement in load factor efficiency.

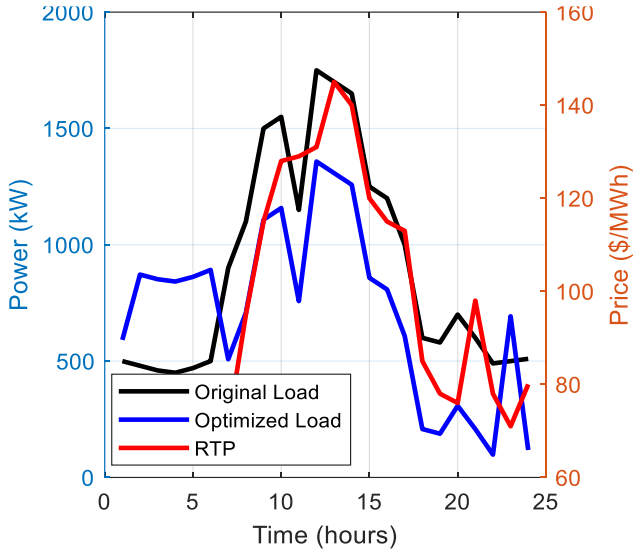

(a)

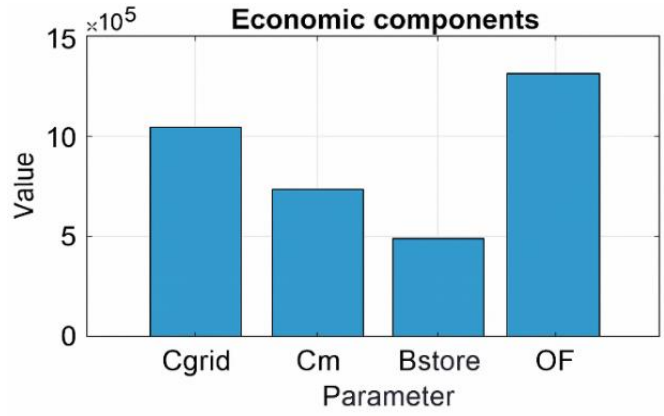

(b)

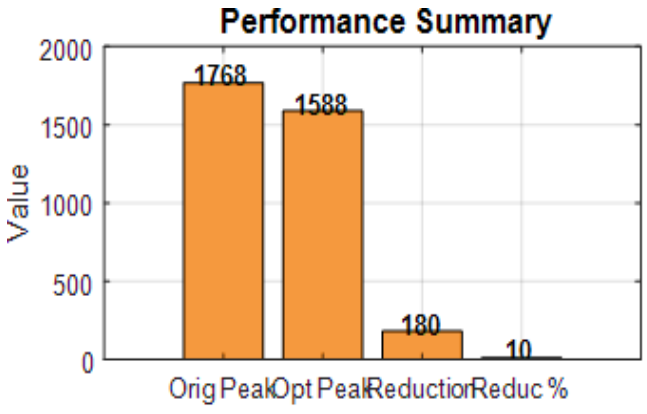

(c)

Fig. 8. (a) The best peak load shifting of energy storage in comparison with the original energy demand and RTP, (b) Economic components of the problem, (c) Proposed optimization performance summary

This operational paradigm demonstrates how coordinated storage dispatch within the EI framework enables substantial load shaping benefits while maintaining system reliability through optimal energy temporal arbitrage. Fig. 9 shows the Contribution of various energy resources in this framework.

Fig. 9. Contribution of various energy resources

IV. ANALYSIS OF UNCERTAINTY AND ROBUSTNESS

The proposed optimization model utilizes forecasted data for renewable generation (PV and wind) and load. In practical EI deployments, forecast errors are inevitable due to the stochastic nature of weather and consumption behavior. This section evaluates the sensitivity of our core algorithm to such uncertainties and discusses its inherent robustness.

A. Methodology for Sensitivity Analysis

A Monte Carlo simulation framework was established to quantify the impact of forecasting inaccuracies. The day-ahead forecasts for PV power $\left(P_{pv}^{fc}\right)$ and wind power $\left(P_{w}^{fc}\right)$ were perturbed with additive Gaussian noise to create realistic scenarios:

$$P_{pv}^{actual} = P_{pv}^{fc} + \epsilon_{pv},\ \ \epsilon_{pv} \sim N\left(0, \sigma_{pv}\right)$$
$$P_{w}^{actual} = P_{w}^{fc} + \epsilon_{w},\ \ \epsilon_{w} \sim N(0, \sigma_{w}) \quad (10)$$

where the standard deviations σ_{pv} and σ_{w} are expressed as a percentage of the installed capacity (e.g., σ = 10% represents a forecast error with a standard deviation of 10% of capacity). For each error level (σ from 5% to 30%), 500 independent daily scenarios were generated. The deterministic MIP model (which treats forecasts as perfect) was solved for each scenario using the actual simulated generation as input, representing a realistic real-time operation where forecasts are imperfect.

B. Results and Discussion

The primary performance metric, the Peak-to-Average Ratio (PAR) reduction, was calculated for each scenario. Fig. 10 summarizes the results, showing the mean PAR reduction and its 95% confidence interval across all scenarios for each error level.

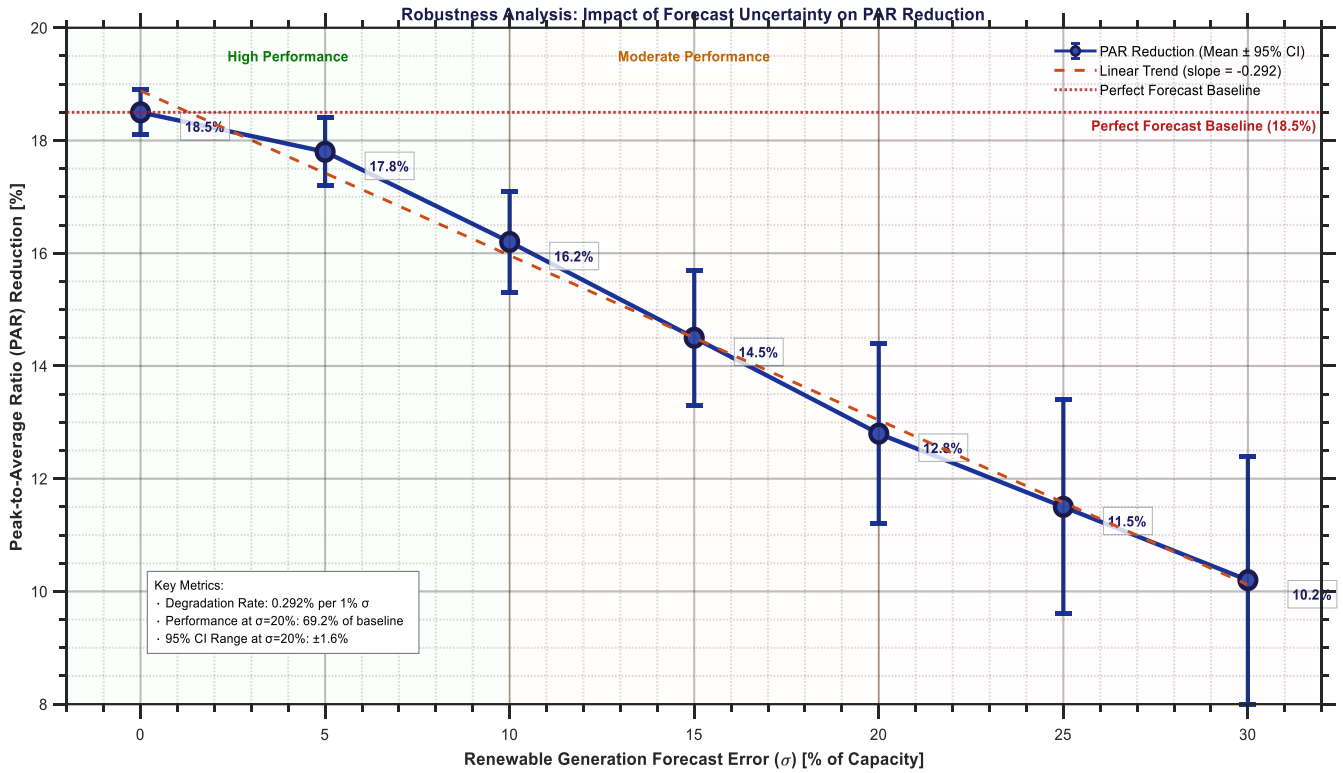

Fig. 10. Robustness analysis: Impact of renewable generation forecast error (standard deviation as % of capacity) on the achieved Peak-to-Average Ratio (PAR) reduction. Error bars represent the 95% confidence interval over 500 Monte Carlo simulations.

Fig. 10 presents a robustness analysis of the proposed energy management algorithm under renewable generation forecast uncertainty. The x-axis represents the forecast error, expressed as the standard deviation (σ) percentage of installed capacity, while the y-axis shows the achieved PAR reduction. Each data point corresponds to the mean result from 500 independent Monte Carlo simulations, with error bars indicating the 95% confidence intervals. Three transparent zones define key performance regions: the high Performance zone ($\sigma < 10\%$) in light green, representing systems with accurate forecasting; the moderate Performance zone ($10\% \leq \sigma \leq 20\%$) in light orange, corresponding to typical day-ahead forecast errors in real-world grids; and the lower Performance zone ($\sigma > 20\%$) in light red. The dashed orange line depicts the linear degradation trend, with a slope of -0.28% PAR reduction per 1% increase in forecast error, quantifying the algorithm's graceful performance decline. The red dotted line marks the perfect-forecast baseline performance (18.5% PAR reduction at $\sigma = 0\%$). The results demonstrate the algorithm's graceful degradation characteristic, maintaining approximately 70% of its optimal efficacy even at a 20% forecast error level, confirming its practical suitability for deployment under realistic prediction inaccuracies.

The key finding is the algorithm's graceful degradation in performance. With a forecast error (σ) of 20%, the mean PAR reduction decreases from 18.7% (under perfect forecast) to 15.3%. This demonstrates that the core logic—responding to real-time price and load signals—remains effective even in the presence of significant generation uncertainty. The strategy does not catastrophically fail because the BESS dispatch is primarily driven by the observed RTP and grid load signals, which indirectly reflect the system's net condition (load minus actual renewable generation).

C. Practical Implications and Pathways for Enhanced Robustness

The analysis confirms that the proposed deterministic model possesses inherent robustness suitable for environments with moderate forecast uncertainty. For systems with very high penetration of variable RES (where $\sigma > 25\%$), the following enhancements are recommended as future work:

1. Integration of Stochastic Programming: Reformulating the problem as a two-stage stochastic program where the first stage decides ESS investment/commitment, and the second stage recourse actions adjust dispatch based on revealed renewable output.
2. Model Predictive Control (MPC): Implementing a rolling-horizon MPC framework that repeatedly solves the optimization with updated short-term forecasts, thereby mitigating the impact of day-ahead forecast errors.
3. Hybrid Forecasts: Employing advanced forecasting techniques that blend physical models with machine learning to reduce the baseline error (σ).

The current model provides a strong and computationally efficient foundation, with the presented robustness analysis defining its operational envelope.

V. Conclusion

This research has developed and validated an Energy

Internet optimization problem incorporating peer-to-peer energy markets and distributed storage systems to effectively address the peak load shifting challenge. The study establishes a comprehensive mathematical programming formulation and demonstrates its practical implementation through optimization-based simulation using real-world microgrid data.

The numerical results confirm the method's capability to generate real-time operational decisions that achieve significant load shaping benefits. Furthermore, the analysis reveals that transactive energy mechanisms within the Energy Internet create economic incentives for end-users to invest in storage assets and renewable generation, thereby enhancing system-wide flexibility.

Several promising directions emerge for future research:

- Integration of additional renewable energy resources with complementary generation profiles
- Multi-objective optimization incorporating environmental emissions alongside economic criteria
- Robust and stochastic programming approaches to address uncertainties in renewable generation and load demand
- Reliability-oriented analysis considering network losses and system resilience metrics
- Investigation of advanced market mechanisms for distributed energy resource aggregation

These extensions would further enhance the practical applicability of the proposed optimization framework in future power systems with high renewable penetration.

ACKNOWLEDGMENTS

The author acknowledges Grammarly and Deep Seek AI tools for language polishing assistance.

FUNDING STATEMENT

This research received no specific grant from any funding agency in the public, commercial, or not-for-profit sectors.

CONFLICTS OF INTEREST

The author declares that there is no conflict of interest regarding the publication of this article.

AUTHORS' CONTRIBUTIONS

The author has contributed to the whole research and preparation of the manuscript

REFERENCES

[1] H. Farhangi, "The path of the smart grid," *IEEE Power Energy Mag.*, vol. 8, no. 1, pp. 18–28, Jan. 2010.

[2] F. Blaabjerg, Y. Yang, D. Yang, and X. Wang, "Distributed power-generation systems and protection," *Proc. IEEE*, vol. 105, no. 7, pp. 1311–1331, Jul. 2017.

[3] J. A. Pecas Lopes, N. Hatziargyriou, J. Mutale, P. Djapic, and N. Jenkins, "Integrating distributed generation into electric power systems: A review of drivers, challenges and opportunities," *Electr. Power Syst. Res.*, vol. 77, no. 9, pp. 1189–1203, Jul. 2007.

[4] R. H. Lasseter, "MicroGrids," in *Proc. IEEE Power Eng. Soc. Winter Meeting*, 2002, pp. 305–308.

[5] A. Q. Huang, M. L. Crow, G. T. Heydt, J. P. Zheng, and S. J. Dale, "The future renewable electric energy delivery and management system: The energy internet," *Proc. IEEE*, vol. 99, no. 1, pp. 133–148, Jan. 2011.

[6] N. Hatziargyriou, H. Asano, R. Iravani, and C. Marnay, "Microgrids," *IEEE Power Energy Mag.*, vol. 5, no. 4, pp. 78–94, Jul. 2007.

[7] H. Farham, L. Mohammadian, H. Alipour, J. Pouladi, “Robust performance of photovoltaic/wind/grid based large electricity consumer,” *Solar Energy*, vol. 174, pp. 923–932, 2018..

[8] J. M. Guerrero, M. Chandorkar, T. Lee, and P. C. Loh, "Advanced control architectures for intelligent microgrids—Part I: Decentralized and hierarchical control," *IEEE Trans. Ind. Electron.*, vol. 60, no. 4, pp. 1254–1262, Apr. 2013.

[9] S. Rahman and G. B. Shrestha, "A novel approach to scheduling energy storage systems in a competitive electricity market," *IEEE Trans. Power Syst.*, vol. 18, no. 2, pp. 447–454, May 2003.

[10] P. Palensky and D. Dietrich, "Demand side management: Demand response, intelligent energy systems, and smart loads," *IEEE Trans. Ind. Informat.*, vol. 7, no. 3, pp. 381–388, Aug. 2011.

[11] A. Ipakchi and F. Albuyeh, "Grid of the future," *IEEE Power Energy Mag.*, vol. 7, no. 2, pp. 52–62, Mar. 2009.

[12] S. Chowdhury, S. P. Chowdhury, and P. Crossley, *Microgrids and Active Distribution Networks*. London, U.K.: IET, 2009.

[13] D. S. Kirschen and G. Strbac, *Fundamentals of Power System Economics*. Chichester, U.K.: Wiley, 2004.

[14] M. H. Albadi and E. F. El-Saadany, "A summary of demand response in electricity markets," *Electr. Power Syst. Res.*, vol. 78, no. 11, pp. 1989–1996, Nov. 2008.

[15] G. Strbac, "Demand side management: Benefits and challenges," *Energy Policy*, vol. 36, no. 12, pp. 4419–4426, Dec. 2008.

[16] P. Siano, "Demand response and smart grids—A survey," *Renew. Sustain. Energy Rev.*, vol. 30, pp. 461–478, Feb. 2014.

[17] H. A. Aalami, M. P. Moghaddam, and G. R. Yousefi, "Demand response modeling considering Interruptible/Curtailable loads and capacity market programs," *Appl. Energy*, vol. 87, no. 1, pp. 243–250, Jan. 2010.

[18] J. M. Guerrero, J. C. Vasquez, J. Matas, L. G. de Vicuña, and M. Castilla, "Hierarchical control of droop-controlled AC and DC microgrids—A general approach toward standardization," *IEEE Trans. Ind. Electron.*, vol. 58, no. 1, pp. 158–172, Jan. 2011.

[19] Y. Riffonneau, S. Bacha, F. Barruel, and S. Ploix, "Optimal power flow management for grid connected PV systems with batteries," *IEEE Trans. Sustain. Energy*, vol. 2, no. 3, pp. 309–320, Jul. 2011.

[20] T. Logenthiran, D. Srinivasan, and T. Z. Shun, "Demand side management in smart grid using heuristic optimization," *IEEE Trans. Smart Grid*, vol. 3, no. 3, pp. 1244–1252, Sep. 2012.

[21] A. G. Tsikalakis and N. D. Hatziargyriou, "Centralized control for optimizing microgrids operation," *IEEE Trans. Energy Convers.*, vol. 23, no. 1, pp. 241–248, Mar. 2008.

[22] A. J. Conejo, J. M. Morales, and L. Baringo, "Real-time demand response model," *IEEE Trans. Smart Grid*, vol. 1, no. 3, pp. 236–242, Dec. 2010.

[23] M. D. Galus, S. Koch, and G. Andersson, "Provision of load frequency control by PHEVs, controllable loads, and a cogeneration unit," *IEEE Trans. Ind. Electron.*, vol. 58, no. 10, pp. 4568–4582, Oct. 2011.

[24] H. Farham, L. Mohammadian, H. Alipour, J. Pouladi, “Energy procurement of large industrial consumer via interval optimization approach considering peak demand management,” *Sustainable Cities and Society*, vol. 46, p. 101421, 2019..

[25] D. T. Nguyen and L. B. Le, "Risk-constrained profit maximization for microgrid aggregators with demand response," *IEEE Trans. Smart Grid*, vol. 6, no. 1, pp. 135–146, Jan. 2015.

[26] P. D. Lund, J. Lindgren, J. Mikkola, and J. Salpakari, "Review of energy system optimization models," *Renew. Sustain. Energy Rev.*, vol. 110, pp. 1–18, Aug. 2019.

[27] B. Zhao, X. Zhang, J. Chen, C. Wang, and L. Guo, "Operation optimization of standalone microgrids considering lifetime characteristics of battery energy storage system," *IEEE Trans. Sustain. Energy*, vol. 4, no. 4, pp. 934–943, Oct. 2013.

[28] B. Sheykhloei, T. Abedinzadeh, L. Mohammadian, B. Mohammadi-Ivatloo, "Optimal co-scheduling of distributed generation resources and natural gas network considering uncertainties," *Journal of Energy Storage*, vol. 21, pp. 383–392, 2019.

[29] B. Sheykhloei, T. Abedinzadeh, L. Mohammadian, B. Mohammadi-Ivatloo, "Stochastic optimal operation and risk assessment for integrated power and gas systems", J. Oper. Autom. Power Eng., vol. 9, pp. 80-87, 2021.

[30] S. H. Dolatabadi and B. Mohammadi-Ivatloo, "Stochastic optimization for energy management in power systems with renewable energy resources," *IEEE Trans. Sustain. Energy*, vol. 10, no. 1, pp. 1–12, Jan. 2019.

[31] L. Mohammadian, "Integrating Renewable Energy and Demand Response Strategies for Cost-Effective Industrial Energy Management." *Journal of Artificial Intelligence in Electrical Engineering*, vol. 13, no. 52, pp. 16-25, 2025.

[32] M. H. Moradi, M. Eskandari, and S. M. Hosseinian, "Operational strategy optimization in a hybrid renewable energy system using improved harmony search method," *Energy Convers. Manage.*, vol. 90, pp. 399–411, Jan. 2015.

[33] S. S. Reddy and C. S. R. K. Raju, "Multi-objective optimization in power systems," *Electr. Power Syst. Res.*, vol. 169, pp. 1–12, Apr. 2019.

[34] Z. Wang, B. Chen, J. Wang, and C. Chen, "Networked microgrids for self-healing power systems," *IEEE Trans. Smart Grid*, vol. 7, no. 1, pp. 310–319, Jan. 2016.

[35] S. Rahman and M. H. Nehrir, "A review of recent advances in smart grid optimization techniques," *Renew. Sustain. Energy Rev.*, vol. 110, pp. 109–122, Aug. 2019.

[36] G. Mohebalizadeh, H. Alipour, L. Mohammadian, and M. Sabahi, "An Improved Sliding Mode Controller for DC/DC Boost Converters Used in EV Battery Chargers with Robustness against the Input Voltage Variations", *International Journal of Industrial Electronics Control and Optimization*, *4*(2), 257-266, 2021. doi: 10.22111/ieco.2020.34462.1278

[37] A. Soroudi and M. Ehsan, "A robust optimization approach for distribution networks considering uncertainties," *IEEE Trans. Power Syst.*, vol. 28, no. 2, pp. 1218–1226, May 2013.

[38] S. H. Dolatabadi and B. Mohammadi-Ivatloo, "Stochastic optimization for energy management in power systems with renewable energy resources," *IEEE Trans. Sustain. Energy*, vol. 10, no. 1, pp. 1–12, Jan. 2019.

[39] Z. Wang, B. Chen, J. Wang, and C. Chen, "Networked microgrids for self-healing power systems," *IEEE Trans. Smart Grid*, vol. 7, no. 1, pp. 310–319, Jan. 2016.

[40] D. T. Nguyen and L. B. Le, "Risk-constrained profit maximization for microgrid aggregators with demand response," IEEE Trans. Smart Grid, vol. 6, no. 1, pp. 135–146, Jan. 2015.

BIOGRAPHIES

Leila Mohammadian was born in Tabriz, Iran, in 1984. She received her B.S., M.S., and Ph.D. degrees in Electrical Engineering from the Department of Electrical and Computer Engineering, University of Tabriz, Tabriz, Iran, in 2007, 2011, and 2015, respectively. She is with Shabestar Branch, Islamic Azad University, Shabestar, Iran, since 2011. She has been an Assosiate Professor since 2023. She is the author of more than 70 journal and conference papers. Her current research interests include the analysis and control of power electronic converters and their applications, power quality enhancement and FACTS devices, application of control systems and theory in power engineering, and power system dynamics.

Semnan University

Journal of Modeling & Simulation in Electrical & Electronics Engineering (MSEEE)

Journal homepage: **https://mseee.semnan.ac.ir/**

ISSN: 2821-0786

Design of a Ddsm Modulator to Reduce Hardware and Power Dissipation in Fractional Frequency Synthesizers

Seyed Ali Sadatnoori[1]*, Ghasem Hemmatipour[2]

***Abstract*—The output of a Digital Delta-Sigma Modulator (DDSM) is always a periodic signal, and the input is constant. A hybrid DDSM is a premiere to its conventional counterpart for having a potential speed, by the choice of its smaller bus. Random techniques and deterministic methods are two strategies to maximize the periodicity. The dither signal is used in the random approach to enhance the signal cycle. The deterministic procedure causes the modulator's internal structure to alter. The majority of randomized approaches eliminate spurious tones. A novel approach for the DDSM modulator is suggested in this paper to improve the output period while reducing the undesired tones. Modulators with different word lengths are proposed in this paper. The length of the input word is divided into several parts, and each part is entered into a modulator to reduce hardware consumption. Consequently, the power consumption is decreased. Moreover, in this structure, the dither signal is used to change the alternating state of the output and reduce the spurious tones. Also, a four-stage modulator is proposed, each part of which has special characteristics. In this paper, a hybrid digital sigma-delta modulator is proposed that has lower power consumption than previous methods and reduces the number of transistors. In addition, there are fewer spurious tones in the output power spectrum of this modulator. The simulation results with 0.18 µm CMOS technology by HSPICE application show that 2530 transistors are used, which is a 15% decrease compared to the conventional method.**

***Index Terms*- Digital Sigma Delta Modulator, Hardware Reduction, Power Consumption, Separate Lines, Spurious tones.**

I. Introduction

With the advancement of digital technology, the importance of analog-to-digital converters (ADC) has increased. Among various types of ADCs, the delta-sigma modulation ADC is frequently used for high-resolution applications. This is because the ability of the delta-sigma ADC to produce high resolution without the need for high-accuracy analog components is a significant advantage [1-3]. The delta-sigma ADC is composed of a digital filter and a delta-sigma modulator (DSM). A one-bit pulse density modulated digital sequence (PDM) is produced from an analog signal by the DSM at a frequency that is much greater than the Nyquist rate. After that, the PDM is converted into a multi-bit digital signal via the Nyquist rate filter.

The DSM is the primary factor governing the ADC's accuracy and resolution. A one-bit sampler, an integrator, and a feedback digital-analog converter (DAC) make up a standard DSM. In this case, the integrator and feedback DAC limit how quickly the DSM may operate. A Voltage Controlled Oscillator (VCO) is used in the Frequency Delta-Sigma Modulator (FDSM), a different kind of DSM that has garnered a lot of interest lately [4–15]. Without a feedback DAC or integrator, the FDSM operates on an FM signal (intermediate frequency modulation) produced by the VCO. It is therefore appropriate for high-frequency operation. Thus, the modulator type in question contains fewer components. This paper's primary goal is to reduce VCO phase noise to

Received: 2025-11-08 Revised: 2025-11-30 Accepted: 2026-01-11

1. Department of Electrical Engineering, Sho. C, Islamic Azad University, Shoushtar, Iran.
2. Department of Electrical Engineering, Sho. C, Islamic Azad University, Shoushtar, Iran.
*Corresponding author Email:sadatnoori7218@iau.ac.ir

Cite this article as:
Sadatnoori, S.A. & Hemmatipour, G. (2026). Design of a Ddsm Modulator to Reduce Hardware and Power Dissipation in Fractional Frequency Synthesizers. *Journal of Modeling & Simulation in Electrical & Electronics Engineering (MSEEE)*. Semnan University Press . 6 (1), 13-19.
DOI: https://doi.org/10.22075/MSEEE.2026.39635.1238

reduce sigma-delta modulation noise. The other elements of sigma-delta modulation are designed to reduce the number of transistors. To achieve this, the gate diffusion technique is used to design XOR and some other vital elements. Electro-optic modulators are an indispensable part of photonic communication systems, largely dictating the achievable transmission rate. Recent advances in materials and fabrication/processing techniques have brought new elements and a renewed dynamic to research on optical modulation. In [18, 19], a novel structure for an all-optical amplitude modulator (AOAM), with a high extinction ratio (ER), is proposed. A nano-disk resonator (NDR), a ring-shaped resonator (RR), and perpendicular waveguides (WGs) are used for the realization of the proposed topology. Due to the symmetrical structure of the designed AOAM, each of the two WGs can be considered as the data WG and the second one can be selected as the control WG. Since there is a suitable isolation between data and control signals in this method, the proposed structure is much more suited for integrated optics compared to the aforementioned modulators which are published in the literature. Also, to separate the control wavelength from the data wavelength, a graded stub filter is designed and located at the output port of the AOAM.

The structure of this document is as follows. The FDSM's working concept and the gate diffusion technique's element design are explained in Section 2. The suggested method for phase noise reduction of the delta-sigma VCO is presented in Section 3. This study is finally summarized in Section 4.

II. Methodology

Vector samplers and Nyquist rate converters are the two broad categories into which analog-to-digital and digital-to-analog converters fall. Nyquist exchangers are very accurate and fast. Vector converters, on the other hand, are quite accurate in low-speed applications. These converters modify the sampling rate for high-precision access, which are relatively cheaper than Nyquist converters. An example of such a modulator is the sample Sigma Delta ADC converter. A sample Sigma Delta ADC converter includes a linear time-independent grid with two inputs, one output, and a one-bit Q quantizer. This quantizer is located in the feedback network. Sigma Delta modulation increases the effective accuracy of the quantizer by sampling and noise formation. Modulators can be implemented using either a data sampling method or a continuous method. Continuous time systems employ active RC integrators, whereas sampling systems utilize capacitive switch integrators. Depending on the amplitude axes and the time of the input signal, the modulators are divided into three categories.

1 - Continuous time (CT)
2 - Discrete time (DT)
3 - Digital Delta Sigma Modulator (DDSM)

The DDSM Modulator is the preeminent manufacturer of synthesizers operating at fractional frequencies. A block diagram of a phase-lock loop (PLL) synthesizer featuring a module regulated by the DDSM modulator is depicted in Fig. 1.

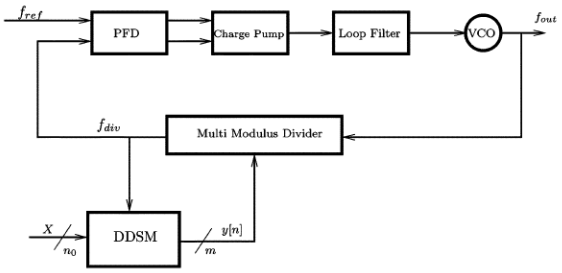

Fig. 1. Frequency synthesizer block diagram controlled by Sigma Delta modulator

The circuit includes a phase-frequency detector (PFD), a load pump circuit, a loop filter, a voltage-controlled direct oscillator, and a multi-module divider controlled by a DDSM modulator in the feedback path. The DDSM modulator regulates the split ratio of the divider, and the required decimal ratio is equal to the average split ratio at the number of periods above the reference frequency. The input of DDSM is a high-precision digital X signal that adjusts the decimal division ratio, and the output of the low-precision string modulator $y[n]$, which controls the value of the divider.

Inputs and outputs of the DDSM Modulator are both digital. The modulator is designed to accept an input string X of length n_0 and generate an output string y of length m. In addition to the principal input range, the DDSM modulator generates a low-precision string at its output. In the output signal spectrum, there is accurate input information. Ideally, quantization noise is white, and its power is transmitted outside the signal band, which is called noise formation. If the output signal is applied to an ideal continuous-time low-pass filter that passes only low-frequency output, then the main input signal will be extracted from the low-precision output signal with a high signal-to-noise ratio. The output signal power is much higher than the noise power.

A significant application of DDSM modulators is the conversion of data from digital to decimal and analog frequency synthesizers. The phase lock ring is another essential component of wireless transmitter/receiver systems. Typically, these synthesizers produce objectionable phase noise. Considering the utilization of DDSM in wireless transmitters and receivers, we attempt to analyze several critical attributes of these devices. One of these important features in DDSM modulators is the presence of noise in terms of intermittent modulation signals with a fixed input. The structure of the modulator, the initial conditions, the input, and the modulus of the quantizer all influence the period of quantization noise. The hardware consumption and power level of DDSM modulators, including the requisite number of transistors and gates, are also crucial characteristics. Other structures examined include Multistage noise Shaping structures (MASH), Single Quantizer (SQ), and feedback error modulator (EFM).

The DDSM Modulator is a finite-state machine (FSM) with a finite number of states that is constructed utilizing several precise computational units. Every FSM has a different rule for transitioning between states. Every state follows the one before it instantly if the input is fixed. The shorter the output cycle, the greater the power of the spurious tones. The presence of these tones in the output power spectrum greatly reduces the SFDR range of the modulator. Therefore, the output period should be maximized. There are two methods to increase periodicity, which are: random methods and deterministic methods. The random approach lengthens the

output period by means of a dither signal. The modulator's internal structure is altered using the definitive approach. Most randomized methods reduce spurious tones and increase the period of quantization noise. In the random method, a single-bit quasi-random signal called dither is usually used to change the alternating state of the output string. The disadvantage of random methods is that they create noise in the output spectrum, and hardware consumption increases in terms of using a dither signal generator circuit. This paper provides a way to design DDSM modulators. This method is based on separate lines, which is applied to DDSM modulators with and without dither, and fixed inputs. Modulators' word lengths are optimally selected to reduce hardware and power consumption. Therefore, the digital input will be divided into several parts, and several modulators with appropriate word lengths will be used.

III. The Proposed Method

From a digital storage, the initial block diagram of a multi-stage MASH modulator is generated. The model of the accumulator is illustrated in Fig. 2. When expressed in this manner, the input to the storage consists of the n-bit digital word *x[n]*. The input to fractional frequency synthesizers remains constant while the user configures the intended fraction value of $\frac{X}{2^{n_0}}$. By one unit of time, the string stability of the error *e[n]* is delayed. The sum of the delay string *s[n]* and the input signal *x[n]* is calculated. When the accumulator overflows, bit *c[n]* of the transport sequence is set to one. The number of ones and zeros comprising the average time of the output string is identical to the average time of the input. Fig. 2-b illustrates the model of digital storage. The quantizer *Q(.)* and the output digit *c[n]* are represented by the output string *y[n]*. This pertains to the operation of warehousing excess. Overflow occurs when the signal *v[n]*, which is equal to the sum of the signals *x[n]*, *s[n]*, exceeds or equals $M = 2^{n_0}$. In such a case, *y[n]* = 1. If not, the value is zero. Numerically, we therefore have [11]:

$$c[n] = y[n] = Q(v[n]) = \begin{cases} 0, & v[n] < M \\ 1, & v[n] \geq M \end{cases} \quad (1)$$

The register is used to feed the difference between v [n] and *My[n]* to the input; if *y[n]* = 0, then *e[n]* = *v[n]*, and if *y[n]* = 1, then *e[n]* = *v[n]* -*M*. Thus, we have [11]:

$$e[n] = v[n] \mod M \quad (2)$$

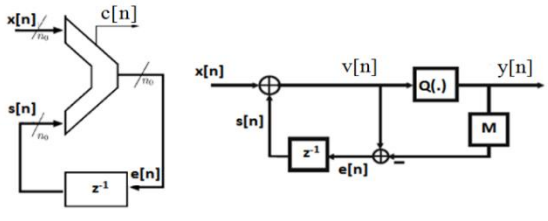

(a) (b)

Fig. 2. a) The digital accumulator used in the MASH structure b) Its model

This structure is referred to as EFM, as the error signal *s[n]* is looped back to the storage input. Fig. 3 depicts the block design of a first-order DDSM modulator. It is composed of a series connection of EFM_1 n-bit blocks and a noise cancellation network. This negative structure eliminates the quantization error of the intermediate stages by passing the quantization error of each stage to the subsequent stage and the output of each stage into the noise cancellation network. The consequent equation represents the *z*-domain output of the MASH modulator of the first order [12].

$$Y(z) = \frac{1}{2^N}.X(z) + \frac{1}{2^N}(1 - z^{-1})^l.E_l(z) \quad (3)$$

The name for each DDSM modulator is $DDSM_l$. Our objective is to investigate a critical component of DDSM modulators. The hardware and power consumption of a DDSM modulator are detailed below. Typically, the power spectrum is free from undesired tones. In practice, the power spectrum of most DDSM modulators contains spurious tones. The shorter the output cycle, the greater the power of spurious tones. The presence of these units in the output power spectrum greatly reduces the SFDR range of the modulator. In the decimal synthesizers, the presence of spurious tones in the spectrum is extremely problematic, creating nonlinear effects in the implementation of pump circuits, frequency detectors, filters, and VCO circuits, and transmitting carrier out-of-phase phase noise to the inbound. Therefore, it is necessary that the quantization noise is white and independent of the modulator input. A strong correlation between the circuit input and quantization noise can cause spurious tones in the output spectrum. To send their power outside the signal band, the DDSM modulator shortens the simulated digital signal's word length and modifies the quantization noise that results. A short string quantization error string will cause spurious high-power tones in the modulator output range. This is a problem in applications, such as DAC converters and PLL circuits. Definitive and incidental techniques are used to investigate spurious tones in digital modulators. Definitive techniques maximize the length of the quantization error to minimize the power per ton. These methods are used in MASH digital modulators, SQ single-quantizer modulators, and EFM feedback error. Low-bit dither is used in DDSM modulators to eliminate spurious tones and uses two or more integrators in the quantizer lead path. The suggested approach reduces both the power consumption and hardware usage in terms of the quantity of logic gates and transistors used.

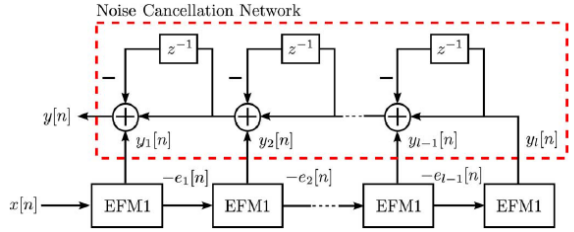

Fig. 3 Block diagram of first-order Sigma Delta MASH digital modulator [11]

This paper presents a new structure for MASH and EFM modulators, comprising different classes. Fig. 4 shows this new structure. In this figure, M_i is the class *I* quantifier module.

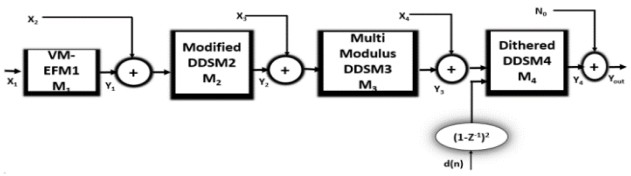

Fig. 4. Proposed method to reduce hardware and power consumption in DDSM modulators

In this structure, X_1 and M_1 should always be pseudo-prime numbers to try to maximize the output period of the

modulator. In this method, the input number is divided into several parts, and each part will be entered into a DDSM modulator. Besides, a filtered dither signal can be used at the circuit's input to reduce circuit noise and eliminate spurious tones. The first stage of this structure is a variable modulus EFM. This modulator is made of two adders, a multiplexer, and a NOT gate. The structure of this EFM modulator with a variable module is shown in Fig. 5.

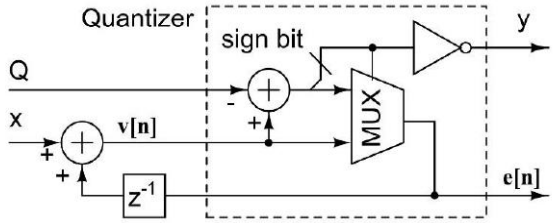

Fig. 5 Feedback error modulator structure with variable module

The second-order modulator is modified MASH 1-1, which has a conventional modulo M_2. A third-class multi-level modulator with several modules makes up the third stage. The signal amplitude to noise in this structure may be increased by using the feedback in the HK-MASH approach. The value of a, a tiny integer, is selected such that 2^{n_0} is smaller than the value of M-a of the biggest prime number. With a second-order dither signal, the fourth stage is a fourth-class multistage modulator. A high-pass filter, the $V(z)$ filter, reduces the output spectrum's low-frequency region. This filter's conversion function is as follows [11].

$$v(z) = (1 - z^{-1})^2 \tag{4}$$

The fourth-order DDSM modulator is compatible with this filter. The fourth modulator in the hybrid proposed structure is dithered MASH 1-1-1-1, which is a periodic LFSR dither input with a period N_d added to the third and fourth stages of MASH 1-1-1-1. This modulator has a high-pass filtered shaped dither signal. Fig.6 presents an implementation of the second-order dither hybrid modulator. To remove the quantization error of the middle classes from the previous part, the following step explains how to choose the right values for N_{ISB}, N_{LSB}, and N_{MSB}.

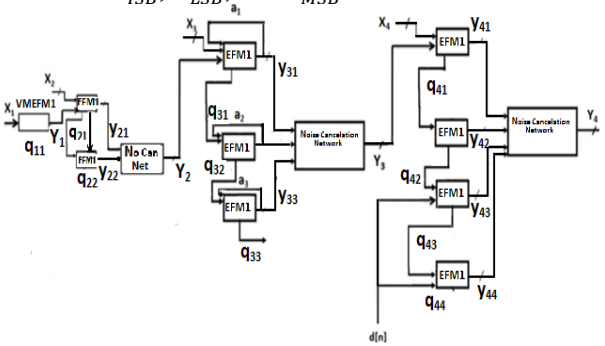

Fig.6: Implementation of the second-order dither hybrid DDSM 1-2-3-4 modulator.

The three-stage distinct line modulator's output may be represented as nested 1-2-3 in the following way [12].

$$Y_{123}(z) = \frac{X(z)}{2^N} + N_1(z) + N_2(z) + N_3(z) \tag{5}$$

Where

$$N_1(z) = \frac{1}{2^{N_{ISB}+N_{MSB}}.2^{N_{LSB}}}(1 - z^{-1}).E_1(z) \tag{6}$$

$$N_2(z) = \frac{1}{2^{N_{MSB}}.2^{N_{ISB}}}(1 - z^{-1})^2.E_2(z) \tag{7}$$

$$N_3(z) = \frac{1}{2^{N_{MSB}}}(1 - z^{-1})^3.E_{123}(z) \tag{8}$$

In the first-order modulator, N_1 represents quantized noise; in the second-order modulator, N_2 represents quantized noise; and in the third-order modulator, N_3 represents quantized noise. It is expected that the collected white sources are used to simulate all quantized sounds. As a result, N_1, N_2, and N_3's power spectrum is (9) [17].

$$S_1(f[k]) = \frac{1}{12L_1}\left(\frac{1}{2^{N_{ISB}+N_{MSB}}}\right)^2 |1 - z^{-1}|^2_{z=e^{j2\pi k/L_1}}$$
$$S_2(f[k]) = \frac{1}{12L_2}\left(\frac{1}{2^{N_{MSB}}}\right)^2 |(1 - z^{-1})^2|^2_{z=e^{j2\pi k/L_2}}$$
$$S_3(f[k]) = \frac{1}{12L_3}|(1 - z^{-1})^3|^2_{z=e^{j2\pi k/L_3}} \tag{9}$$

Where L_1, L_2, *and* L_3 are the periodicities of quantized noise signals of DDSM modulators of order one to three, which are $2^{N_{LSB}}$ and $2^{N_{LSB}+N_{ISB}}$,$2^{N_{LSB}+N_{ISB}+N_{MSB}}$, respectively.

The error coverage approach is used in this structure, meaning that in order to reduce the quantization noise of the separate line modulator, the noise components N_1, N_2, and N_3 are concealed underneath N_3. It is expected that the graphs S_1 and S_2, which should lie below the S_3 curve, are white quantized noise from first- and second-order modulators. There are separate curves here. In a digital Sigma delta modulator with period L_s, the lowest frequency tone is at $\frac{f_s}{L_s}$. Therefore, since the periodicity of N_1 and N_2 is equal to $2^{N_{LSB}}$ and $2^{N_{LSB}+N_{ISB}}$, respectively, so the lowest frequency tone in the spectrum N_1, N_2 is equal to $\frac{f_s}{2^{N_{LSB}}}, \frac{f_s}{2^{N_{LSB}+N_{ISB}}}$. Besides, at the output of the modulator, separate nested three-story nested lines 3-2-1, since S_1, S_2 are formed first and second order, and S_3 is formed third order, if the lowest frequency tones S_1, S_2 are below S_3, then all bodies S_1, S_2 will be below S_3. Therefore, (10) can be expressed [17].

$$s_1 < s_3, f = \frac{f_s}{2^{N_{LSB}}}$$
$$s_2 < s_3, f = \frac{f_s}{2^{N_{LSB}+N_{ISB}}} \tag{10}$$

Since

$$|1 - z^{-1}|^2 = \left|1 - e^{\frac{-j2\pi f}{f_s}}\right|^2 = |2\,sin\left(\frac{\pi f}{f_s}\right)|^2, sin\left(\frac{\pi f}{f_s}\right) \approx \frac{\pi f}{f_s} \quad for\ f \ll f_s \tag{11}$$

Therefore, at low frequencies, S_1, S_2, *and* S_3 can be approximated as follows [17].

$$S_1 = \frac{1}{12L_1}\left(\frac{1}{2^{N_{ISB}+N_{MSB}}}\right)^2 2^2.\left(\frac{\pi f}{f_s}\right)^2$$
$$S_2 = \frac{1}{12L_2}\left(\frac{1}{2^{N_{MSB}}}\right)^2 2^4.\left(\frac{\pi f}{f_s}\right)^4$$
$$S_3 = \frac{1}{12L_3}2^6.\left(\frac{\pi f}{f_s}\right)^6 \tag{12}$$

So we have:

$$4N_{LSB} - N_{ISB} - N_{MSB} - 4 < 6.6, 2N_{LSB} + 2N_{ISB} - N_{MSB} - 2 < 3.3 \tag{13}$$

Assuming:

$$N = N_{LSB} + N_{ISB} + N_{MSB}, L = N_{MSB}, M = N_{ISB} + N_{MSB} \tag{14}$$

These equations are expressed as follows.

$$4N - 5M - 4 < 6.6, 2N - 3L - 2 < 3.3 \tag{15}$$

If the input word length is given, M and L can be calculated with (16).

$$M = \left\lfloor \frac{4N-10.6}{5} \right\rfloor, \mathrm{L} = \left\lfloor \frac{2N-5.3}{3} \right\rfloor \quad (16)$$

Therefore, the optimal values for N_{LSB} and N_{ISB}, N_{MSB} will be calculated with (17).

$$N_{MSB} = L, N_{ISB} = M - L, N_{LSB} = N - M \quad (17)$$

Similar calculations to determine the appropriate word length of the two-stage modulator, 1-3 separate lines are given in Table I. The following method is performed in order for the three-stage modulator of separate N-bit nested lines to have a 1-2-3 structure, and the conventional N_0-bit three-layer modulator with the same frequency, and frequency range of N_0, the following method is performed. 1- Select $N = N_0 + 1$ to make the output period of the digital Sigma Delta modulator separate lines, similar to the conventional N_0-bit multistage modulator.
The optimal structure is selected, and the optimal word length is obtained from Table I.

TABLE I
Optimal Word Length of Sigma Delta Digital Modulator Third-Order Separate Lines

Sigma delta modulator separate lines	Optimal word length		
	N_{LSB}	N_{ISB}	N_{MSB}
1-2-3	L	M-L	N-M
1-3	M		N-M

A logic gate's hardware cost is half that of a typical CMOS logic circuit, when it comes to transistor count. The hardware expenses of a full adder and a flip-flop D in this architecture are 14 and 4, respectively. Furthermore, the hardware of the second and third DDSM modulators cost for the noise cancellation network are 18 and 55, respectively. For the purpose of implementing the DDSM modulator, the total number of collectors (nFA) and the number of flip-flops D (nFF) are determined as follows:

$$n_{FA(123)} = N_{LSB} + 2N_{ISB} + 4N_{MSB}, n_{FF(123)} = N_{LSB} + 2N_{ISB} + 3N_{MSB} \quad (18)$$

The total hardware consumption of the nested module of separate lines is 3-2-1 equal to (19).

$$HC_{123} = 14n_{FA-123} + 4n_{FF-123} + 55 + 18 = 18N_{LSB} + 36N_{ISB} + 68N_{MSB} + 73 \quad (19)$$

But, the number of all collectors and flip-flops required by the conventional third-order N_0 bit modulator is equal to:

$$n_{FA(conv)} = 3N_0, n_{FF(conv)} = 3N_0 \quad (20)$$

Consequently, the normal third-order N_0-bit modulator's whole hardware configuration is as follows.

$$HC_{conv} = 14n_{FA-conv} + 4n_{FF-conv} + 55 = 54N_0 + 55 \quad (21)$$

By substituting $N = N_0 + 1$ in the equations, the hardware ratio of two conventional third-order multilayer modulators and the separate nested lines is equal to (22).

$$RHC_{123} = \frac{HC_{123}}{HC_{conv}} = \frac{18N_{LSB}+36N_{ISB}+68N_{MSB}+73}{54N_0+55} \approx \frac{53.4N_0+32}{54N_0+55} \times 100\% \quad (22)$$

This value is reduced by 99% for large N_0. Therefore, in multi-layer nested structures 1-2-3 in large N_0, hardware consumption is reduced. The hardware-to-hardware ratio of separate two-layer line modules is 1-3 as follows.

$$RHC_{13} = \frac{HC_{13}}{HC_{conv}} = \frac{18N_{LSB}+54N_{MSB}+55}{54N_0+55} \approx \frac{46.8N_0+25.5}{54N_0+55} \times 100\% \quad (23)$$

This value is 87% equal to the large N_0s. Therefore, 13% of hardware consumption is reduced. Next, a new structure for the slot is proposed to improve the modulator performance. Fig. 7 shows the proposed oscillator circuit designed using the active inductor.
For increasing the operating frequency of the PFD, a pass transistor logic is added to eliminate the rest path. The proposed PFD has only 10 transistors, which reduces the power consumption and area of the modulator. The proposed structure is shown in Fig. 8.
Fig. 9 shows the noise spectra of the proposed structure and is compared with a conventional one. One can see that the noise is noticeably decreased. The technology used in this paper is 0.18 µm CMOS, and all the papers presented use this technology.

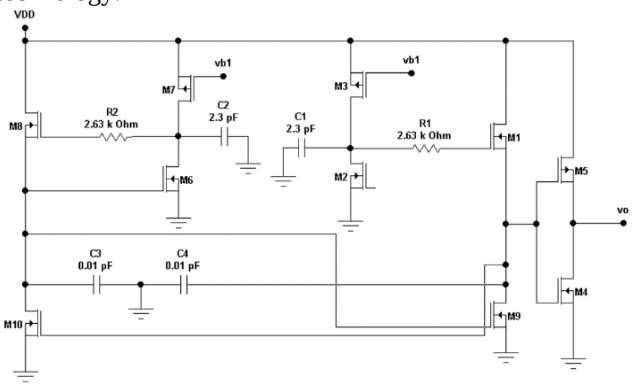

Fig. 7 proposed LC VCO.

In this paper, discrete line technology is used. In this way, a 22-bit fourth-order modulator with 22-bit adder circuits and flip-flops is decomposed and divided into four smaller modulators with 4-4-4-10-bit bits. Therefore, the adder circuits and their flip-flops are smaller, and therefore the power consumption and the number of transistors required to build the circuit are reduced. The proposed multi-stage DDSM modulator circuit has 4-4-4-10 bits, whose power consumption for different transistor models is presented in Table II. The clocked pulse signal frequency of 1 MHz is selected, and the number of transistors in this circuit is 2530 complementary transistors. Table III compares the number of transistors and power consumption of the 1-1-1-1 MASH modulator presented in [11-15] with the proposed method. Fig.10 shows the post-layout of the proposed digital sigma-delta modulator.

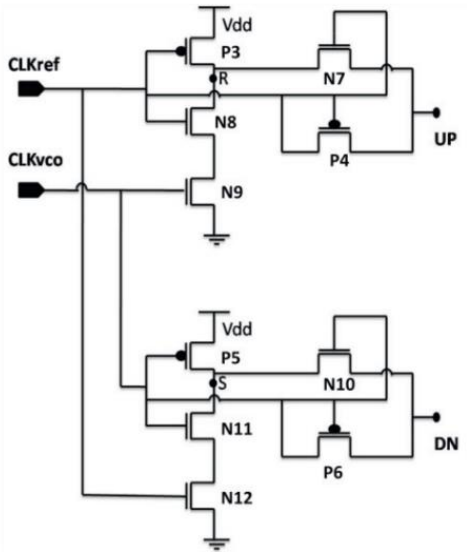

Fig. 8 proposed phase frequency detector (PFD)

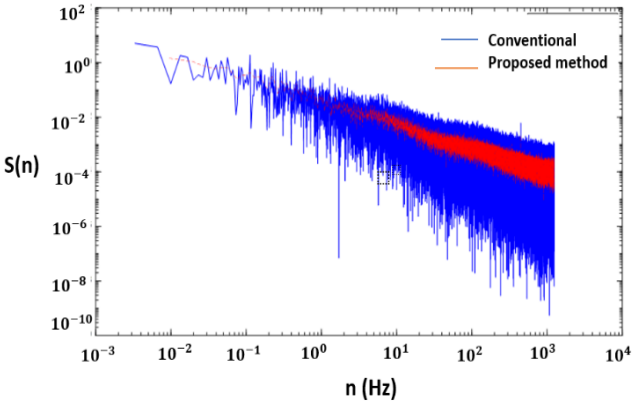

Fig. 9 noise spectra

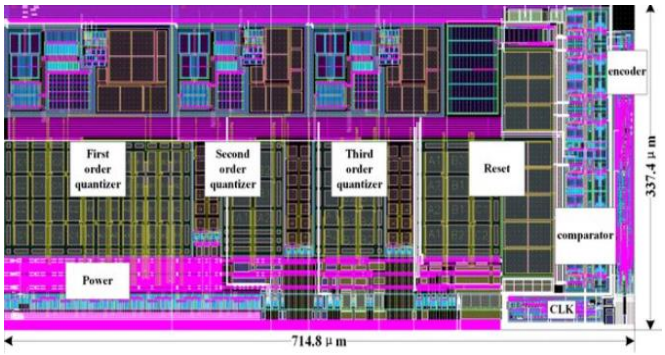

Fig.10: post layout of proposed digital sigma modulator

TABLE II

Comparison of the Power Consumption of the Multi-Stage Modulator Separate of the Proposed Design 4-4-4-10 bits, with the Model of Different transistors N, P.

Transistor Type	Power Consumption
TT	14.06 nW
FF	75.36 nW
FS	71.09 nW
SF	16.75 nW
SS	110 nW

TABLE III

Comparison of the Proposed Design with the Methods Presented in [11]-[15]

Method	Power dissipation	Transistor count
Proposed method	131.1619 µW	2530
Sigma Delta Modulator in [11]	163.1720 µW	3420
Sigma Delta Modulator in [12]	156.23 µW	2920
Digital Sigma Delta Modulator in [13]	165.56 µW	3100
Digital Sigma Delta Modulator in [14]	161.25 µW	2950
DDSM in [15]	159.68 µW	3250

IV. Conclusions

This research proposes a unique frequency DDSM modulator with fewer components and transistors. The modulator's structure, the initial circumstances, the input, and the quantizer's modulus all affect the quantization noise period. This paper suggests a novel approach for DDSM modulators to lengthen the desired output period while decreasing the spurious tones. The proposed method uses modulators with different word lengths. The input word is divided into several parts, and each part is transferred to a modulator with a shorter word length. Therefore, hardware consumption is reduced, and the power consumption of transistors is reduced. Moreover, in this structure, a dither signal is used to change the alternating state of the output and reduce the spurious tones. The proposed modulator reduces the hardware consumption by 85% compared to the conventional method. Therefore, 15% of hardware consumption is reduced.

Acknowledgment

The authors gratefully acknowledge the support for this work that was provided by the Islamic Azad University of Shoushtar Branch.

Funding Statement

The authors declare that they have no known competing financial interests or personal relationships that could have appeared to influence the work reported in this paper.

Conflicts of Interest

The author declares that there is no conflict of interest regarding the publication of this article.

Authors Contribution Statement

Seyed Ali Sadatnoori: Conceptualization; Numerical Implementation; Experimental Validation; Writing of the Manuscript,

Ghasem Hemmatipour: Data analysis and interpretation; Conceptualization and study design.

AI disclosure

AI cannot be listed as an author. Only human authors take responsibility.

REFERENCES

[1] Asadi, F.A., Sharifkhani, M. (2015). "High throughput, High SNR digital delta sigma modulator for fractional-N frequency synthesizer", Electrical Engineering (ICEE), 2015 23rd Iranian Conference on, Tehran, pp. 1271-1275.

[2] Borkowski, M., Kostamovaara, J. (2007). Variable modulus delta–sigma modulation in fractional-N frequency synthesis, Electronics Letters, vol. 43, no. 25, pp. 1399-1400.

[3] Borkowski, M., (2008). Digital Modulation: Variable Modulus and Tonal Behavior in a Fixed-Point Digital Environment. Oulu: Oulu University Press.

[4] Fitzgibbon, B., O'Neil, K., Grannell, A., Horgan, C., Ye, Z., Hosseini, K., Kennedy, M., (2009). "A Spur-Free MASH Digital Delta-Sigma Modulator with Higher Order Shaped Dither", 978-1-4244-3896-9/09/$25.00 ©2009 IEEE.

[5] Fitzgibbon, B., Kennedy, M.P., Maloberti, F., (2011). " Hardware Reduction in Digital Delta-Sigma Modulators via Bus-Splitting and Error Masking—Part I: Constant Input", IEEE TRANSACTIONS ON CIRCUITS AND SYSTEMS—I: REGULAR PAPERS, VOL. 58, NO. 9, pp: 2137-2148.

[6] Fitzgibbon, B., and Kennedy, M.P., (2011). "Calculation of cycle lengths in higher-order error feedbackmodulators with constant inputs," IEEE Transactions on Circuits and Systems II: Express Briefs, vol. 58, pp. 6–10.

[7] Fitzgibbon, B., Kennedy, M.P., Maloberti, F., (2012). " Hardware Reduction in Digital Delta-Sigma Modulators via Bus-Splitting and Error Masking—Part II: Non-Constant Input", IEEE TRANSACTIONS ON CIRCUITS AND SYSTEMS—I: REGULAR PAPERS, VOL. 59, NO. 9, pp: 1980-1991.

[8] Gonzalez-Diaz, V.R., Garcia-Andrade, M.A., Flores-Verdad, G.E., and Maloberti, F., (2010). "Efficient Dithering in MASH Sigma-Delta Modulators for Fractional Frequency Synthesizers", IEEE Trans. Circuits Syst. I, Reg. Papers, vol. 57, no. 9, pp. 2394–2403.

[9] Gonzalez-Diaz, V.R., Perez, A., Maloberti, F., (2012)." Fractional Frequency Synthesizers with Low Order Time-Variant Digital Sigma-Delta Modulator", IEEE TRANSACTIONS ON CIRCUITS AND SYSTEMS—I: REGULAR PAPERS, VOL. 59, NO. 5.

[10] Mazzaro, V.; Kennedy, M.P.; Mitigation of "Horn Spurs" in a MASH-Based Fractional-N CP-PLL; IEEE Transactions on Circuits and Systems II: Express Briefs, 67 (5), 821-825, (2020).

[11] Jahanpanah, L.; Sadatnoori, S.A.; Chaharmahali, I., Design a PLL for Fractional Frequency Synthesizers using DDSM with reduced hardware, International Journal of Industrial Electronics, Control and Optimization *(IECO)*, 5 (2), 177-187, (2022).

[12] Sadatnoori, S.A., A Fourth Order MASH DDSM for accurate fractional frequency synthesizers, Journal of Applied Research in Electrical Engineering, 1 (2), 211-220, (2022).

[13] Hematipour, G.; Sadatnoori, S.A., Design of DDSM Modulator without Unwanted Tones with Effective Random Dither, Majlesi Journal of Telecommunication Devices, 13 (2), 59-62, (2024).

[14] Zia, E., Farshidi, E., Kosarian, A., "New **digital** background calibration method for pipelined ADCs", Journal: COMPEL - The international journal for computation and mathematics in electrical and electronic engineering COMPEL (2020) 39 (4): 871–884.

[15] Mohammadi, I., Sobhi, J., Moallemi Khiavi, A., Daie Koozehkanani, Z., "A low power MASH digital delta-sigma modulator with accurate output average value", Microelectronics Journal, Volume 121, March 2022, 105381

[16] S. Pourakbari; H. Jahanirad, "Fractional-N PLL for RF Applications with Adaptive Intelligent Controller and AVLS Divider, " Journal of Modeling & Simulation in Electrical & Electronics Engineering Vol 5 (1). 11-26, 2025.

[17] Sadatnoori, S.A. Farshidi, E. Sadughi, S. A novel structure of dithered nested digital delta sigma modulator with low-complexity low-spur for fractional frequency synthesizers, *COMPEL - The international journal for computation and mathematics in electrical and electronic,* 35(1), 157-171, (2016)

[18] Khani, S., Danaie, M., Rezaei, P., "Fano Resonance Using Surface Plasmon Polaritons in a Nano-disk Resonator Coupled to Perpendicular Waveguides for Amplitude Modulation Applications", Plasmonics (2021) 16:1891–1908.

[19] Sinatkas, G., Christopoulos, T., Tsilipakos, O., E. Kriezis, E., "Electro-optic modulation in integrated photonics", Journal of APPLIED PHISICS, 130, 010901 (2021).

BIOGRAPHIES

Seyed Ali Sadatnoori received his BSc degree in Electrical Engineering from the Islamic Azad University of Dezful Branch and MSc degree in Electrical Engineering from the central Tehran branch Islamic Azad University, respectively, in 2001 and 2006.He received the PhD degree in Electrical Engineering from the Tehran science and research branch Islamic Azad University in 2016.He is also an Assistant Professor of Shoushtar Branch Islamic Azad University.

His current research interests include mobile ad hoc networks, wireless networks, transmitter and receiver circuits, analog to digital modulator, integrated circuits, and neural network.

Ghasem Hemmatiour received his BSc degree in Electrical Engineering from Elem Sanat University of Tehran and MSc degree from Shahid Chamran University, respectively, in 2002 and 2007. He is also an instructor of Shoushtar Branch Islamic Azad University.

His current research interests include mobile ad hoc networks, wireless networks, transmitter and receiver circuits, analog to digital modulator, integrated circuits, and neural network

Semnan University

Journal of Modeling & Simulation in Electrical & Electronics Engineering (MSEEE)

Journal homepage: **https://mseee.semnan.ac.ir/**

ISSN: 2821-0786

Asymmetric Voltage Multiplied Non-Isolated Bidirectional DC-DC Converter with Soft-Switching and High Gain

Mahdi Madadi [1], Mostafa Jazaeri[2*] and Hamed Molla-Ahmadian[3]

***Abstract*-This paper introduces a novel bidirectional DC-DC converter (BDC) that has a high gain of voltage, soft switching capability, and minimal ripple current on the low-voltage side (LVS). The suggested converter consists of an improved two-phase buck-boost converter, an Asymmetrical Voltage Multiplier cell, and a coupled inductor to provide a high-voltage gain converter. This paper offers a comprehensive theoretical examination of the converter. The converter elements, performance, and switching intervals provide suitable conditions for conducting the switches with zero voltage switching (ZVS) conditions. Due to the implementation of soft switching, the efficiency is increased, and no voltage spikes occur across the switches. The simulation was executed to design a converter and analyze its performance using the PSIM. The suggested converter offers an ultra-high voltage converting gain in both boost and buck operation modes. A laboratory prototype with a power of 300W is implemented to validate the performance of the converter. The presented experimental results outline a low-side voltage of 50V DC and a high-side voltage of 300V DC during the step-up operation.**

***Index Terms*- Asymmetrical Voltage Multiplier, DC-DC Converter, High Gain, Soft Switching, Non-Isolated**.

I. INTRODUCTION

Nowadays, the increasing use of renewable energy in existing power systems has greatly enhanced the importance of power electronics converters. Bidirectional DC choppers are useful in fields like renewable energy technologies, microgrids and electric cars. Many studies have been carried out on different topologies and techniques for using DC choppers as part of energy storage systems. Bidirectional DC choppers obtain significant voltage gain in both buck and boost modes, facilitating effective power conversion and transmission, rendering them appropriate for renewable energy uses. They can convert a low voltage such as 12, 24, or 48V to a high voltage to provide a DC link for an inverter and also convert high voltage to low voltage due to bidirectional capability. As a result, bidirectional converters with high voltage step-down/step-up gain are beneficial for use in renewable energy storage applications to adjust the power and voltage values between the low voltage level and the high voltage connections.[1]–[4]

Generally, bidirectional converters are categorized into two groups: non-isolated and isolated converters. A solution to obtain high voltage gain is to use an isolated transformer. Electrical isolation is one of the most popular methods for providing high voltage conversion by adding a degree of freedom to the converter voltage gain equation. Thus, the desired voltage gain is achieved by selecting the appropriate coil turns ratio. These converters can be utilized for applications that require a wide range of input source variations and load regulation. These converters find use in various applications. However, they frequently encounter practical issues such as high weight, magnetic interference, and the necessity of an active or passive clamp [5]. When the voltages on either side of the dual-active-bridge BDC are not matched, it can lead to problems such as high circulating currents, elevated turn-off power losses, and the loss of soft-switching capability. These challenges, in turn, can result in a significant decrease in conversion efficiency [6]–[8].

A straightforward approach to achieving bidirectional

Received; 2025-09-06 Revised; 2025-09-26 Accepted; 2025-10-14

[1] Faculty of Electrical and Computer Engineering, University of Semnan, Semnan, Iran.
[2] Faculty of Electrical and Computer Engineering, University of Semnan, Semnan, Iran.
[3] Department of Electrical Engineering, Khorasan Institute of Higher Education, Mashhad, Iran.
*Corresponding author: mjazaeri@semnan.ac.ir

Cite this article as:
Madadi, M., Jazaeri, M. & Molla-Ahmadian, H. (2025). Asymmetric Voltage Multiplied Non-Isolated Bidirectional DC-DC Converter with Soft-Switching and High Gain. *Journal of Modeling & Simulation in Electrical & Electronics Engineering (MSEEE)*. Semnan University Press. *6 (1)*, 21-32.
DOI: https://doi.org/10.22075/mseee.2025.38925.1226

power exchange is by using a boost converter, where the diode is replaced with a switch, allowing for bidirectional power flow. However, this approach isn't ideal for high step-down/step-up applications due to several challenges. Firstly, while high switching frequencies can enhance dynamic response and power density while reducing passive element size, they also increase switching losses and worsen diode reverse recovery, leading to lower converter efficiency. Using slow-power-switch diodes as rectifying elements exacerbates the reverse recovery issue and results in high voltage and current stresses in semiconductors. Additionally, high switching frequencies may cause electromagnetic interference, negatively impacting other devices.

Second, most industrial applications require high voltage conversion rates. Low-gain converters, such as conventional buck-boost converters, must operate at duty cycles close to zero/one to achieve high voltage step-down/step-up gains, which increases current stress in switches and diodes and raises conduction losses.

Third, to minimize conduction loss and semiconductor costs, low switch voltage stress is crucial, and the voltage level significantly influences the correct switch selection [9]–[11]. In [12]-[14], several high-gain converters are introduced that employ multilevel converters.

This method provides high gain and decreases the switches' voltage stress however the quantity of switches has increased. This results in increase in the cost and complexity of the control method, complicating the topology and control circuit.

In addition, switched capacitor (SC) circuits are used to increase the voltage rating [15]–[17]. The voltage gain is increased by this method but some converters based on SCs suffer from the high current transient issues. This problem has a negative effect on power density and decreases the efficiency [10], [18].

In [19], the voltage gain is achieved using a converter consisting of two boost converters. To increase the efficiency of traditional buck-boost converters, a circuit composed of a cascaded step-up-step-down converter along with an extra capacitor is suggested [20]. A bidirectional two-phase topology with high voltage gain is presented in [21]. In [22], a DC chopper with bidirectional functionality and soft switching capability is suggested**.** The voltage gain rises but is contingent on the switching frequency**.**

The paired inductors are employed to achieve a notably high step-down gain in [8], [10], [22]–[26]. This method has several benefits. The high step-down of step-up gain can be achieved by using a turn ratio. Furthermore, they can be controlled by conventional PWM control. In [10] high voltage gain is provided by employing a voltage doubler cell connected the buck-boost BDC. The coupled inductor is used to increase voltage gain based on the turn ratio. A high voltage gain BDC with a coupled inductor is proposed in [22], but the voltage gain is limited compared to the others. The bidirectional interleaved buck-boost linked to a dual active half-bridge provides significant voltage gain by utilizing a coupled inductor as shown in [23]**.** In [24], a method of combining voltage amplification modules and coupled inductors is used to achieve a high step-up/down voltage conversion. In [25], a proposal includes a two-phase converter on the low voltage side alongside a parallel high voltage series converter that features coupled inductors to obtain significant voltage amplification. The topology proposed by [26] provides high voltage gain by employing two coupled inductors. In [27], a proposal features a bidirectional design with high gain for a BDC converter, integrating a dual active half-bridge (DAHB) with a high-gain interleaved DC-DC converter through the use of a coupled inductor.

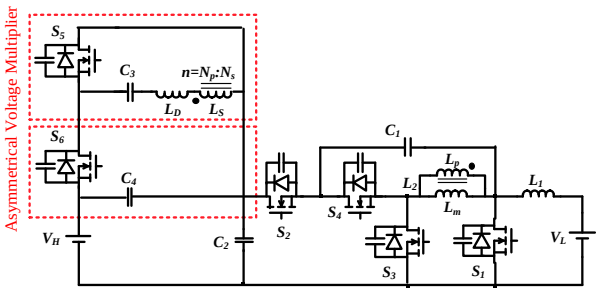

Fig. 1. The schematic of proposed converter.

The design provides multiple important benefits, such as high voltage amplification, two-way power flow, and soft switching to minimize energy losses. Ref. [28] employs two coupled inductors to achieve a high voltage gain. Although this results in a higher voltage gain, it also increases the overall volume of the passive components.

This paper proposes a non-isolated bidirectional DC-DC converter that has soft switching capability for the keys and offers higher voltage gain than competitors by using an asymmetric voltage multiplier cell.

II. Proposed Converter

This converter, obtained from the acknowledged converters in [11] and [24], is illustrated in Fig. 1. The suggested converter enhances the voltage gain in comparison to [11] and [24]. The system includes of a two-phase step-up-step-down converter composed of switches S_1, S_2, S_3 and S_4, capacitors C_1 and C_2 and inductor L_1 at the low-side input. The converter consists of a voltage amplification cell consisting of capacitors C_4 and C_3, switches S_5 and S_6 and an inductor L_D, forming an asymmetric voltage gain converter. Additionally, the coupled inductor, L_2, is characterized by its primary winding, np, a secondary winding, ns and a magnetic inductance, L_m. The leakage inductance of the coupled inductor is combined with an L_D inductance structure.

A. Operating Principle

Switches S_2 and S_4 operate in reverse to switches S_1 and S_3. The duty cycle for switches S_2 and S_4 is identical to the value of D. α is the amount of overlap for S_3 and S_1, which is defined as α=D-0.5. Switches S_6 and S_5 operate in reverse of each other with a duty cycle of 0.5. Dφ represents the phase difference between switches S_5 and S_1, While the S_1 gate pulse has a phase difference of π with the S_2 gate pulse (along with S_3 and S_4). This converter functions across twelve intervals during one switching period. The various states during a switching period for Dφ >α are detailed below.

For easier analysis of the steady state of the proposed converter, the following assumptions are made:

- The ripple current of inductor L_1 is ignored because it is sufficiently large

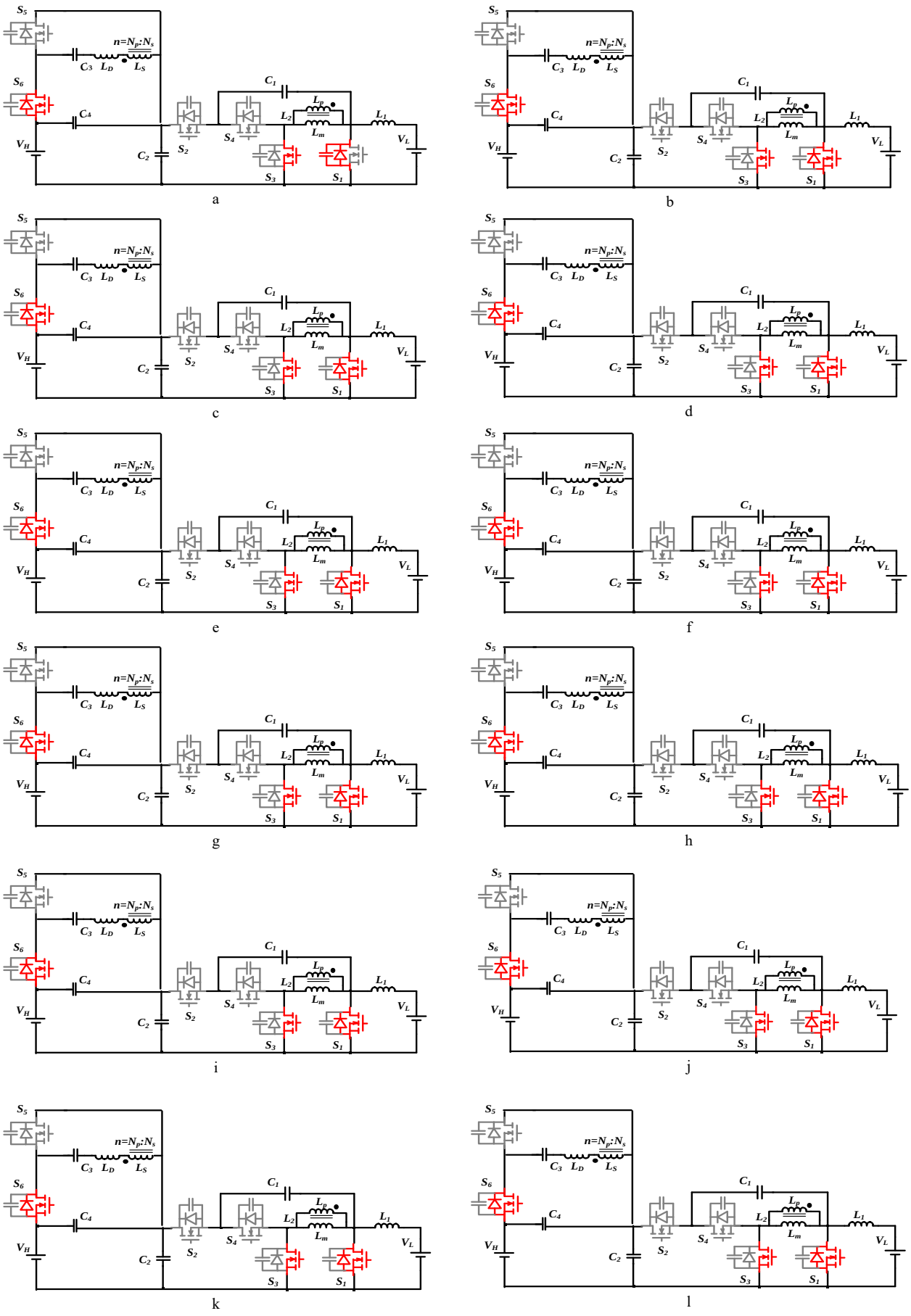

Fig. 2. Equivalent circuit for 12 modes in high step-up operation. (a) Mode 1, (b) Mode 2, (c) S Mode 3, (d) Mode 4, (e) Mode 5, (f) Mode6, (g) Mode 7, (h) Mode 8, (i) S Mode 9, (j) Mode 10, (k) Mode 11, and(l) Mode12

- The voltage ripple of C_1 to C_4, is ignored because they are sufficiently large.
- It is assumed that the elements of converter are ideal, considering only the drain-source capacitances of the MOSFETs in the circuit.
- n is equal to the turn ratio of the coupled inductor, denoted as n = ns/np, and the magnetic coupling K is assumed to be one.
- The capacitors of MOSFETs, C_{ds1} to C_{ds6}, become completely charged and discharged throughout the dead time.
- The diodes connected in parallel to the switches are rapid recovery diodes.

Mode 1 ($t_0<t<t_1$)

This interval starts when switch S_2 is switched off. Since the sum of the initial current of the transformer primary current and capacitor C_1 current is greater than the current i_{L1} (current of input inductor, L_1) at time t_0, the capacitor at drain-source of switch S_1 is initially discharged, after which the body diode under ZVS conditions begins to conduct.

Mode 2 ($t_1<t<t_2$)

When this interval begins, the S_1 switch starts functioning with ZVS situations. As S_6 switch is currently on, the voltage of L_D (V_{LD}) becomes negative, leading to a reduction in the flow of current through it. The formulas for the circuit in mode 2 can be expressed as (1):

$$\begin{cases} V_{Lm} = 0, V_{L1} = V_L, V_{LD} = V_{C3} - V_{C4} \\ I_{C1} = 0, I_{C2} = -I_H, I_{C3} = -I_{LD}, I_{C4} = -I_H + I_{LD} \end{cases} \quad (1)$$

Where I_H denotes the current associated with the voltage of high side (V_H) and V_{Lm} is the voltage of the inductor L_m. Hence, Equation (2) shows the inductor current in state 2.

$$\begin{cases} i_{Lm}(t) = i_{Lm}(t_0) \\ i_{LD} = i_{LD}(t_0) + \dfrac{V_{C3} - V_{C4}}{L_D} t \end{cases} \quad (2)$$

Mode 3 ($t_2<t<t_3$)

When this period begins, switch S_3 has been turned off, and then the body diode of S_4 starts conducting. Under this condition, the voltage of the magnetic inductor Lm becomes negative and not equal to zero. As a result, the Lm current is decreased.

Mode 4 ($t_3<t<t_4$)

Under these situations, Switch S_4 begins to function with ZVS operation. In this period, the voltage of L_D is more negative than in the previous two time frames and nears its minimum value with a steeper slope. In mode 4 the equations related to the circuit are as follows (3):

$$\begin{cases} V_{Lm} = -V_{C1}, V_{L1} = V_L, V_{LD} = -nV_{C1} + V_{C3} - V_{C4} \\ I_{C1} = I_{Lp}, I_{C2} = -I_H, I_{C3} = -I_{LD}, I_{C4} = -I_H + I_{LD} \end{cases} \quad (3)$$

Thus, the equations i_{LD} and i_{Lm} for mode 4 can be represented as (4):

$$\begin{cases} i_{Lm}(t) = i_{Lm}(t_2) - \dfrac{V_{C1}}{L_m} \\ i_{LD} = i_{LD}(t_2) + \dfrac{-nV_{C1} + V_{C3} - V_{C4}}{L_D} t \end{cases} \quad (4)$$

Mode 5 ($t_4<t<t_5$)

This interval starts when the switch S_6 is turned off. First, capacitor C_{ds5} is discharged by current i_{LD} and then the capacitor C_{ds6} starts charging. which causes the diode of switch S_5 to conduct with ZVS situations.

Mode 6 ($t_5<t<t_6$)

Starting from this period, switch S_5 operates with ZVS situation. While the current i_{LD} remains constant, the voltage across inductor L_D is almost zero. The voltage across inductor L_m is likewise negative and, with a slope identical to the prior segment, it attains its lowest value at the conclusion of this segment. The circuit equations in mode 6 can be represented as (5):

$$\begin{cases} V_{Lm} = -V_{C1}, V_{L1} = V_l, V_{LD} = -nV_{C1} + V_{C3} \\ I_{C1} = I_{Lp}, I_{C2} = -I_H, I_{C3} = -I_{LD}, I_{C4} = -I_H \end{cases} \quad (5)$$

So, it can be concluded (6),

$$nV_{C1} = V_{C3} \quad (6)$$

For mode 6, the currents i_{Lm} and i_{LD} can be expressed by the equations given as follows (7):

$$\begin{cases} i_{Lm}(t) = i_{Lm}(t_4) - \dfrac{V_{C1}}{L_m} \\ i_{LD} = i_{LD}(t_4) + \dfrac{-nV_{C1} + V_{C3}}{L_D} t \end{cases} \quad (7)$$

Mode 7 ($t_6<t<t_7$)

Mode 7 begins when the S_4 switch is turned off. The current (I_p), which the drain-source capacitor of switch S_3 is discharged by the current on the primary side of the transformer. and then the body diode of the switch S3 conducts under ZVS situation.

Mode 8 ($t_7<t<t_8$)

During this time, switch S_4 starts operating with ZVS situation. The voltage of L_D becomes positive when switch S_5 is activated, resulting in a rising current flowing through it. The circuit's equations in mode 8 can be represented as (8):

$$\begin{cases} V_{Lm} = 0, V_{L1} = V_L, V_{LD} = V_{C3} \\ I_{C1} = 0, I_{C2} = -I_H, I_{C3} = -I_{LD}, I_{C4} = -I_H \end{cases} \quad (8)$$

Thus, the i_{LD} and i_{Lm} equations for case 8 will be as follows (9):

$$\begin{cases} i_{Lm}(t) = i_{Lm}(t_6) \\ i_{LD} = i_{LD}(t_6) + \dfrac{V_{C3}}{L_D} \end{cases} \quad (9)$$

Mode 9 ($t_8<t<t_9$)

During this time interval, switch S_1 is inactive and due to the active rectification function of switch S_2, the diode on the body of transistor S_2 starts to conduct. In this condition, the voltage of the magnetic inductance L_m becomes positive.

Mode 10 ($t_9<t<t_{10}$)

At this stage, due to the ZVS condition for switch S_2, this switch conducts. At this stage, the L_D voltage increases positively and approaches its peak value with a sharper incline. The circuit equations in mode 10 can be represented as (10):

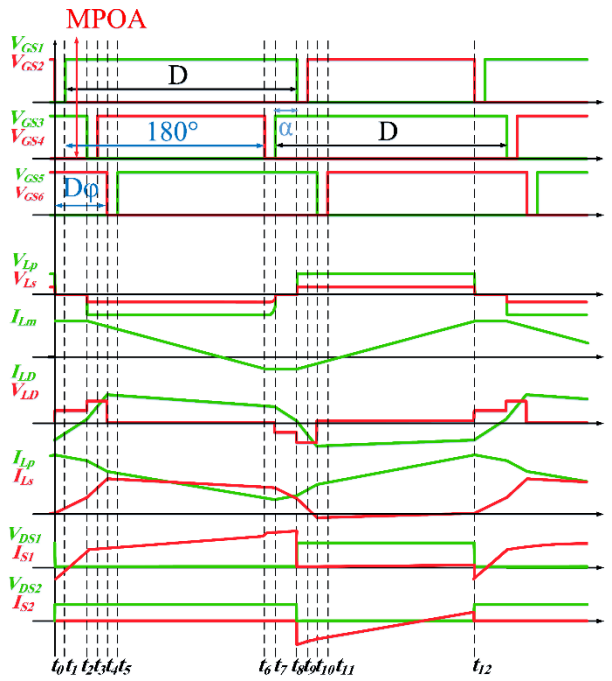

Fig. 3. Theoretical waveforms throughout a switching interval of the suggested converter in step-up operation mode

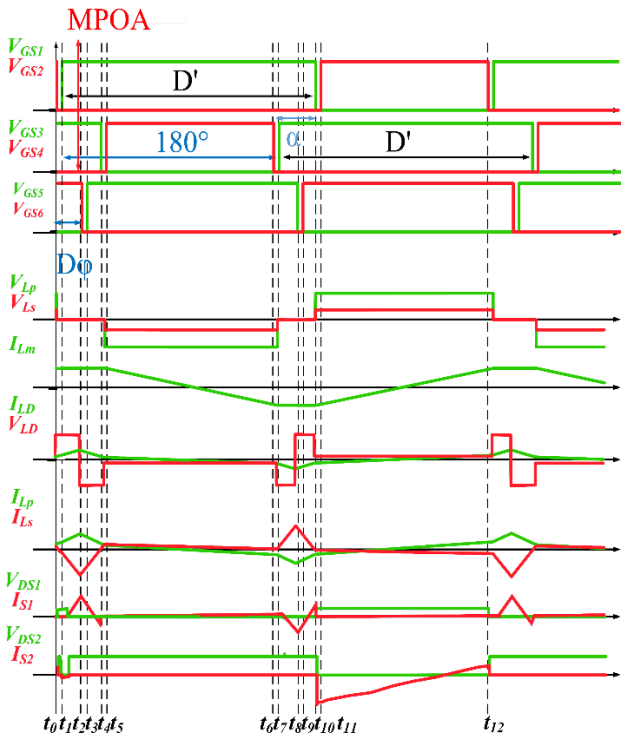

Fig. 4. Theoretical waveforms throughout the switching interval of the proposed converter in step-down operation mode

$$\begin{cases} V_{Lm} = V_{C2} - V_{C1}, V_{L1} = V_L - V_{C2} + V_{C1}, \\ V_{LD} = nV_{C2} - nV_{C1} + V_{C3} \\ I_{C1} = -I_{L1} + I_{Lp}, I_{C2} = -I_H + I_{L1} - I_{Lp} \\ I_{C3} = -I_{LD}, I_{C4} = -I_H \end{cases} \quad (10)$$

The current that flows through the primary winding of the coupled inductor is defined as. Thus, the formulas for i_{LD} and i_{Lm} in mode 10 can be represented as (11):

$$\begin{cases} i_{Lm}(t) = i_{Lm}(t_8) + \dfrac{V_{C2} - V_{C1}}{L_m} \\ i_{LD} = i_{LD}(t_8) + \dfrac{nV_{C2} - nV_{C1} + V_{C3}}{L_D} \end{cases} \quad (11)$$

Mode 11 ($t_{10}<t<t_{11}$)

This time state begins when the S_5 switch is switched off. At first, capacitor C_{ds6} is discharged by current i_{LD}, and subsequently, the diode of S_6 activates under ZVS situation.

Mode 12 ($t_{11}<t<t_{12}$)

In this mode, ZVS conditions are created for switch S_6 so it starts conducting. The L_D voltage is near zero while the i_{LD} current remains constant. The voltage of L_m is above zero, and its current attains its peak value at the conclusion of its ramp, keeping the same slope as the previous mode. The formulas for the circuit in interval 12 represented in this way (12):

$$\begin{cases} V_{Lm} = V_{C2} - V_{C1}, V_{L1} = V_L - V_{C2} + V_{C1}, \\ V_{LD} = nV_{C2} - nV_{C1} + V_{C3} - V_{C4} \\ I_{C1} = -I_{L1} + I_{Lp}, I_{C2} = -I_H + I_{L1} - I_{Lp}, \\ I_{C3} = -I_{LD}, I_{C4} = I_{LD} - I_H \end{cases} \quad (12)$$

Therefore, the equations i_{LD} and i_{Lm} for mode 13 can be expressed as (13):

$$\begin{cases} i_{Lm}(t) = i_{Lm}(t_{10}) + \dfrac{V_{C2} - V_{C1}}{L_m} \\ i_{LD} = i_{LD}(t_{10}) + \dfrac{nV_{C2} - nV_{C1} + V_{C3} - V_{C4}}{L_D} \end{cases} \quad (13)$$

Figs. 2(a-l) and 3 show the operating range and key waveforms of this converter.

It is essential to note that the converter operates in two modes: it functions in step-down mode when $\alpha>D\varphi$ and in step-up mode when $\alpha<D\varphi$, where α signifies the overlap of switches S_3 and S_1, and D denotes the duty cycle of switches S_3 and S_1. It has been mentioned previously that the duty cycle have to be greater than 0.5 to ensure smooth switching of the circuit switches, and $D\varphi$ indicates the time difference between the activation signals for transistors S_5 and S_1. The reference point for phase shift is the duration when S_1 and S_3 operate simultaneously (MPOA, Middle Point of Overlapping Area).

The functioning of a converter in the buck mode is typically akin to the boost mode. To gain a clearer insight into how a step-down mode functions, the theoretical key waveforms associated with it are illustrated in Fig. 4. Additionally, Table I displays the active switches for both modes of step-down and step-up during each interval.

The functioning of a converter in the buck mode is typically akin to the boost mode. To gain a clearer insight into how a step-down mode functions, the theoretical key waveforms associated with it are illustrated in Fig. 4. Additionally, Table I displays the active switches for both modes of step-down and step-up during each interval.

TABLE I
Active Switches During each Interval in Step-up and Step-Down Modes

Time interval	step-up mode	step-down mode
t_0-t_2	$S_1S_3S_6$	$S_1S_3S_6$
t_2-t_4	$S_1S_4S_6$	$S_1S_3S_5$
t_4-t_6	$S_1S_4S_5$	$S_1S_4S_5$
t_6-t_8	$S_1S_3S_5$	$S_1S_3S_5$
t_8-t_{10}	$S_2S_3S_5$	$S_1S_3S_6$
t_{10}-t_{12}	$S_2S_3S_6$	$S_2S_3S_6$

III. ANALYSIS AND DESIGN

A. Voltage Gain in Step-Up Modet

Equation (14) shows the voltage on the upper side of the suggested converter. This equation is obtained using the KVL law for the high-side voltage of this converter.

$$V_H = V_{C2} + V_{C4} \tag{14}$$

The voltage gain of the boost converter configuration is obtained as (15) using the volt-second law on the inductors Lm and L_1.

$$\begin{cases} V_{C1} = \dfrac{V_{C2}}{2} \\ \dfrac{V_{C2}}{V_L} = \dfrac{2}{1-D} \end{cases} \tag{15}$$

Equation (16) is obtained by assuming that in the stable condition the voltage of the L_D is approximately zero.

$$\frac{n_s}{n_p} = \frac{V_{C4}}{V_{C2}} = \frac{V_{C4}}{2V_{C1}} = n \tag{16}$$

Equation (17) shows the output voltage gain of the suggested converter operating in boost mode, taking into account equations (14) to (16).

$$G_H = \frac{V_H}{V_L} = \frac{2(n+1)}{1-D} \tag{17}$$

B. Component Design

According to the various modes of the suggested converter, for switches S_1 to S_6, the maximum voltage stress is determined as follows (18):

$$\begin{cases} V_{max,S1} = V_{max,S2} = V_{max,S3} = \dfrac{V_L}{1-D} = \dfrac{V_H}{2(n+1)} \\ V_{max,S4} = \dfrac{2}{1-D} V_L = \dfrac{V_H}{n+1} \\ V_{max,S5} = V_{max,S6} = \dfrac{2n}{1-D} V_L = n\dfrac{V_H}{n+1} \end{cases} \tag{18}$$

The existing stress on the switches can be articulated as (19):

$$\begin{cases} I_{max,S1} = I_{max,S3} = \\ \dfrac{P_{High}}{V_L} + \dfrac{V_L D}{f_s L_1} + \dfrac{V_L D}{2_{Lm}(1-D) f_s} + \dfrac{nV_{C4}}{4L_D f_s}(2D_\varphi - \alpha) \\ I_{max,S2} = I_{max,S4} = \\ \dfrac{nV_{C4}}{4L_D f_s}\alpha + \dfrac{P_{High}}{V_L} + \dfrac{V_L D}{f_s L_1} + \dfrac{V_L D}{2_{Lm}(1-D) f_s} \\ I_{max,S5} = I_{max,S6} = \dfrac{nV_{C4}}{4L_D f_s}(2D_\varphi - \alpha) \end{cases} \tag{19}$$

where f_s is the switching frequency.

Using the value of the inductor current ripple, the value of the inductors can be determined as follows (20):

$$\begin{cases} \Delta i_{L1} = \dfrac{V_L D}{L_1 f_s} \\ \Delta i_{Lm} = \dfrac{V_L D}{L_m f_s (1-D)} \end{cases} \tag{20}$$

The capacitor's voltage can be determined using equations (6), (15), and (16). The potential of the capacitors can be determined from the output voltage as (21).

$$\begin{cases} V_{C1} = \dfrac{V_H}{2(n+1)} \\ V_{C2} = \dfrac{V_H}{n+1} \\ V_{C3} = \dfrac{nV_H}{2(n+1)} \\ V_{C4} = \dfrac{nV_H}{n+1} \end{cases} \tag{21}$$

The capacitance of capacitors can be determined by their voltage ripple as (22):

$$\begin{cases} \Delta V_{C1} = \dfrac{2I_{L1}(1-D)}{f_s C_1} \\ \Delta V_{C2} = \dfrac{I_H D}{f_s C_2} \\ \Delta V_{C3} = \dfrac{I_H}{f_s C_3} \\ \Delta V_{C4} = \dfrac{0.5 I_H}{f_s C_4} \end{cases} \tag{22}$$

C. Power Transfer Analysis

According to the suggested converter, the conveyed power can be expressed as (23):

$$P_{total} = (V_{C2} + V_{C4}) I_H \tag{23}$$

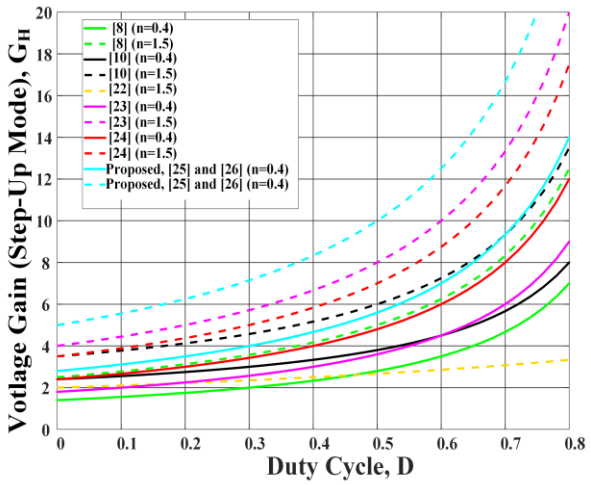

a

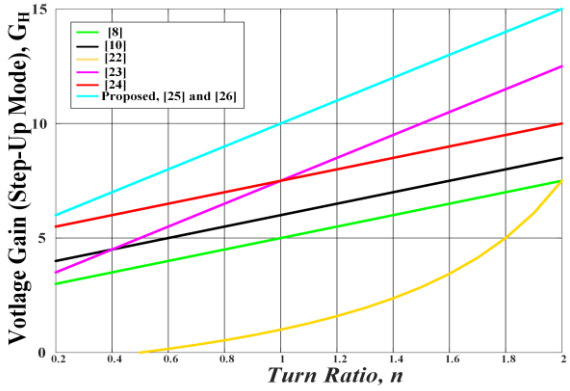

b

Fig. 5. Comparison of voltage gain a versus duty cycle for same turn ratio, and b versus turn ratio for same duty cycle.

To calculate the power component transmitted by the voltage boost cell, middle of current value of switches S_5 and S_6 during one switching cycle should be multiplied by the voltage factor of capacitor C_4 as described in (24):

$$P_{total} = V_{C2} + 3V_{C4}f_s \int_0^{Ts} i_{S5}dt \quad (24)$$

The equations of power for the two operating modes of the suggested converter are obtained after calculating the middle of current of switches S_6 and S_5 with the state equations.

$$For \ \frac{a}{2} < D_\varphi < a$$

$$P_{total} = \frac{V_H^2}{4L_D f_s}\frac{n}{n+1}(\alpha D - 2D_\varphi - \alpha - 2DD_\varphi) \quad (25)$$

and $for \ D_\varphi > a$

$$P_{total} = \frac{V_H^2}{4L_D f_s}\frac{n}{n+1}$$
$$(2D_\varphi - 2DD_\varphi + 4D_\varphi\alpha - \alpha + D\alpha - 2\alpha^2 - 2D_\varphi^2) \quad (26)$$

Equations (23)–(26) show that the transmitted power is affected by the phase shift angle Dφ and the duty cycle D. As the duty cycle is defined by the output and input voltages, the power transfer is regulated by the phase shift. As a result, the converter is capable of functioning with various voltages and power levels.

To ensure ZVS for 6 switches require the inductance Lm must be designed considering the worst-case condition. The condition for ZVS is provided in Equation (27).

$$L_m < \frac{L_D(1-D)}{n\frac{(n+1)}{(1-D)}(A) - n^2(2D_\varphi - \alpha)} \quad (27)$$

$$A = 2D_\varphi - 2DD_\varphi + 4D_\varphi\alpha - \alpha + D\alpha - 2\alpha^2 - 2D_\varphi^2$$

IV. Comparison

This part provides a comparison between the proposed converter and the other BDC converters mentioned in the introduction, as indicated in Table II. In the literature, several methods for DC-DC converters with high step-down/step-up voltage gain are introduced which among them the converters based on coupled inductors are one of the popular approaches to provide high voltage gain. In fact, the topology design approach for BDC converters aimed at achieving a high voltage gain which can be one of the main objectives. Hence, Fig.5 shows the voltage gain comparison of the suggested structure with competing. In the figure, the variations of the voltage amplification in boost configuration are illustrated when the duty cycle and the turn ratio are changed in the range of interest. These variations are plotted in MATLAB. The voltage gain versus duty cycle for the same turn ratio is shown in Fig. 5 (a) while the relationship between voltage gains and turn ratio for a constant duty cycle is shown in Fig. 5 (b). It is evident that the suggested converter offers the ultra gain of voltage when compared to the voltage gains presented in references[8], [10], [22]–[24]. Additionally, it achieves the same voltage level with fewer semiconductor components in comparison to references [25] and [26]. Additionally, the suggested converter offers a higher gain of voltage compared to those in [10] and [21]. The voltage gain of [21] is solely dependent on the duty cycle and the voltage gain of [10] is like [8]. So, the suggested converter offers a significantly higher voltage gain. The details of the specification of the converters are presented in Table II. Also, the suggested converter offers the highest step-down voltage gain compared to others. Furthermore, the suggested converter establishes common ground between the output and input terminals and also has current continuity on the side of low voltage. These features improve converter performance compared to the others. A high voltage gain BDC is suggested based on a reversal coupled inductor in [23]. It is evident that the equation for voltage gain in boost mode includes the turn ratio as a fractional term in the voltage gain formula's denominator. So, it may decrease voltage gain with a high turn ratio and lead to instability with a low turn ratio. As it can be seen, the number of elements of the proposed converter and [24] are almost equal, but the suggested converter offers higher gain of voltage compared to [24]. In [25] a high voltage gain BDC based on coupled inductor and voltage is presented. Likewise observed, the voltage gain is limited compared to the suggested converter and also the input and output currents are discontinuous. The converter proposed by [26] provides the same voltage gain, but the number of semiconductors is higher than the proposed here and the current of the low side is not continuous. Moreover, there is no common ground at input and output terminals in [25] . The proposed converter presented by [26] offers the same voltage gain, but the number of semiconductors is too high. Furthermore, it uses two coupled inductors to provide high voltage gain.

The comparison table illustrates the total voltage stress on semiconductor elements in the proposed converter compared

to others. As can be seen, the proposed converter experiences lower voltage stress than converters with the same voltage gains, resulting in reduced costs and increased efficiency. Moreover, the overall voltage stress on switches.

exhibits only a marginal difference compared to converters with a minor voltage gain, while the gain of voltage is significantly higher. In addition, the suggested converter provides interleaved capabilities that can diminish enhance power quality and the input current ripple.

V. Experimental Results

In this section, the experimental results are presented. Before conducting an experimental assessment of the converter's performance, it was initially simulated using PSIM software. Subsequently, a laboratory setup was constructed and utilized to verify the operational and analytical findings of the suggested converter. The conditions and parameters of the converter for testing are provided in Table III. The prototype for the BDC is depicted in Fig. 6. The results of the experiment are presented for boost mode. Thus, input voltages of 50 V DC and output voltage of 300 V DC are considered, a value frequently utilized in industries like single-phase inverters and electric vehicles. Notably, different input and output voltages can be obtained by altering the design through the use of equations (14)-(26).

The EE42 ferrite core is encased by the coupled inductor, whereas the L_D and input inductors are wrapped around toroidal cores. (Due to its efficiency, accessibility, and affordability) That features an air gap in its legs. A controller board utilizing the STM32F303RBT microcontroller and TLP350 gate drivers generates PWM signals in a loop control system. (to evaluate the performance and operational modes of the converter). Fig. 6(b) displays the control board. The control board consists of three parts: the flyback power supply, the microcontroller, and the gate drivers. For generating gate signals, the microcontroller provides three PWM channels. The circuits for the gate driver consist of six TLP350.

Fig. 7 presents the experimental findings for the buck and boost configurations. The stable waveforms of Fig. 7(a) show the current and input/output voltages of the proposed converter. The input voltage (V_{Low}) is 50V DC in the step-up mode, while the high-side voltage (V_{High}) is maintained at 301.2V DC. The efficiency measured at the nominal output power, is 96.23%. Fig. 7(b) show the voltage of capacitors C_1 to C_4. The signals produced by gate drivers are illustrated in Fig. 7(c). The gate signal of S_3 (V_{gs3}) is 180 degrees behind the gate signal of S_1 (V_{gs1}). The signal of gates for switches S_1, S_3, and S_5 are opposite to those of switches S_2, S_4, and S_6. Fig. 7(d) show the voltage of the switches S_1 and S_2 (V_{DS1} and Fig. 7 presents the experimental findings for the buck and boost configurations. The stable waveforms of Fig. 7(a) show the current and input/output voltages of the proposed converter. The input voltage (V_{Low}) is 50V DC in the step-up mode, while the high-side voltage (V_{High}) is maintained at 301.2V DC. The efficiency measured at the nominal output power, is 96.23%. Fig. 7(b) show the voltage of capacitors C_1 to C_4. The signals produced by gate drivers are illustrated in Fig. 7(c). The gate signal of S_3 (V_{gs3}) is 180 degrees behind the gate signal of S_1 (V_{gs1}). The signal of gates for switches S_1, S_3, and S_5 are opposite to those of switches S_2, S_4, and S_6. Fig. 7(d) show the voltage of the switches S_1 and S_2 (V_{DS1} and V_{DS2}).

TABLE II
Comparison Among Various BDC

Feature	Proposed Converter	[26]	[25]	[24]	[23]	[22]	[10]	[8]
No. of semiconductors	6	8	7	4	6	4	4	4
No. of inductors	2	-	-	-	2	-	-	-
No. of coupled inductor	1	2	2	1	1	1	1	1
No. of capacitors	4	4	3	2	3	2	2	3
Voltage gain (boost mode)	$\frac{2(n+1)}{1-D}$	$\frac{2(n+1)}{1-D}$	$\frac{2(n+1)}{1-D}$	$\frac{n+2}{1-D}$	$\frac{2n+1}{1-D}$	$\frac{2n-1}{(n-1)(1-D)}$	$\frac{2+n-D}{1-D}$	$\frac{n+1}{1-D}$
Voltage gain (buck mode)	$\frac{D'}{2(n+1)}$	$\frac{D'}{2(n+1)}$	$\frac{D'}{2(n+1)}$	$\frac{D'}{n+2}$	$\frac{D'}{2n+1}$	$\frac{(n+1)D'}{2n-1}$	$\frac{D'}{1+n+D'}$	$\frac{D'}{n+1}$
Total voltage stress across semiconductors/ V_H	$\frac{4n+5}{2n+2}$	$\frac{6n+5}{2n+2}$	$\frac{6n+8}{2n+2}$	2	$\frac{4n+4}{2n+1}$	2	2	$2+\frac{2n}{1-D}$
Reported efficiency at nominal power in boost mode (%)	96.23	94.9	96.3	96	97	95.22	97	95.2
Continuous input current at low voltage side	Yes	Yes	No	No	Yes	No	No	No
Common ground between input/output	Yes	Yes	No	No	Yes	Yes	Yes	Yes

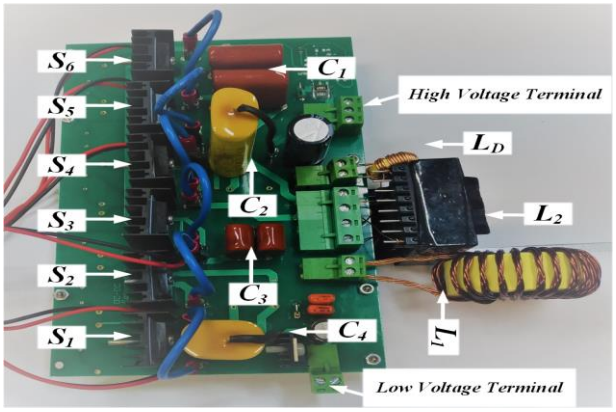

a

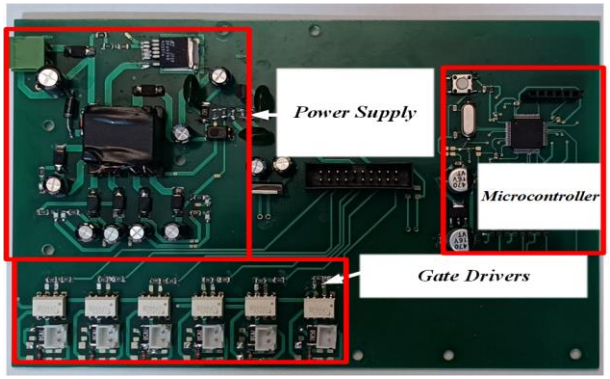

b

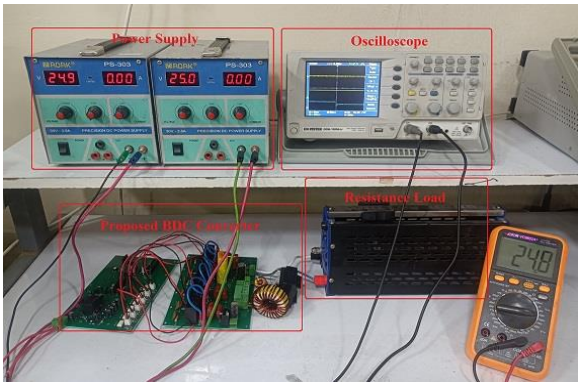

c

Fig. 6. Experimental prototype, a power converter, b gate drivers and microcontroller, c experimental setup.

The voltage stress for these switches is identical to that determined in equation (18). The waveforms corresponding to the voltages of switches S_3, S_4, and S_6 are shown in Fig. 7(e) displays the voltage waveforms for switches S_3, S_4, and S_6.

Fig. 7 (f) show the waveforms of voltage and current for both the primary and secondary of the coupled inductor. The voltage waveforms for the primary and secondary are represented as V_{Lp} and V_{Ls}, respectively. The currents in the primary and secondary windings of the coupled L_2, are represented as I_{Lp} and I_{Ls}, respectively. Different waveforms of multiple components of the proposed converter are shown to confirm the performance of the converter. To verify the ZVS functioning of the converter, the enlarged view of the waveforms is shown in Figs 7(g)-(i). The voltage, current, and input gate for switches S_1 and S_3 are illustrated in Fig. 7 (g) and (h).

TABLE III
Experimental Condition and Parameters

Parameters	Value
P_o ,Output power	350 W
V_{High} ,High voltage	300 V_{dc}
V_{Low} ,Low voltage	50 V_{dc}
f_s ,Switching frequency	50 kHz
L_D *and* L_{in} ,Inductors	47µH ,100µH
L_m ,Coupled Inductor, , turn ratio	250µH, 0.37
C_1, C_2, C_3 & C_4,capacitors	10µF, 12µF. 10µF, 12µF
S_1, S_2 & S_3,Switches	IRFP260NPBF
S_4,Switch	IPW60R060P7
S_5 & S_6,Switches	IRFP150NPB

Fig. 7(i) additionally presents findings for the input gate and voltage of switch S_5. Additionally, the waveform of the magnetizing current for the coupled inductor is displayed in Fig. 7(i). It is evident that zero-voltage switching is available for the switches. Thus, the power loss is reduced, and the switch activates under soft switching conditions. Fig. 8 shows the outcomes for buck mode functionality. Fig. 7(j) shows the signal gates of switches S1, S_3, and S_5. The signal gates of switches S_2, S_4, and S_6 are opposite to those of switches S_1, S_3, and S_5. The input voltage for buck operation is 300V, producing an output voltage of 49.87V. Fig. 7(k) illustrates the voltage across the capacitors, whereas Fig. 7(l) represents the voltage across switches S_1, S_3, and S_5. The outcomes for buck mode indicate that the converter delivers strong performance across various components.

The distribution of power loss is determined using the RMS current, current and voltage waveforms, peak voltage, along with the switching frequency. Fig. 8 illustrates the efficiency results for various load conditions. For load levels between 80% and nominal power, the efficiency is greater than 96%.

Consequently, the experimental results validate the effective operation of the suggested converter, demonstrating its appropriateness for multiple applications. The result of experimental confirm the efficient operation of the suggested converter, demonstrating its appropriateness for multiple applications.

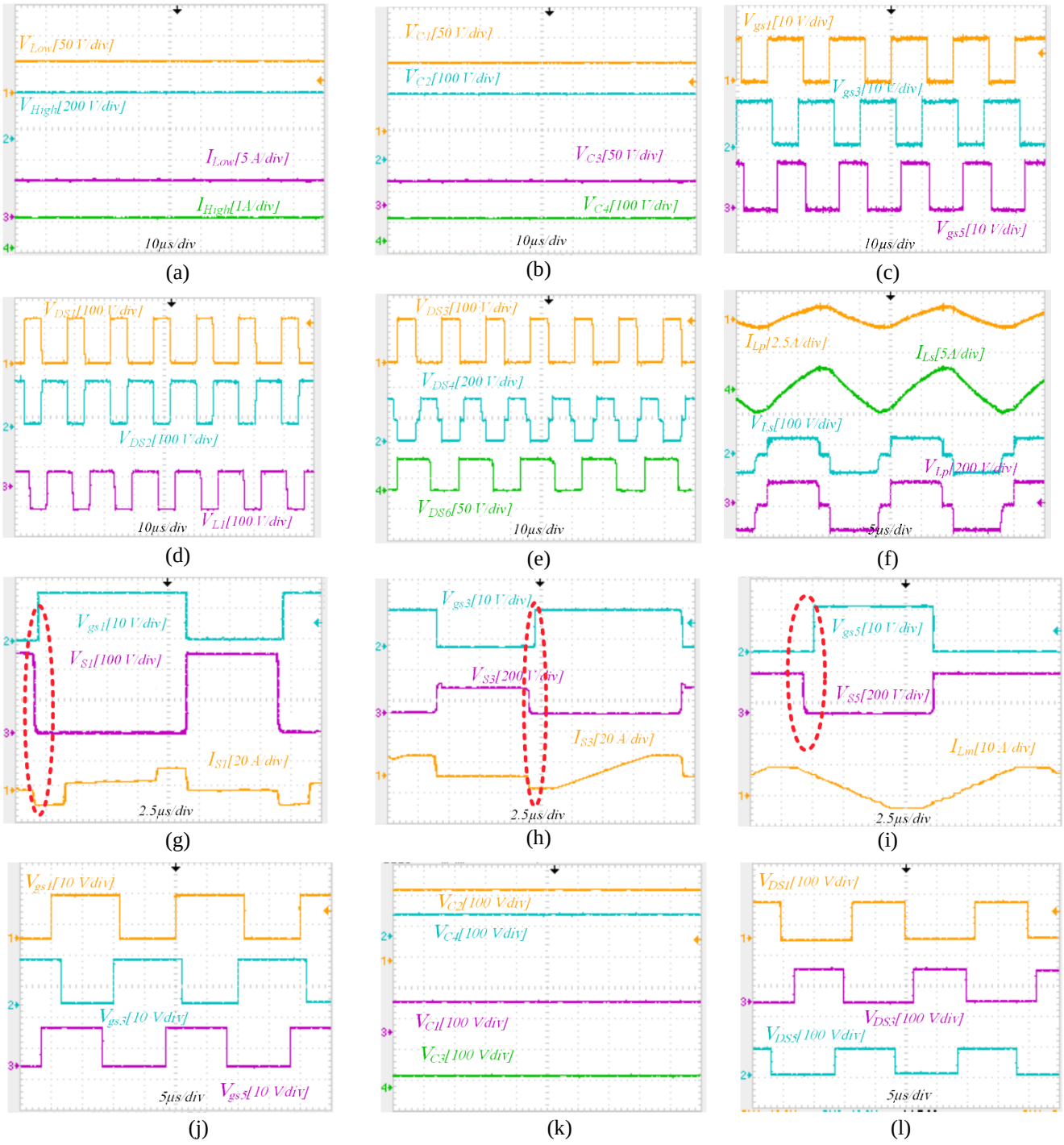

Fig. 7. Experimental data includes (a) waveforms for input and output, (b) voltages of capacitors, and (c) input gate measurements for switches S1, S3, and S5, (d) the voltage across S1 and S2, along with the voltage across the input inductor, (e) voltages of S3, S4, and S6, (f) voltage and current waveforms for the coupled inductor, (g) a detailed view of the input gate, voltage, and current for switch S1, (h) a detailed view of the input gate, voltage, and current for switch S3, and (i) a detailed view of the input gate, voltage for switch S5, and the magnetizing current for the coupled inductor. Additionally, (j) input gate data for switches S1, S3, and S5, (k) voltages across capacitors, and (l) voltages of switches S1, S3, and S5

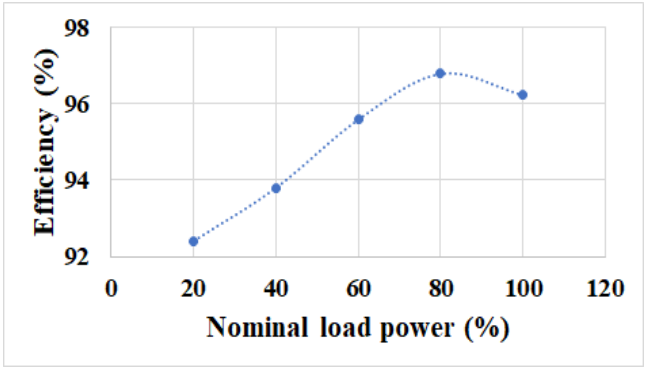

Fig. 8. The efficiency curve as a function of nominal power.

VI. Conclusion

This paper presented an innovative power converter featuring a high voltage gain BDC through the use of a Asymetrical Voltage Multiplayer cell, a coupled inductor, and two-phase boost converter. Various switching modes of the converter are examined, and equations for each mode are presented. Additionally, the design equations for various elements are outlined. The suggested converter offers the greatest voltage gain in comparison to many competitors and contains fewer components than other converters with equivalent voltage gain. Additionally, it provides a steady

current on the low voltage side. ZVS switching is implemented, enhancing the efficiency of the converter. Using an asymmetrical design of the voltage multiplier cell can reduce total losses due to the voltage distribution strategy and reduced peak currents. The experimental findings indicate that the converter's performance is satisfactory and that it can deliver a high voltage from a low voltage according to pre-defined specifications.

ACKNOWLEDGMENT

The authors acknowledge Semnan University.

FUNDING STATEMENT

This research received no specific grant from any funding agency in the public, commercial, or not-for-profit sectors.

CONFLICTS OF INTEREST

The second author is a Director-in-Charge for Modeling and Simulation in Electrical and Electronics Engineering Journal and was not involved in the editorial review or the decision to publish this article.

AUTHOR'S CONTRIBUTION STATEMENT

Conceptualization and study design: (Madai, Molla-Ahmadian)
Data collection and experimentation: (Madai, Jazaeri, Molla-Ahmadian)
Data analysis and interpretation: (Madai, Jazaeri, Molla-Ahmadian)
Manuscript writing and editing: (Madai, Jazaeri, Molla-Ahmadian)
Supervision and project administration: (Jazaeri, Molla-Ahmadian)

AI DISCLOSURE

AI was used only as a tool for language editing.

REFERENCES

[1] M. Babaei, S. Sharifi, and M. Monfared, “A Z-source network integrated buck–boost PFC rectifier,” Int. J. Ind. Electron., Control Optim., vol. 2, no. 2, pp. 289–296, Oct. 2019, doi: 10.22111/ieco.2018.26296.1073.

[2] K. Varesi and S. Padmanaban, “A transformer-less high-boosting common-grounded multi-phase DC–DC converter with continuous input-current favourable for low-power applications,” IET Renew. Power Gener., vol. 16, no. 3, pp. 594–604, Mar. 2022, doi: 10.1049/rpg2.12591.

[3] S. O. Golpayegani, M. Jazaeri, and N. Eskandarian, “Frequency domain analysis of dual active bridge converter considering all power loss elements,” J. Model. Simul. Electr. Electron. Eng., vol. 3, no. 2, pp. 45–56, Aug. 2023, doi: 10.22075/mseee.2024.33381.1149.

[4] M. Elmi, M. Banaei, and H. Afsharirad, “Study on a non-isolated high step-up SEPIC-based DC–DC converter with continuous input current for photovoltaic applications,” Int. J. Ind. Electron., Control Optim., vol. 3, no. 1, pp. 95–104, Mar. 2025, doi: 10.22111/ieco.2024.48587.1558.

[5] W. Li, X. He, D. Xu, and B. Wu, “General derivation law of nonisolated high-step-up interleaved converters with built-in transformer,” IEEE Trans. Ind. Electron., vol. 59, no. 3, pp. 1650–1661, Mar. 2012, doi: 10.1109/TIE.2011.2163375.

[6] A. Rodriguez, A. Vazquez, D. G. Lamar, M. M. Hernando, and J. Sebastian, “Different purpose design strategies and techniques to improve the performance of a dual active bridge with phase-shift control,” IEEE Trans. Power Electron., vol. 30, no. 2, pp. 790–804, Feb. 2015, doi: 10.1109/TPEL.2014.2309853.

[7] S. Zong, H. Luo, W. Li, Y. Deng, and X. He, “High-power bidirectional resonant DC–DC converter with equivalent switching frequency doubler,” IET Renew. Power Gener., vol. 10, no. 6, pp. 834–842, Jul. 2016, doi: 10.1049/iet-rpg.2015.0437.

[8] J. Hiltunen, V. Vaisanen, R. Juntunen, and P. Silventoinen, “Variable-frequency phase shift modulation of a dual active bridge converter,” IEEE Trans. Power Electron., vol. 30, no. 12, pp. 7138–7148, Dec. 2015, doi: 10.1109/TPEL.2015.2390913.

[9] M. Packnezhad, P. Talebi, and H. Farzanehfard, “Fully soft-switched high step-up/down bidirectional buck/boost converter with reduced switch voltage stress,” IET Power Electron., vol. 16, no. 1, pp. 105–115, Jan. 2023, doi: 10.1049/pel2.12457.

[10] M. Forouzesh, Y. P. Siwakoti, S. A. Gorji, F. Blaabjerg, and B. Lehman, “Step-up DC–DC converters: A comprehensive review of voltage-boosting techniques, topologies, and applications,” IEEE Trans. Power Electron., vol. 32, no. 12, pp. 9143–9178, Dec. 2017, doi: 10.1109/TPEL.2017.2652318.

[11] H. Wu, K. Sun, L. Chen, L. Zhu, and Y. Xing, “High step-up/step-down soft-switching bidirectional DC–DC converter with coupled-inductor and voltage matching control for energy storage systems,” IEEE Trans. Ind. Electron., vol. 63, no. 5, pp. 2892–2903, May 2016, doi: 10.1109/TIE.2016.2517063.

[12] K. Filsoof and P. W. Lehn, “A bidirectional modular multilevel DC–DC converter of triangular structure,” IEEE Trans. Power Electron., vol. 30, no. 1, pp. 54–64, Jan. 2015, doi: 10.1109/TPEL.2014.2307004.

[13] C. Pineda, J. Pereda, F. Rojas, C. Cerda, X. Zhang, and A. J. Watson, “Asymmetrical triangular current mode (ATCM) for bidirectional high step ratio modular multilevel DC–DC converter,” IEEE Trans. Power Electron., vol. 35, no. 7, pp. 6906–6915, Jul. 2020, doi: 10.1109/TPEL.2019.2957951.

[14] C. Pineda, J. Pereda, F. Rojas, G. Droguett, C. Burgos-Mellado, and A. J. Watson, “Optimal ZCS modulation for bidirectional high-step-ratio modular multilevel DC–DC converter,” IEEE Trans. Power Electron., vol. 36, no. 11, pp. 12540–12550, Nov. 2021, doi: 10.1109/TPEL.2021.3078235.

[15] S. T. S. Lee, S. Y. R. Hui, W. C. Chow, and H. S. H. Chung, “Development of a switched-capacitor DC–DC converter with bidirectional power flow,” IEEE Trans. Circuits Syst. I Fundam. Theory Appl., vol. 47, no. 9, pp. 1383–1389, Sep. 2000, doi: 10.1109/81.883334.

[16] H. Shayeghi, S. Pourjafar, and S. M. Hashemzadeh, “A switching capacitor based multi-port bidirectional DC–DC converter,” IET Power Electron., vol. 14, no. 9, pp. 1622–1636, Sep. 2021, doi: 10.1049/pel2.12137.

[17] R. Hu, J. Zeng, J. Liu, and K. W. E. Cheng, “A nonisolated bidirectional DC–DC converter with high voltage conversion ratio based on coupled inductor and switched capacitor,” IEEE Trans. Ind. Electron., vol. 68, no. 2, pp. 1155–1165, Feb. 2021, doi: 10.1109/TIE.2020.2967667.

[18] S. A. Gorji, H. G. Sahebi, M. Ektesabi, and A. B. Rad, “Topologies and control schemes of bidirectional DC–DC power converters: An overview,” IEEE Access, vol. 7, pp. 117997–118019, Aug. 2019, doi: 10.1109/ACCESS.2019.2937239.

[19] H. Ardi, A. Ajami, F. Kardan, and S. N. Avilagh, "Analysis and implementation of a nonisolated bidirectional DC–DC converter with high voltage gain," IEEE Trans. Ind. Electron., vol. 63, no. 8, pp. 4878–4888, Aug. 2016, doi: 10.1109/TIE.2016.2552139.

[20] H. S. Lee and J. J. Yun, "High-efficiency bidirectional buck–boost converter for photovoltaic and energy storage systems in a smart grid," IEEE Trans. Power Electron., vol. 34, no. 5, pp. 4316–4328, May 2019, doi: 10.1109/TPEL.2018.2860059.

[21] N. A. Dung, H.-J. Chiu, Y.-C. Liu, and P. J. Huang, "Analysis and implementation of a high voltage gain 1 MHz bidirectional DC–DC converter," IEEE Trans. Ind. Electron., vol. 67, no. 2, pp. 1415–1424, Feb. 2020, doi: 10.1109/TIE.2019.2905810.

[22] V. V. S. K. Bhajana, P. Drabek, M. Jara, M. Popuri, A. Iqbal, and C. B. B., "Investigation of a bidirectional DC–DC converter with zero-voltage switching operation for battery interfaces," IET Power Electron., vol. 14, no. 3, pp. 614–625, Mar. 2021, doi: 10.1049/pel2.12048.

[23] H. Liu, L. Wang, Y. Ji, and F. Li, "A novel reversal coupled inductor high-conversion-ratio bidirectional DC–DC converter," IEEE Trans. Power Electron., vol. 33, no. 6, pp. 4968–4979, Jun. 2018, doi: 10.1109/TPEL.2017.2725358.

[24] H. Bahrami, S. Farhangi, H. Iman-Eini, and E. Adib, "Analysis, design, and implementation of DC–DC IBBC–DAHB converter with voltage matching to improve efficiency," IEEE Trans. Ind. Electron., vol. 66, no. 7, pp. 5209–5219, Jul. 2019, doi: 10.1109/TIE.2018.2868260.

[25] Z. Hosseinzadeh, N. Molavi, and H. Farzanehfard, "Soft-switching high step-up/down bidirectional DC–DC converter," IEEE Trans. Ind. Electron., vol. 66, no. 6, pp. 4379–4386, Jun. 2019, doi: 10.1109/TIE.2018.2863216.

[26] M. R. Mohammadi, A. Amoorezaei, S. A. Khajehoddin, and K. Moez, "A high step-up/step-down LVS-parallel HVS-series ZVS bidirectional converter with coupled inductors," IEEE Trans. Power Electron., vol. 37, no. 2, pp. 1945–1961, Feb. 2022, doi: 10.1109/TPEL.2021.3106668.

[27] R. Hu, H. Qi, Z. Yan, W. Wu, J. Zeng, and J. Liu, "A coupled-inductor-based bidirectional DC–DC converter with high voltage conversion ratio and sensorless current balance," IEEE Trans. Ind. Electron., vol. 70, no. 3, pp. 2450–2460, Mar. 2023, doi: 10.1109/TIE.2022.3172770.

[28] M. Madadi, M. Jazaeri, and H. Molla-Ahmadian, "Design and implementation of an ultra-high gain, soft-switching, bidirectional DC–DC converter with high efficiency," e-Prime – Adv. Electr. Eng., Electron. Energy, vol. 12, pp. 101002, Jun. 2025, doi: 10.1016/j.prime.2025.101002.

[29] E. Babaei, Z. Saadatizadeh, and C. Cecati, "High step-up high step-down bidirectional DC–DC converter," IET Power Electron., vol. 10, no. 12, pp. 1556–1571, Dec. 2017, doi: 10.1049/iet-pel.2016.0977.

[30] M. Babaei and M. Monfared, "High step-down bridgeless SEPIC/Cuk PFC rectifiers with improved efficiency and reduced current stress," IEEE Trans. Ind. Electron., vol. 69, no. 10, pp. 9984–9991, Oct. 2022, doi: 10.1109/TIE.2022.3159954.

[31] D. Graovac and M. Pürschel, "MOSFET power losses calculation using the data-sheet parameters," Infineon Technologies AG, Munich, Germany, Appl. Note AN-201, Jan. 2006.

[32] A. H. Masoumi, S. Sharifi, M. Monfared, and S. Karbasforooshan, "Γ-source magnetic integrated filter for single-phase grid tied voltage source converters," IEEE Trans. Ind. Electron., early access, 2019, doi: 10.1109/TIE.2019.2934031.

[33] R. W. Erickson and D. Maksimović, Fundamentals of Power Electronics, 3rd ed. Cham, Switzerland: Springer, 2020, doi: 10.1007/978-3-030-43881-4.

BIOGRAPHIES

Mahdi Madadi received the B.Sc. degree in electronic engineering from Shahid Rajaee University, Tehran, Iran, in 2005, and M.Sc. degree in electrical engineering from the Islamic Azad University, Science and Research Branch, Tehran, Iran, in 2014. He is currently a PhD student in the department of electrical engineering at Semnan University. His research interests include the design and modeling of power converters and renewable energy systems.

Mostafa Jazaeri received the B.Sc. degree from Sharif University of Tech., Tehran, Iran in 1986, the M.Sc. degree from Ferdowsi University of Mashhad, Mashhad, Iran in 1992 and the Ph.D. degree from University of Bath, Bath, UK, in 2003 all in electrical engineering. He is currently an associate Prof. with the department of electrical and computer engineering, Semnan University. His main research interests include power system dynamics and control, AC/DC systems, FACTS.

Hamed Molla-Ahmadian received the B.S. degree in electrical engineering from the Ferdowsi University, Mashhad, Iran, in 2004, the M.Sc. degree in electrical engineering from the Sharif University of Technology, Tehran, Iran, in 2007, and the Ph.D. degree in electrical engineering from Ferdowsi University, Mashhad in 2012. In 2007, he joined Khorasan Institute of Higher Education, Mashhad, Iran, where he is currently an Assistant Professor. Since 2008, he has been the Entrepreneur and the Chairman of Tajhizat Abzarazma Co, Mashhad, Iran. His research interests include the hybrid and switched systems, modeling and control of power electronic converters, and electronic measurement.

Semnan University

Journal of Modeling & Simulation in Electrical & Electronics Engineering (MSEEE)

Journal homepage: **https://mseee.semnan.ac.ir/**

ISSN: 2821-0786

A Novel Method for Inverter Fault Localization in CSC-HVDC System Using DC Current Component

Fatemeh Fallahi Meybodi[1], Ahmad Mirzaei[2*] and Hamidreza Toodeji[3]

Abstract **-- Internal faults within the current source converter–based high-voltage direct current (CSC-HVDC) systems pose serious threats to system reliability and operational security. While integrated protection and control schemes can effectively clear most temporary faults, permanent faults or failures in the control system require accurate localization to enable targeted isolation procedures. Moreover, recurrent transient faults demand timely diagnostic interventions to prevent equipment degradation. This paper focuses on short circuit faults that occur within the inverter stage of CSC-HVDC systems. Considering the converter control dynamics, arm currents are monitored under both forced-alpha operation and normal operating conditions. A novel diagnostic approach is proposed, in which the DC current component is exploited as a distinctive signature to achieve precise arm-level fault localization. The method is computationally simple, does not require high sampling rates, and identifies the fault location within a maximum of two cycles, allowing for isolation before forced-alpha mode is activated. The proposed technique is validated through detailed simulations of the Hydro-Quebec monopolar CSC-HVDC test system in MATLAB/Simulink, demonstrating its effectiveness and rapid response under various fault scenarios.**

Index Terms**: Current Source Converter, High Voltage Direct Current System, Inverter Fault, 12-pulses Converter.**

I. INTRODUCTION

TODAY, high voltage direct current (HVDC) systems are increasingly favored for power transmission, offering three key advantages over high voltage alternating current (HVAC) systems: (1) more economical long-distance power transfer, (2) enhanced controllability and stability, and (3) asynchronous network interconnection capability [1]. Due to the massive amount of energy transmitted by the HVDC system, the reliability and security of this system have a direct impact on the security and stability of the entire system [2]. Consequently, HVDC protection systems have become a critical area of research focus in power systems.

HVDC systems experience multiple fault types, including alternating current (AC) system faults, converter internal faults, and direct current (DC) system faults. The main reason for these faults is insulation failure due to short circuit, lightning, or switching [3]. Extensive research has been conducted on internal faults in converters, with the most prevalent protection schemes being differential protection, overcurrent protection, and direct digital protection [4]-[6]. Due to the high cost and complexity of control associated with direct digital protection, converter switch protection primarily relies on differential and overcurrent relays [7].

A significant challenge during asymmetrical faults in thyristor legs is the generation of inrush current in the converter transformer. This phenomenon can lead to maloperation or even system failure, as conventional differential protection often responds too slowly. To mitigate this risk, faster alternative protection methods must be implemented [8]. The DC blocking method is a protection scheme used to detect and isolate internal short circuit faults

Received; 2025-10-31 Revised; 2025-11-17 Accepted; 2026-01-07

1. Department of Electrical Engineering, Yazd University, Yazd, Iran.
2. Department of Electrical Engineering, Yazd University, Yazd, Iran.
3. Department of Electrical Engineering, Yazd University, Yazd, Iran.
*Corresponding author: mirzaei@yazd.ac.ir

Cite this article as:
Fallahi Meybodi, F., Mirzaei, A., & Toodeji, H. (2026). A Novel Method for Inverter Fault Localization in CSC-HVDC System Using DC Current Component. *Journal of Modeling & Simulation in Electrical & Electronics Engineering (MSEEE)*. Semnan University Press . 6 (1), 33-42.
DOI: https://doi.org/10.22075/MSEEE.2026.39553.1236

in converters, effectively containing fault propagation to adjacent AC/DC subsystems while maintaining grid stability. This approach provides faster fault clearance than conventional differential protection, typically isolating the affected converter within 2-5 ms to prevent cascade failures in the interconnected power system [9]. Modern protection schemes should implement a multi-level blocking strategy to maintain system availability during fault isolation [10].

Another approach for fault location detection in converters involves analyzing the circuit state characteristics and measuring the time differences between signals at different converter terminals. This method enables precise determination of both the fault location and fault type [11]. This technique is commonly employed in modular multilevel converter (MMC) systems, where it facilitates real-time monitoring of individual submodule voltages to enable precise fault detection and localization. Additionally, fault zone identification can be achieved by monitoring transient phenomena and analyzing voltage waveform characteristics across predefined converter sections, enabling precise localization of the faulted area [12], [13]. This method requires a high sampling rate (>1000 kHz) and employs wavelet transform techniques, making it effective in MMC-based HVDC systems.

Given the advancements in signal processing techniques in recent years, a method for detecting faults within the converter can be proposed using either the wavelet transform or the Stockwell transform [14], [15]. In the wavelet transform method, selecting the appropriate mother wavelet is crucial for both the accuracy and speed of fault detection. Additionally, this method is susceptible to noise, and the presence of electromagnetic interference in the current source converter (CSC) can distort the wavelet coefficients. On the other hand, the Stockwell transform method, which combines wavelet and Fourier transforms for fault detection, comes with a high computational cost. Moreover, interpreting its results typically requires advanced classification algorithms.

Additionally, these two methods may fail to accurately distinguish between internal converter faults and DC-side faults, load variations, or AC grid disturbances.

Modern HVDC protection systems are increasingly employing intelligent techniques such as artificial neural networks (ANNs) and support vector machines (SVMs) for fault detection, thereby enhancing the reliability and performance of conventional protection schemes. [16], [17]. Neural networks, being more straightforward to implement, are primarily employed for preliminary detection of basic faults and demonstrate moderate accuracy in complex fault scenarios. The SVM approach shows strong performance with limited datasets but faces challenges when handling large-scale data, and is predominantly utilized for fault classification. A key limitation of these intelligent methods is their substantial requirement for training data. This poses practical challenges for HVDC systems, as acquiring real-world internal converter fault data is both technically difficult and economically costly.

The unique configuration of controlled thyristor arms in CSCs and the specific control characteristics of CSC-HVDC systems enable partial implementation of both DC protection and inverter protection during commutation faults. Numerous studies have demonstrated that these protection systems can achieve satisfactory performance when coordinated adequately with the converter's control strategy. In the event of a permanent fault or failure of the control system, we require an effective protection structure to identify the most detailed part of the fault as possible and to minimize stress on the equipment and system through appropriate protective operations, such as repair or replacement of the faulty part.

In this paper, the effect of control parameters in various fault conditions within the inverter is investigated, and a protection structure is presented that can determine the fault arm in the event of control system failure or the presence of a permanent fault. This method utilizes a comparison of DC versus arm current to detect the faulty arm prior to forced alpha function activation, enabling preemptive isolation of the faulted section and maintaining uninterrupted system operation. The main contributions of this paper are summarized as follows:

- A novel DC-current-signature-based algorithm for arm-level fault localization in CSC inverters.
- Demonstration of fault identification within two cycles using low-rate sampling and a simple decision rule.
- Validation on the Hydro-Quebec monopolar CSC-HVDC test system simulated in MATLAB/Simulink across a range of permanent and transient fault scenarios, including cases with control-system failures and commutation disturbances.

The different sections of the article are as follows:

In Section 2, the structure of the system under study is examined. In Section 3, the control characteristic diagram and the control modes of the system are described. In Section 4, various permanent and transient faults on the thyristor arms of the inverter are simulated, and the performance of the control system for fault suppression is examined. In Section 5, a protection method is presented that can detect the location of the fault inside the converter, based on the presence of the DC component in the thyristor arms.

II. The Studied Network

The system analyzed in this paper is derived from Hydro-Quebec monopolar HVDC link. It transmits 1000 MW at ±500 kV DC and 2 kA via a 300 km DC line, interconnecting a 5000 MW, 500 kV, 60 Hz AC grid (rectifier) with a 10,000 MW, 345 kV, 50 Hz AC grid (inverter). Both rectifier and inverter utilize twelve-pulse thyristor-based CSCs, which significantly reduce harmonic distortion in both DC voltage and current, as well as in AC waveforms, compared to six-pulse converters. According to Fig. 1, the converters are connected to the AC system through a three-winding Y/Y/Δ transformer and to the DC system through a 0.5 H smoothing inductor. The AC filters installed on the AC side of both converters prevent the odd harmonics of the current from entering the AC system and act as a large capacitor at the fundamental frequency, compensating for the reactive power consumed by the rectifier due to the firing angle α. The DC filters also prevent the voltage harmonics from entering the DC system.

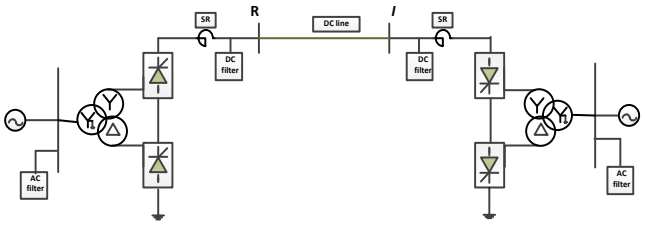

Fig. 1. Monopolar HVDC network with CSC.

Fig. 2 illustrates the internal structure of a twelve-pulse CSC. Each twelve-pulse converter comprises two six-pulse converters supplied via a three-winding transformer with star and delta connections. The converter connected to the star connection of the transformer is referred to as a star converter. In contrast, the converter connected to the delta connection of the transformer is referred to as a delta converter.

According to Fig. 2, each converter contains two upper and lower legs, with each leg comprising three arms. Within every arm, thousands of thyristors are connected in series. This article aims to investigate and precisely locate faults occurring within individual arms of this configuration.

Throughout this article, the following nomenclature applies with reference to Fig. 2: S denotes the star converter, D denotes the delta converter, U and L represent the upper and lower legs, respectively, and numerals 1 through 3 identify the arm positions. For example, SU1 indicates the first arm at the upper leg of the star converter. Since the current source is supplied from the DC line side, current measurements are positioned at the upper terminal of each arm, denoted as 'M' in Fig. 2. In this article, we investigate internal faults within the converter arms—exemplified by the SU1 fault location marked 'F' in Fig. 2—and develop an algorithm to identify such fault positions precisely.

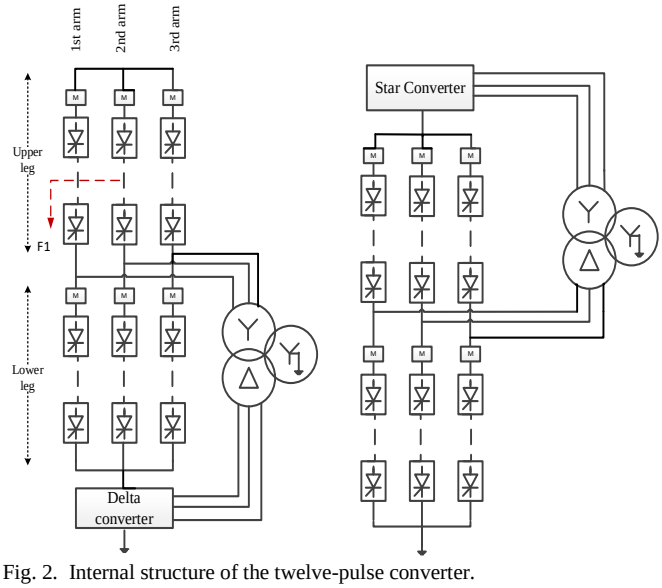

Fig. 2. Internal structure of the twelve-pulse converter.

In this study, the diagnostic algorithm uses the individual arm currents measured at the upper terminals of the thyristor arms, denoted by the "M" points in Fig. 2. These measurement points are located on the DC-fed side of each arm, between the smoothing reactor / DC bus and the corresponding thyristor stack. Therefore, the currents are acquired directly in the DC arm branches. In practice, non-intrusive Hall-effect or optical current transducers can be installed on each monitored arm. Because the proposed method relies on the cycle-averaged (DC) component of these currents, a modest sensor bandwidth of about 2–5 kHz is sufficient, and no high-frequency transient information is required.

III. The Control System

Fig. 3 depicts the equivalent circuit of the studied HVDC system, where the DC network is represented by a fundamental inductance L and a series resistance R. The values of L and R represent the inductance and resistance of the smoothing inductor and DC line, respectively. The voltages V_{dr} (rectifier voltage across the terminals) and V_{di} (inverter voltage across the terminals) are defined according to (1) and (2).

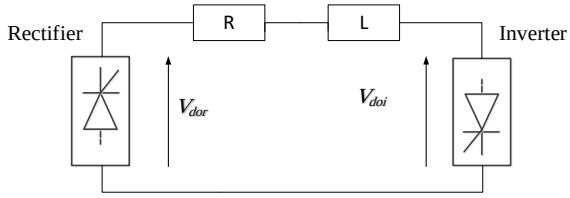

Fig. 3. Equivalent circuit of HVDC system.

$$V_{dr} = V_{dor}\cos\alpha - R_{cr} I_d \quad (1)$$

$$V_{di} = V_{doi}\cos\gamma - R_{ci} I_d \quad (2)$$

Where V_{dor} is the rectified voltage dependent on the AC voltage of the rectifier side, and V_{doi} is the inverter voltage dependent on the AC voltage of the inverter side. I_d is the DC line current, and α is the firing angle. If μ is the commutation angle, the extinction angle is defined as $\gamma=\pi-\alpha-\mu$.

According to the equivalent circuit and considering (1) and (2), the DC current can be written as (3) and (4).

$$I_d = (V_{dr} - V_{di})/R \quad (3)$$

$$I_d = (V_{dor}\cos\alpha - V_{doi}\cos\gamma)/(R + R_{cr} - R_{ci}) \quad (4)$$

According to (3), the DC current magnitude is directly proportional to the voltage differential measured between the rectifier and inverter terminals. Furthermore, the control factors I_d include the firing angle α, the extinction angle γ, and the AC voltages of the rectifier and inverter sides.

In most HVDC systems operating optimally, the rectifier controls DC current while the inverter regulates the DC voltage. Fig. 4 illustrates the corresponding V-I control characteristic and identifies the system operating point (Q) in this mode. According to (4), and considering that the firing angle α is maintained in the range of 2 to 5 degrees to ensure sufficient thyristor turn-on voltage. The constant alpha characteristic is plotted in the diagram of Fig. 4.

The constant alpha characteristic (line AB in Fig. 4) applies when the AC voltage on the rectifier side suddenly decreases, and according to (1), the system compensates for this by decreasing α. As a result, the system enters the constant alpha state and maintains a constant value of α at 2 degrees. According to the diagram in Fig. 5-a, in this case, the rectifier and inverter diagrams may not have an intersection point. As a result, the inverter enters the constant current state, and the operating point is located at (S). Since the value of the inverter current is usually less than the rectifier current, the marginal value of the current is considered to be 0.1, as indicated by ΔI_d in Fig. 4.

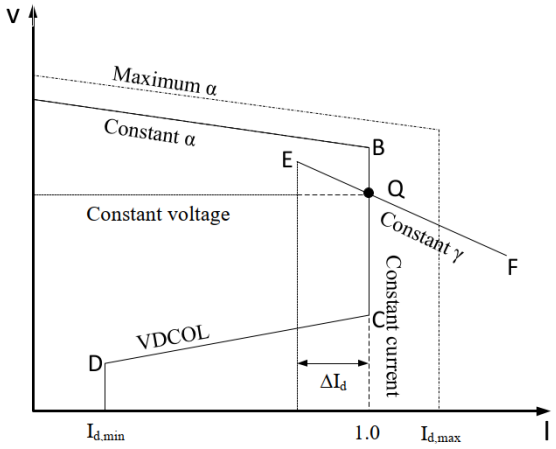

Fig. 4. Current-voltage characteristic of DC system.

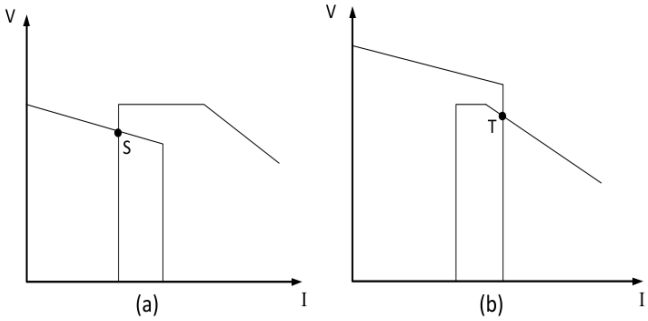

Fig. 5. Current-voltage characteristic of DC system during AC voltage drop on the a) rectifier side, b) inverter side.

On the other hand, by reducing the AC voltage on the inverter side, to prevent the occurrence of commutation failure, the inverter enters the constant gamma mode (line EF in Fig. 4). It keeps the value of γ constant at its minimum allowable value. The operating point of the system in this mode is indicated by (T) in Fig. 5-b [18], [19].

To protect thyristors from overheating at high currents, the maximum DC current ($I_{d,max}$) must be kept below 1.2 per unit. Similarly, to maintain continuous current flow and prevent dangerous chopping, the minimum current ($I_{d,min}$) must stay above 0.2 per unit. These operating limits are shown in Fig. 4.

The voltage-dependent current order limiting (VDCOL) characteristic, represented by line CD in Fig. 4, proportionally reduces the reference current during DC voltage depressions caused by DC faults or severe AC faults. This reduction subsequently decreases AC system reactive power consumption, facilitating faster grid recovery during fault conditions.

In the inverter, the values of α_{min} and α_{max} are defined to ensure that the inverter does not enter the rectifier mode and to create the necessary margin for the minimum extinction angle, respectively. Moreover, following DC faults, the absence of current zero crossing prevents arc extinction. Consequently, fault-induced arcs persist even after fault clearance. To deal with this situation, after 0.07 seconds a forced alpha mode is activated in which the rectifier enters the forced alpha mode and its alpha value is kept constant at 166 degrees, as a result of which the rectifier operates in the inverting mode and the system energy is discharged from the two rectifier and inverter terminals and the electric arc caused by the fault is extinguished [18].

IV. Proposed Method

Faults within the converter can be caused by factors such as thyristor arm malfunction, failure of associated components, inverter commutation failure, or an internal converter short circuit. This paper aims to investigate the short-circuit fault in thyristor arms within the inverter.

In reference [20], a short circuit fault in the thyristor arms of the rectifier is investigated. Since this fault current contains a DC component and exhibits no zero crossing, the resulting electric arc persists after fault clearance. Due to the rectifier's AC network supply, this internal converter fault effectively manifests as a permanent short circuit fault on the AC network side. Consequently, by measuring the transformers' secondary current and detecting both the DC component magnitude and direction, the fault location (specific arm or phase) can be identified. This enables fault elimination through selective single-phase switching on the transformer primary winding. However, this mitigation strategy is ineffective for inverter-side faults. Because the inverter is DC fed, single-phase switching on the inverter side transformer is operationally ineffective.

Although the forced alpha method can discharge system energy and restore operation during transient faults, locating the fault becomes critical for inspection and maintenance when encountering permanent faults, repeated faults, or control system malfunctions.

Since the fault is DC network fed, during a leg fault, the current in the lower thyristor legs collapses to zero, and the DC current component diverts exclusively through the upper bus to the faulted leg. According to Fig. 2, an SL1 fault causes current collapse in all delta-connected (D) arms while the DC current component persists exclusively within the star-converter legs. Furthermore, because the delta converter's lower phase leg is grounded, a short circuit fault here only reduces current magnitude without typical short circuit effects.

V. Simulation Results

This paper proposes a fault detection method based on measuring arm currents within the converters and analyzing their DC components. The approach enables precise fault location identification, allowing targeted inspection or preventive measures to be implemented on the affected converter arm.

The network analyzed in this study is derived from Hydro-Quebec monopolar HVDC system. This system demonstrates robust fault management capabilities, effectively detecting both DC and AC faults while maintaining optimal control during fault conditions. However, the system cannot detect internal converter faults.

This section simulates multiple short-time faults (0.7–0.78 s) across different inverter arms and discusses the results. First, system behavior is evaluated without forced alpha operation.

Figs. 6 and 7 depict SU2 and SL2 currents on the inverter side during a short circuit fault in SU2.

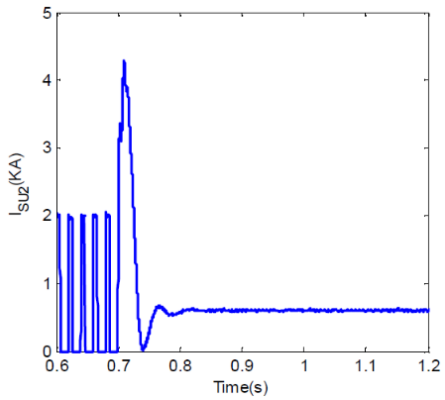

Fig. 6. SU2 current during short circuit fault in SU2.

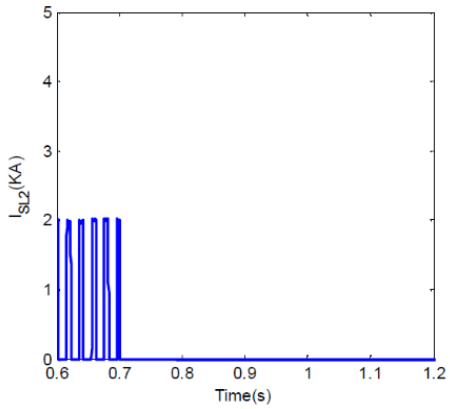

Fig. 7. SL2 current during short circuit fault in SU2.

Figs. 8 and 9 also depict the change in the converter control mode and the inverter reference current when this fault occurs. The control modes include 0 for block mode, 1 for constant current, 2 for constant voltage, 3 for minimum alpha, 4 for maximum alpha, 5 for forced alpha, and 6 for gamma control.

Since the fault is fed from the DC line side, when a short circuit fault occurs in SU, the current in SL, DU, and DL becomes zero. During DC faults, the control system reduces the reference current according to the VDCOL characteristic in response to a reduction in DC voltage. This action forces the inverter into current control mode, thereby reducing the magnitude of fault current. Due to the DC current component and the absence of zero crossing, the fault-induced electric arc persists. After fault clearance, this current continues to circulate within the faulted section. As the inverter voltage drops to zero, it loses control of the system voltage and current, and the inverter enters the maximum alpha state.

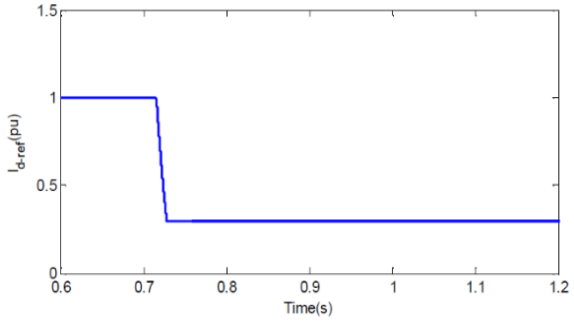

Fig. 8. Control modes changes in the inverter during a short-circuit fault in SU2.

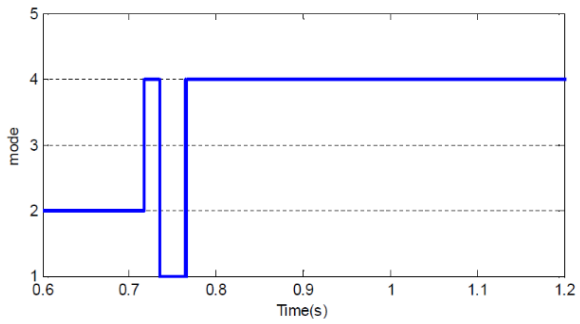

Fig. 9. Reference current changes in the inverter during a short-circuit fault in SU2

Figs. 10 to 12 depict SU1, SL1, and DU1 currents on the inverter side during an SL1 short circuit fault. Figs. 13 and 14 show the corresponding converter control mode variations and inverter reference current dynamics under this fault condition. As with prior fault, DC voltage reduction during this fault activates the VDCOL function. The resultant reference current decreases the DC current, causing the inverter to enter current control mode.

However, in this scenario, the current reduction extinguishes both the electric arc and the fault current. Consequently, the inverter maintains current control mode, restoring the network to its pre-fault state by ramping up the reference current. As illustrated in Fig. 2, the fault current path flows through SU. During such faults, SU manifests overcurrent while DC current appears in both star converter legs; meanwhile, delta-converter currents collapse completely to zero.

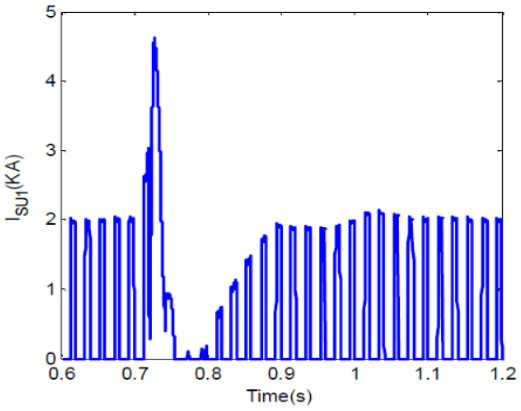

Fig. 10. SU1 current during short circuit fault in SL1.

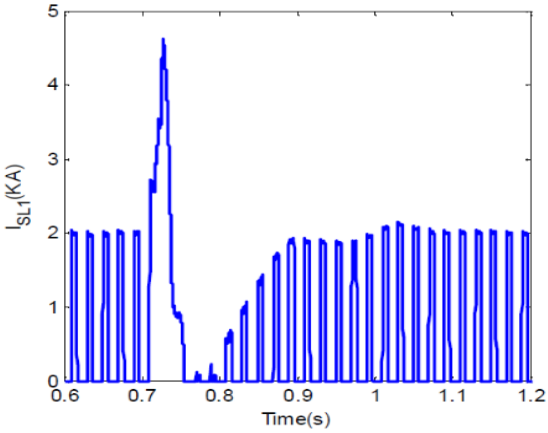

Fig. 11. SL1 current during short circuit fault in SL1.

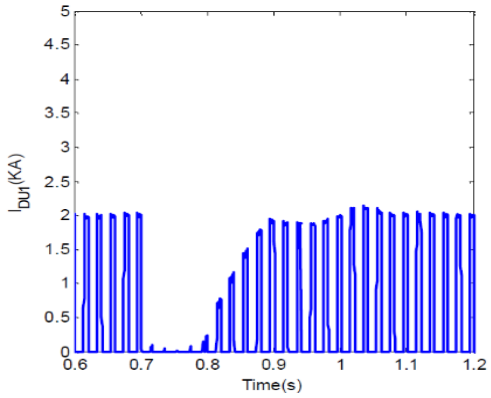

Fig. 12. DU1 current during short circuit fault in SL1.

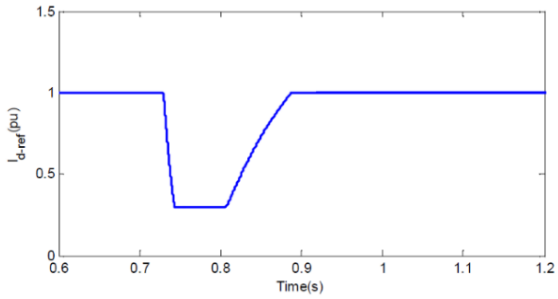

Fig. 13. Control modes changes in the inverter during a short-circuit fault in SL1.

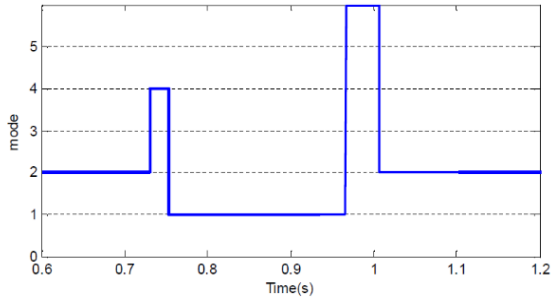

Fig. 14. Reference current changes in the inverter during a short-circuit fault in SL1.

Figs. 15 to 17 depict SU1, SL1, and DU2 currents on the inverter side during a DU2 short circuit fault. Figs. 18 and 19 show converter control mode variations and inverter reference current dynamics under this condition. As fault current rises and DC voltage drops—consistent with prior cases—VDCOL reduces the reference current, triggering the converter's transition to current control mode. Fig. 2 confirms that at fault initiation, both star converter legs and the faulted arm simultaneously manifest overcurrent accompanied by DC component generation. However, similar to SL fault cases, the star converter's fault current ceases completely, allowing uninterrupted continuation of normal operation.

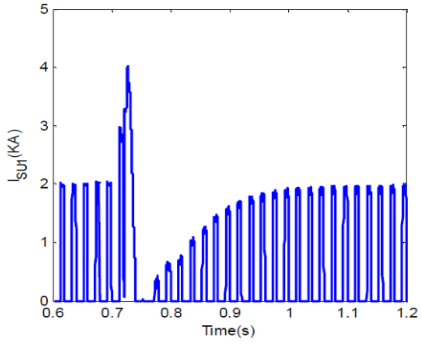

Fig. 15. SU1 current during short circuit fault in DU2.

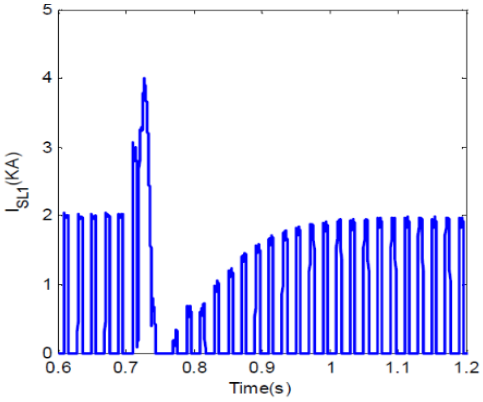

Fig. 16. SL1 current during short circuit fault in DU2

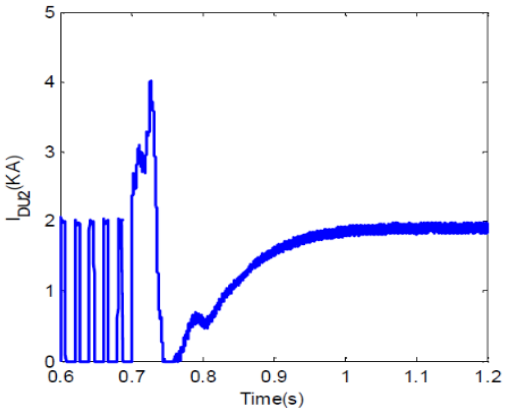

Fig. 17. DU2 current during short circuit fault in DU2.

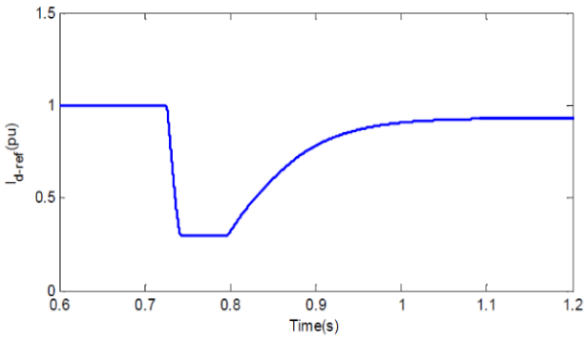

Fig. 18. Control modes changes in the inverter during a short-circuit fault in DU2.

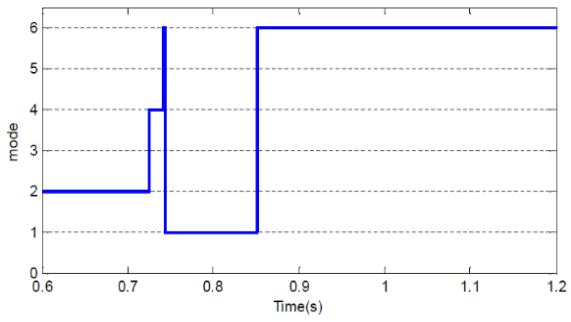

Fig. 19. Reference current changes in the inverter during a short-circuit fault in DU2.

In fact, the inverter maintains current control mode, increasing the reference current to 1.0 pu after the star converter fault clearance. However, the electric arc persists in the delta converter, sustaining localized current circulation at the fault point. Consequently, the inverter's operation resembles a 6-pulse converter. Due to the primary current path configuration, current cannot reach the delta converter's lower phase leg. Until fault extinction, this leg's current

persists at zero, prompting the system to engage gamma control mode to prevent commutation failure.

Since the delta converter's lower phase leg is grounded, short-circuit faults in this leg become electrically insignificant and need not be investigated.

Simulations in this section omitted forced alpha mode operation. Consequently, the presence of DC components in arm currents and current collapse in non-faulted arms enables unambiguous identification of the faulty leg and arm.

When forced alpha operation is active:

- For SU/DU faults: VDCOL reduces the reference current to lower the fault current, triggering forced alpha activation. Increasing α to 166° discharges system energy bidirectionally, extinguishing the transient fault arc.
- For SL faults: The fault arc self-extinguishes without requiring forced alpha intervention.

However, for permanent faults, recurring faults, or control system failures, a fault location algorithm becomes essential. This enables targeted inspection, repair, or preventive measures.

Figs. 20 to 22 present simulation results for short circuit faults across various converter legs under forced alpha operation.

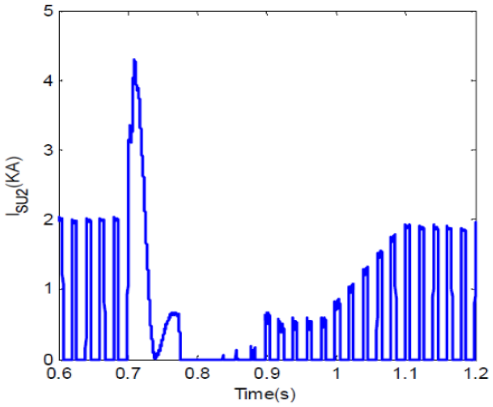

Fig. 20. SU2 current during short circuit fault in SU2 with forced alpha mode activated.

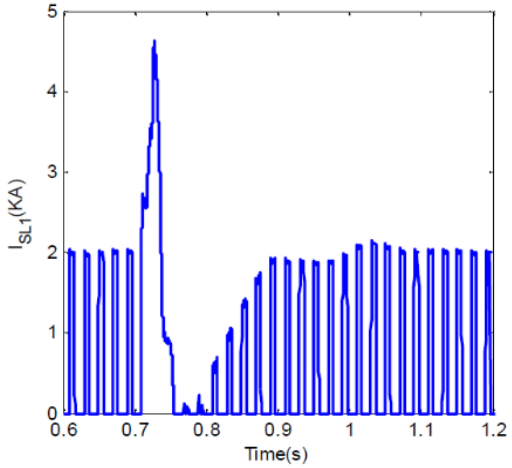

Fig. 21. SL1 current during short circuit fault in SL1 with forced alpha mode activated.

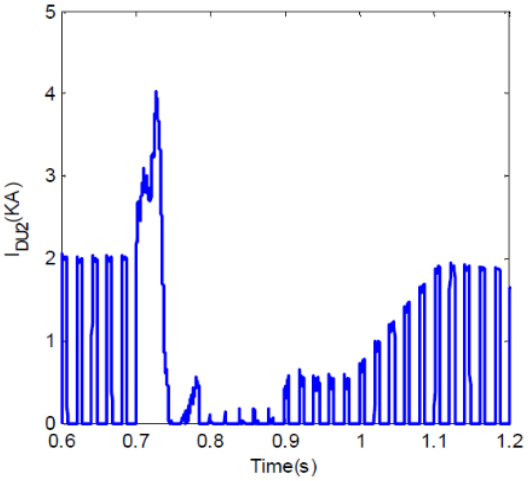

Fig. 22. DU2 current during short circuit fault in DU2 with forced alpha mode activated.

As demonstrated in the figures, forced alpha activation extinguishes the fault. Crucially, identification of the faulty arm must precede this activation. In all cases, one or two upper leg arms exhibit DC component currents, with current collapse occurring in the lower legs of the affected converter section. Given that forced alpha mode activates 70 ms post-fault inception, a dedicated algorithm must detect and locate faults before forced alpha initiation.

VI. Protection Method Algorithm

During normal operation, each converter arm conducts current for 60 electrical degrees (one-third of a cycle) and remains at zero current for 120 electrical degrees (two-thirds of a cycle). However, during an arm short circuit fault, lower leg arm currents collapse to zero while the faulted arm conducts continuously for multiple cycles. This distinct behavior forms the foundation of the fault detection algorithm.

A fault in a given arm is confirmed if its current remains non-zero for 40 ms (two cycles) while all lower leg arms maintain zero current throughout this interval. Figs. 23 and 24 show the proposed algorithm. According to Figs. 23 and 24, Algorithm A initially executes across all four inverter-side converter legs, numbered 1 to 4 sequentially from top to bottom. In the Algorithm of Fig. 23, the arm current integral (C_j) and DC line current integral (d) are measured over one cycle. If these two parameters are equal, the arm is short-circuited to the DC line current. To ensure valid fault determination, the Algorithm of Fig. 23 requires that the value of $|C_j\text{-}d|$ be less than a threshold value (Δ_{th}) for two consecutive cycles.

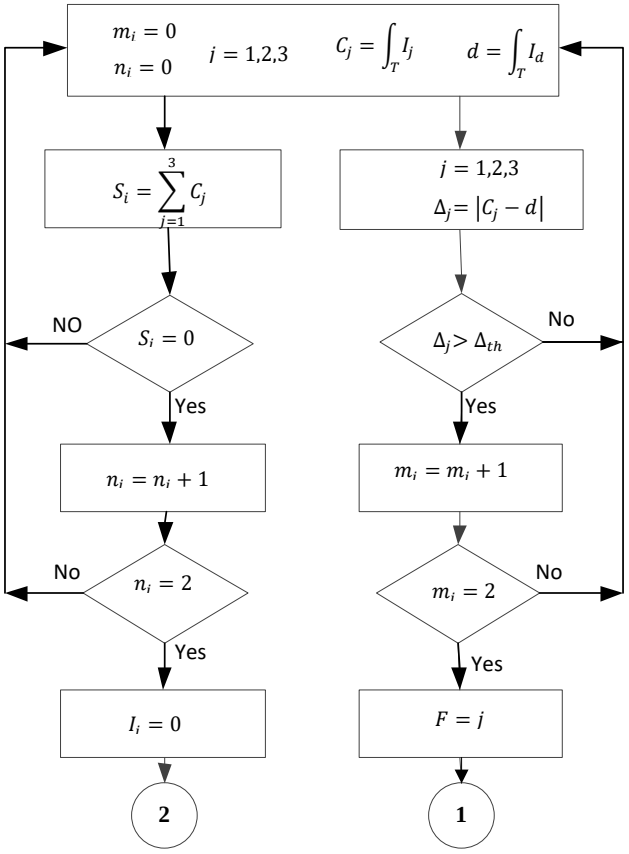

Fig. 23. Algorithm for measuring the average current in the inverter arms (algorithm A)

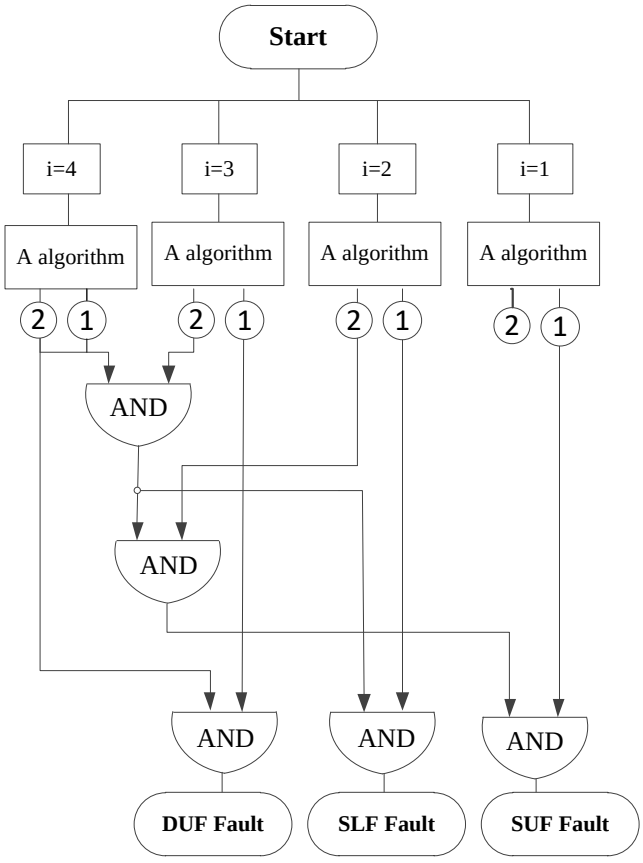

Fig. 24. Proposed fault detection for inverter arms

Since the fault feed path originates from the DC line, the current in the upper legs that are short-circuited can also apply to this condition. Therefore, the condition of zero current in the lower legs must also be checked.

In Algorithm of Fig. 23, the sum of the integral currents of all three arms in one leg (S_i) is also calculated, and if this value is zero during two cycles, it means that no current is entered this leg, which could be due to a short circuit in the upper legs. Finally, in the algorithm of Fig. 23:

- Output 1 activates if any arm current equals the DC line current for 40 ms.
- Output 2 activates if the leg current sum *Si*=0 persists for two consecutive cycles.

In the Fig. 24 algorithm, Outputs 1 and 2 from Fig. 23 serve as inputs. When active, they trigger validation of two concurrent conditions:

- Arm current continuity ($|Cj-d|<\Delta th$)
- Zero current in all lower arms

Both conditions must persist for 40 ms to confirm fault localization. When an arm's current equals the DC line current concurrent with zero current in all lower legs, this confirms a short-circuit fault in that specific arm. The faulted arm and its parent leg are thereby definitively localized.

Since the proposed method detects the fault through the cycle-averaged (DC) component of the arm currents, it is inherently less sensitive to sensor inaccuracies than high-frequency or transient-based protection schemes. Sensor offset has a negligible impact on the decision logic because the fault indication is obtained by comparing the integral of the arm current with the integral of the DC line current, causing constant offsets to cancel each other out. Long-term drift may shift the threshold Δth slightly, but the fault signature (persistent arm current with simultaneous current collapse in the lower legs) remains unaffected; drift can be mitigated through periodic calibration. Bandwidth requirements are modest, as only the fundamental-frequency waveform needs to be captured; a bandwidth of 2–5 kHz is adequate. Sensor saturation is unlikely because the arm currents remain within the continuous-measurement range of standard Hall-effect or optical transducers commonly used in HVDC converters.

For practical implementation, the algorithm requires only cycle-averaged arm-current values. Therefore, a sampling rate of 20–40 samples per electrical cycle is sufficient, corresponding to approximately 1–2 kHz for 50/60 Hz power systems. No high-frequency transient components are needed, and the method remains fully effective at these modest sampling rates.

The proposed algorithm has a very low computational burden, as it requires only cycle-by-cycle integration of arm currents and simple comparison operations. No frequency-domain processing or high-rate sampling is needed. Therefore, the method can be executed on typical DSP- or FPGA-based HVDC control platforms with negligible CPU load and memory usage (only two cycles of data are stored). The latency of the implementation is well below the two-cycle detection window, making the algorithm suitable for real-time industrial deployment.

In practical HVDC installations, arm-current measurements are affected by EMI and sensor noise. However, the proposed algorithm relies on the cycle-averaged (DC) value of the arm currents, which inherently suppresses high-frequency disturbances and makes the method robust to typical measurement noise. Only severe sensor drift or loss of

measurement may affect detection, while moderate noise does not alter the integral-based decision criteria. If required, a simple moving-average or low-pass filter may be applied to the measured currents; such filtering does not impact the detection time because the algorithm already operates over a 20–40 ms evaluation window. From a computational perspective, the algorithm consists mainly of three numerical integrations and threshold comparisons, resulting in a negligible computational burden. Consequently, it can be executed on standard DSP-based HVDC controllers or small FPGA devices with minimal latency and very low memory usage (only one or two cycles of samples are needed). Thus, the method is fully compatible with practical HVDC protection hardware.

VII. Limitations and Discussion

The proposed detection mechanism is based solely on the DC-fed nature of current-source converter arms and the characteristic collapse of the lower-leg currents during internal arm faults. Therefore, the same principle applies to bipolar HVDC links, where the two poles can be evaluated independently. In multi-terminal CSC-HVDC systems, the arm-level detection principle remains valid; however, coordination with station-level protection may be required due to the more complex current-sharing behavior. The method assumes a conventional thyristor-based CSC structure, and substantially modified converter topologies may require adjustments of the detection thresholds.

The applicability of the proposed method is governed by the characteristic current signatures produced by internal arm faults. Internal faults create a persistent DC component in the faulted upper arm and cause all lower-leg currents in the same converter section to collapse. In contrast, severe DC-line faults depress all arm currents simultaneously without generating a localized DC offset. This inherent difference enables reliable discrimination between the two fault categories. The algorithm is also capable of handling evolving or sequential faults, as the decision logic is based on the cycle-by-cycle evaluation of the arm-current integrals. Simultaneous multi-arm faults can be detected, but may require coordination with station-level protection if their signatures become ambiguous. The method is most effective for low- and medium-impedance internal faults; very high-impedance faults may produce a weak DC component, in which case auxiliary protection functions may be needed.

VIII. Conclusion

This study presents a novel and efficient approach for precise short-circuit fault localization in inverter arms of CSC-HVDC systems. By relying solely on arm current measurements, the proposed method eliminates the need for voltage sensors while maintaining high diagnostic accuracy. The algorithm, based on current integration, deterministically identifies the faulty arm within two electrical cycles (about 40 ms) and operates effectively without high-rate sampling or computationally intensive processing. The method was rigorously validated through comprehensive simulations under both forced-α operation and normal operating conditions. Results demonstrate that it consistently achieves fault localization within 40 ms—fast enough to enable preventive isolation before significant energy discharge occurs. For permanent faults, the capability to pinpoint the exact faulty arm enables targeted maintenance, allowing for the rapid isolation and replacement of damaged components and thereby minimizing system downtime.

In the proposed method, the fault detection time is on the order of two network cycles. Due to its reliance on the DC component of the arm current, a high sampling rate is not required; sampling rates of a few kilohertz are sufficient for effective signal extraction. In contrast, wavelet-based methods typically require much higher sampling rates (tens to hundreds of kHz) and longer processing times due to the multi-stage nature of wavelet analysis. AI-based approaches, especially those using neural networks or deep learning algorithms, have detection times dependent on the model size and complexity, often resulting in higher computational delays and the need for more powerful hardware.

Regarding computational load, the proposed method only requires the calculation of the instantaneous current integral and comparison of DC values. Therefore, it is significantly lighter than wavelet methods, which involve multi-level signal decomposition, and AI-based methods, which require feature extraction, model training, or execution of complex networks. This makes it feasible for implementation on standard HVDC controllers with limited computational resources.

In terms of accuracy, although wavelet and AI methods may achieve high performance under laboratory conditions, their strong dependence on signal quality, parameter tuning, and high sampling rates can reduce their effectiveness in noisy industrial HVDC environments. In contrast, the proposed method, due to the DC nature of the detection index and the high current levels in CSC-HVDC, is less sensitive to noise and has demonstrated stable and fast detection of internal arm faults under simulated conditions.

Therefore, based on this qualitative comparison, the main advantages of the proposed method over wavelet- and AI-based techniques are its simplicity, low sampling rate requirement, minimal computational load, and short detection time. However, precise numerical comparisons can be addressed in future studies.

Acknowledgments

The authors gratefully acknowledge the support for this work that was provided by Yazd University.

Funding Statement

This research received no specific grant from any funding agency in the public, commercial, or not-for-profit sectors.

Conflicts of Interest

The author declares that there is no conflict of interest regarding the publication of this article.

Authors' Contributions

Conceptualization and study design: (F.F.M. & A.M.)
Data collection and experimentation: (F.F.M.)
Data analysis and interpretation: (All)
Manuscript writing and editing: (All)
Supervision and project administration: (A.M.)

STATEMENT ON THE USE OF GENERATIVE AI

AI cannot be listed as an author. Only human authors take responsibility.

REFERENCES

[1] M. Kumari and A. Yadav, "An adaptive neuro fuzzy inference system based method for DC fault recognition in VSC-MTDC system," *Modeling and Simulation in Electrical and Electronics Engineering*, vol. 3, no. 1, pp. 23-36, 2023.

[2] S. p. Gao, Q. Liu, and G. b. Song, "Current differential protection principle of HVDC transmission system," *IET Generation, Transmission & Distribution*, vol. 11, no. 5, pp. 1286-1292, 2017.

[3] M. Muniappan, "A comprehensive review of DC fault protection methods in HVDC transmission systems," *Protection and Control of Modern Power Systems*, vol. 6, no. 1, pp. 1-20, 2021.

[4] H. Darwish, M. Rahman, A. Taalab, and H. Shaaban, "Overcurrent relay with novel characteristics for HVDC converter protection," in *Proceedings 1995 Canadian Conference on Electrical and Computer Engineering*, IEEE, 1995, pp. 664-667.

[5] C. Buccella, C. Cecati, and H. Latafat, "Digital control of power converters—A survey," *IEEE Transactions on Industrial Informatics*, vol. 8, no. 3, pp. 437-447, 2012.

[6] H. Li, Y. Xia, Z. Wang, K. Zhang, P. Li, and Y. Fu, "Analysis and Improvement of Bridge Differential Protection Behavior of Smart Converter Substation," in *2019 4th International Conference on Intelligent Green Building and Smart Grid (IGBSG)*, IEEE, 2019, pp. 185-189.

[7] H. A. Darwish, A. M. Taalab, and M. Rahman, "Performance of HVDC converter protection during internal faults," in *2006 IEEE Power Engineering Society General Meeting*, IEEE, 2006, pp. 1-7.

[8] T. Zheng, X. Liu, and X. Guo, "Analysis of fault-induced inrush current of converter transformer in LCC HVDC system considering DC control and protection," *International Journal of Electrical Power & Energy Systems*, vol. 125, p. 106536, 2021.

[9] Y. Liu, X. Zhu, J. Deng, J. Guo, F. Yu, and J. Li, "Research on protection block strategy of grounding faults in HVDC converter station," *The Journal of Engineering*, vol. 2019, no. 16, pp. 1016-1019, 2019.

[10] S. Yan, Z. He, J. Yang, M. Kong, and M. Hu, "Optimized protection strategies for HVDC grid with fault-blocking modular multilevel converters for overhead line applications," *Journal of Modern Power Systems and Clean Energy*, vol. 8, no. 6, pp. 1168-1177, 2020.

[11] S. Yin and X. Li, "Converter valve-level fault location method based on the temporal differences among horizontal and longitudinal valve states," *International Journal of Electrical Power & Energy Systems*, vol. 154, p. 109458, 2023.

[12] D. Mu, S. Lin, H. Zhang, and T. Zheng, "A novel fault identification method for HVDC converter station Section based on energy relative entropy," *IEEE Transactions on Instrumentation and Measurement*, vol. 71, pp. 1-10, 2022.

[13] S. Lin, D. Mu, L. Liu, Y. Lei, and X. Dong, "A novel fault diagnosis method for DC filter in HVDC systems based on parameter identification," *IEEE Transactions on Instrumentation and Measurement*, vol. 69, no. 9, pp. 5969-5971, 2020.

[14] M. Tahan, H. Monsef, and S. Farhangi, "A new converter fault discrimination method for a 12-pulse high-voltage direct current system based on wavelet transform and Hidden Markov Models," *Simulation*, vol. 88, no. 6, pp. 668-679, 2012.

[15] A. Pragati, D. A. Gadanayak, and M. Mishra, "Fault detection and fault phase identification in a VSC-MT-HVDC link using Stockwell transform and Teager energy operator," *Electric Power Systems Research*, vol. 236, p. 110937, 2024.

[16] A. E. Abu-Elanien, "An artificial neural network-based technique for protection of HVDC grids," in *2019 IEEE PES GTD Grand International Conference and Exposition Asia (GTD Asia)*, 2019: IEEE, pp. 1004-1009.

[17] R. Muzzammel and A. Raza, "A support vector machine learning-based protection technique for MT-HVDC systems," *Energies*, vol. 13, no. 24, p. 6668, 2020.

[18] V. K. Sood, *HVDC and FACTS controllers*. 2004, pp. 68-93.

[19] D. Jovcic, *High Voltage Direct Current Transmission: converters, systems and DC grids*, 2 ed. 2019, pp. 49-56.

[20] F. D. Marvasti and A. Mirzaei, "A novel method of combined DC and harmonic overcurrent protection for rectifier converters of monopolar HVDC systems," *IEEE Transactions on Power Delivery*, vol. 33, no. 2, pp. 892-900, 2017.

Fatemeh Fallahi Meybodi received the B.Sc. degree in electrical engineering from Isfahan University of Technology, Isfahan, Iran, in 2012, and the M.Sc. and Ph.D. degrees in power engineering from Yazd University, Yazd, Iran, in 2014 and 2025, respectively. Her research interests include HVDC systems.

Ahmad Mirzaei received the B.Sc. degree in 1988, M.Sc. degree in 1994, and Ph.D. degree in power engineering from Isfahan University of Technology, Isfahan, Iran, in 2005. He is an associate professor at Yazd University, Yazd, Iran. His research interests include power systems, electrical machines, power quality, and intelligent systems.

Hamidreza Toodeji received the B.Sc. degree in electrical engineering from Isfahan University of Technology, Isfahan, Iran, in 2006, and the M.Sc. and Ph.D. degrees in power engineering from Amirkabir University of Technology, Tehran, Iran, in 2008 and 2015, respectively. He is currently an Assistant Professor at Yazd University, Yazd, Iran. His current research focuses on power electronics and control in HVDC systems, and reliability enhancement of converter-based power networks. His broader interests include power electronics and renewable energy systems.

Semnan University

Journal of Modeling & Simulation in Electrical & Electronics Engineering (MSEEE)

Journal homepage: **https://mseee.semnan.ac.ir/**

ISSN: 2821-0786

Design and Optimization of a Rose-Inspired Plasmonic Filter using Machine Learning

Seyed Mohammad Mehdi Hosseini[1], Pejman Rezaei[2]*and Shiva Khani[3]

***Abstract*- Bio-inspired plasmonic structures offer a powerful route toward compact and high-performance photonic components by ena-bling strong confinement of surface plasmon polaritons (SPPs) at deeply subwavelength scales. In this research, a tunable mul-tichannel bandpass filter using surface plasmon polaritons (SPPs) is introduced and numerically studied on a metal-insulator-metal (MIM) waveguide substrate. Consisting of a central circular resonator, two larger main waveguides, and six smaller sat-ellite resonators, the proposed structure exploits a unique rose-like geometry. High Q-factor (Q-factor) multiple resonance modes can be achieved due to this blend. Nevertheless, time-consuming numerical methods such as the Finite-Difference Time-Domain (FDTD) approach are employed in the conventional design and optimization of such intricate structures. Re-cently, a machine learning framework was utilized to considerably accelerate the design procedure. Through training on a vast dataset from FDTD runs, a Random Forest surrogate model was developed and trained to predict the filter spectral response from its geometrical parameters with very high accuracy. FDTD simulation results reveal that the proposed rose-like structure produces several sharp transmission peaks of high Q-factor, up to 127.2. Moreover, the machine learning system possesses a high coefficient of determination (R^2 up to 0.986) and excellent predictive ability and can replicate the transmission spectrum within a fraction of the time it takes for conventional runs. Through its powerful volume-based optimization tool and inverse design tool, the proposed mixed-method approach brings within grasp possible future applications of photonic integrated circuits (PICs), high-sensitivity biosensors, and wavelength-division multiplexing (WDM) systems.**

***Index Terms*: Plasmonic Filter, MIM Waveguide (Metal-Insulator-Metal), Circular Resonator, Machine Learning, Quality Fac-tor.Introduction**

I. INTRODUCTION

The rapid growth of modern information technology [1] has contributed to a considerable demand for increased integration density of photonic devices over the past several years. The use of surface plasmon polaritons (SPPs), which are transverse electromagnetic waves propagating at the interface of a metal and a dielectric, represents a promising direction in developing ultra-high-density photonic integrated circuits (PICs) [2, 3]. Structures based on SPPs allow for manipulating light at the sub-wavelength scale, thereby overcoming the traditional diffraction limit of dielectric waveguides [4-6]. Among numerous SPP platforms for building highly integrated optical circuits, metal-insulator-metal (MIM) waveguides are one of the most com-mon. Such waveguides provide many advantages, including strong subwavelength light confinement, decreased propagation losses, and simple fabrication procedures [6, 7]. Various optical devices utilizing SPP structures have been proposed by re-searchers, such as plasmonic filters, demultiplexers, splitters, and sensors [8-28]. Plasmonic filters play an essential role in frequency selection within systems such as wavelength-division multiplexing (WDM) and refractive index sensing [10]. The main targets for these devices are to have a high-quality factor (Q-factor), high transmission efficiency, and an optimal figure of merit (FOM) for enabling their integration in photonics [11, 12]. In recent years, bio-inspired structures that mimic those found in nature, such as butterfly wings or diatom shells, have emerged as novel approaches to create distinctive optical

Received; 2025-10-10 Revised; 2025-12-20 Accepted; 2025-12-28

1. Electrical and Computer Engineering Faculty, Semnan University, Semnan, Iran.
2. Electrical and Computer Engineering Faculty, Semnan University, Semnan, Iran.
3. Electrical and Computer Engineering Faculty, Semnan University, Semnan, Iran.
*Corresponding author: prezaei@semnan.ac.ir

Cite this article as:
Hosseini, S. M. M., Rezaei, P., & Khani, S. (2025). Design and Optimization of a Rose-Inspired Plasmonic Filter using Machine Learning. *Journal of Modeling & Simulation in Electrical & Electronics Engineering (MSEEE)*. Semnan University Press. 6 (1), 43-51.
DOI: https://doi.org/10.22075/MSEEE.2025.39313.1231

prop-erties as well as increase the interaction of light with matter [13-15, 19, 20]. However, the analysis, along with optimization of these nanophotonic structures, traditionally makes use of electromagnetic simulation software based on time-consuming methods, such as the Finite-Difference Time-Domain (FDTD) technique [2]. The numerical approach used requires exhaustive trial-and-error searches over the geometric parameters of the device, an exercise that is computationally intensive and ineffi-cient. In response to such a design challenge, machine learning (ML) algorithms have emerged as an effective solution for building surrogate models capable of rapid and accurate prediction of the spectral properties of a device [1, 16, 29-33]. This AI-assisted approach provides an efficient and reliable means for the inverse design and rapid optimization of complex nano-photonic devices [17, 18]; an approach that has been explored by researchers such as Khani et al for the analysis of plasmonic sensors [1]. In this paper, we combine a novel and high-performance design for a plasmonic filter with an efficient machine learning framework. We propose a multichannel bandpass filter with a unique, rose-inspired geometry on a MIM waveguide platform. First, the performance of this structure is analyzed using the FDTD method to determine its tunable and multichan-nel response. Then, we demonstrate that a Random Forest Regressor, trained on FDTD simulation data, can serve as a powerful surrogate model for accurately predicting the filter's spectral characteristics.

II. METHOD FOR DESIGNING AND SIMULATING STRUCTURES

The proposed plasmonic filter, as shown in Fig. 1, is based on a MIM structure in which air acts as the insulator. The device is arranged on a plasma substrate, and air serves as the dielectric around it. The structure has two main waveguides and a com-plicated system of resonators. The resonator is based on the shape of a rose. It has a central circular cavity with a radius of 300 nm and six smaller satellite circular cavities with a radius of 150 nm.

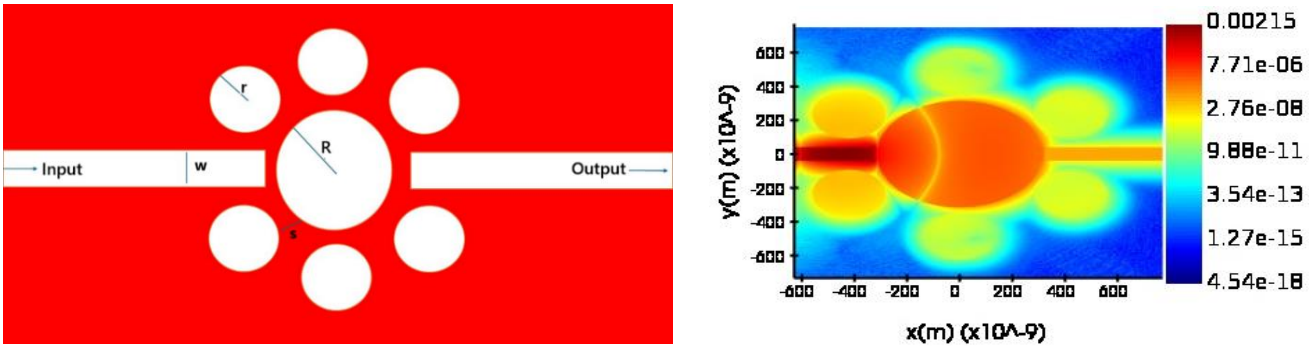

(a) (b)

Fig. 1. (a) Schematic of the proposed rose-inspired plasmonic filter, specifying the key geometric parameters: main resona-tor radius (R), small resonator radius (r), waveguide width (w), and the gap between the central and satellite resonators (s). (b). Electric field distribution in the rose-inspired plasmonic filter at one of the resonance modes. Warmer colors (red and orange) indicate higher field intensity, and cooler colors (blue) indicate lower field intensity. This distribution indicates the effective coupling between the central and satellite resonators.

The main waveguides are also 50 nm wide. Additionally, the electric field distribution in the proposed structure is depicted in Fig. 1 (inset). This image clearly illustrates the interaction and coupling of light within the resonators and the waveguide.

$$\varepsilon(\omega)=\varepsilon_{\infty}-(\omega_p^2)/(\omega^2-i\gamma\omega) \quad (1)$$

The frequency-dependent complex relative permittivity of silver for all components, including the substrate, is characterized by the Drude model:

The parameters for this model were obtained by fitting the experimental data of Palik in the Lumerical software environment, and the following values were used for all simulations: permittivity at infinite frequency $\varepsilon_{\infty}=3.4611$, bulk plasma frequency $\omega_p=9.0264$ eV, and electron collision frequency $\gamma=0.051111$ eV.

All numerical simulations were performed using the commercial FDTD software package from Lumerical. To reduce computational costs, a two-dimensional (2D-FDTD) simulation model was used. The simulation domain was set to 3 μm × 3 μm, and at all boundaries, perfectly matched layer (PML) boundary conditions were used to absorb outgoing waves. To ensure high accuracy, a fine mesh grid with a uniform step of $\Delta x=\Delta y=3$ nm was used. A Mode Source was used to excite the fundamental TM plasmonic mode in the input waveguide, and a frequency-domain field and power monitor was placed at the output to calculate the transmission spectrum ($T=P_{output}/P_{input}$) in the wavelength range of 400 to 1800 nm.

III. MACHINE LEARNING MODEL

To build an effective surrogate of time-costly FDTD computations, a supervised machine learning approach was used. Machine learning offers a quicker substitute to explicit electromagnetic modeling by acquiring the nonlinear transformation from geometrical parameters to optical response non-iteratively, rather than solving Maxwell's equations. A Random Forest Regressor was chosen, as this ensemble learning technique has strong resilience to overfitting and has robust performance even with smaller training sets.

A narrow, high-performance range was systematically swept on three important geometric parameters and used to generate a concentrated dataset of 90 individual FDTD runs. Although this dataset is short, it is carefully chosen

to be optimally appropriate for our task: developing a highly precise local surrogate model used for fine-tuning a previously promising design, rather than laboriously sampling the complete global parameter space. This selective approach permits a powerful yet computationally efficient optimization procedure. The main resonator radius (R) was swept between 290 nm and 310 nm, the satellite resonator radius (r) between 140 nm and 160 nm, and the gap (s) was tuned within values between -10 nm and +10 nm. For each simulation, the model's inputs were the three geometrical parameters [R, r, s], and the output was the corresponding transmission spectrum at 1401 discrete points within a wavelength interval of 400-1800 nm. Only then was the dataset normalized, shuffled, and divided into training and test sets in order to produce unbiased performance measures. The learned model sufficiently recreated FDTD-simulated spectra with a very high coefficient of determination (R^2>0.95) significantly lowered the design cycle and made real-time optimization feasible.

IV. RESULTS AND DISCUSSION

In this section, the step-by-step design and optimization process of the proposed plasmonic filter, from a basic structure to the final geometry, is presented and analyzed.

A. Initial Design and Bio-Inspiration

Our design process began with a basic and conventional structure in plasmonic filters: namely, a single circular resonator coupled to two MIM waveguides (Fig. 2a). Although this simple structure is capable of generating resonance modes, it usually has limitations in terms of the number of channels and the quality factor (Q-factor). To improve the performance and achieve a more complex and efficient spectral response, we drew inspiration from nature. Inspired by the symmetry and structure of a rose, six smaller circular resonators (satellites) were added around the central resonator (Fig. 2b). This hexagonal symmetry, analogous to photonic crystal structures, facilitates complex mode coupling between the resonators, which is essential for enhancing the quality factor and creating multiple channels.

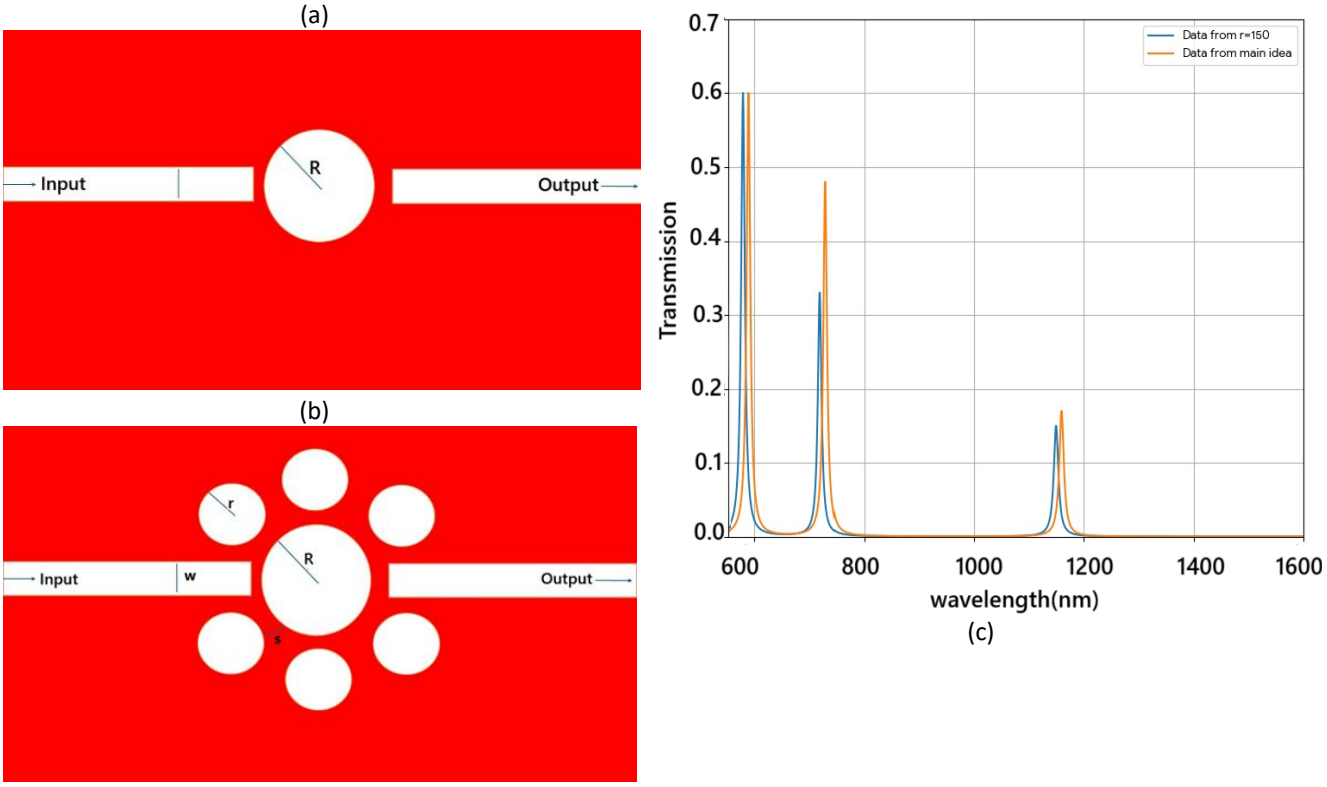

Fig. 2. (a) Schematic of the initial structure with a single circular resonator. (b) The final rose-inspired structure, with the addition of six satellite resonators. (c) Comparison of the transmission spectra, showing that the final rose-inspired structure (Data from r=150) generates additional, sharper transmission peaks compared to the initial structure.

The center-to-center distance between the main resonator and each small resonator was determined by considering a fixed gap of 20 nm. The objective of this design was to create a more complex coupling between different modes, thereby generating multiple resonance peaks with higher quality. As shown in Fig. 2c and 2d, the addition of the satellite resonators leads to a change in the field distribution pattern and the formation of additional transmission peaks, indicating an increase in the number of resonance modes and an improvement in the filter's spectral performance.

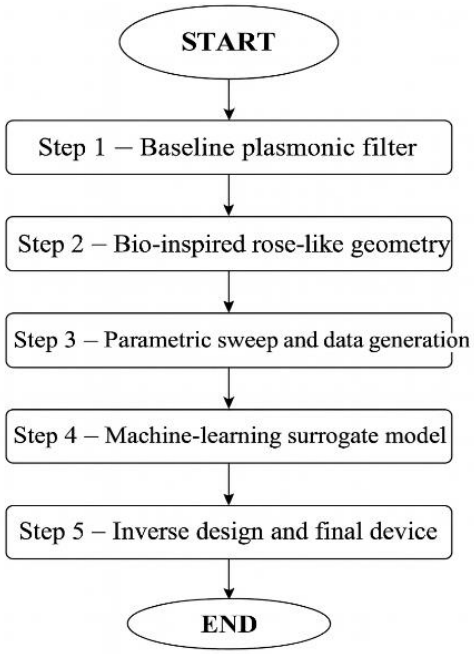

Fig. 3. The proposed flowchart of filter design.

The complete flowchart of the proposed design methodology is summarized in Fig. 3, which outlines the step-by-step progression from the baseline MIM filter to the bio-inspired rose geometry, the parametric sweep, and the surrogate-assisted inverse design.

B. Dual-Mode Operation and Physical Analysis Origin of the Performance

The observed dual-mode functionality of the rose-inspired filter is governed by the Fano resonance phenomenon. This effect arises from the interference between two distinct electromagnetic states: a spectrally broad 'bright mode' supported by the directly-coupled central resonator, and spectrally narrow 'dark modes' supported by the isolated satellite resonators [22, 26]. The bright mode facilitates a high-throughput pathway for light, corresponding to the high-transmission resonance. In contrast, the dark modes act as high-Q energy reservoirs, excited only indirectly via near-field coupling. The interference between these two pathways carves a sharp, asymmetric resonance out of the broad transmission spectrum, creating the high-selectivity, high Q-factor peak. This physical interpretation is definitely verified by our modal field investigation. It is evident from the latter that at the high-transmission resonance, energy is mainly concentrated within the central resonator and hence verifies its bright-mode nature. At the high-Q resonance, the field is highly localized within the satellite resonators and shows clear visual verification of the energy-storing dark modes. This scenario verifies that the structural geometry is absolutely designed such that it is capable of accommodating the Fano interference essential for its double-function functionality.

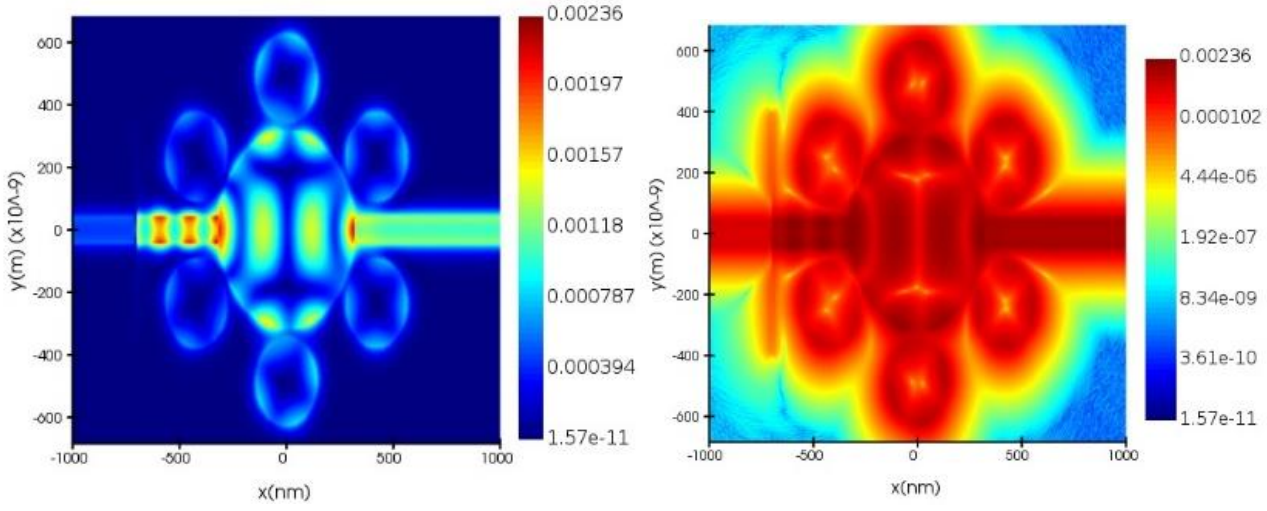

(a) (b)

Fig. 4. (a) Bright resonance at λ ≈ 774.2 nm, with the field being strongly coupled to the dominant waveguide and the central cavity. (b) Dark resonance at λ ~ 1145.5 nm, where the optical energy is mainly localized inside the satellite resonators with a sharp and high-Q resonance and small coupling to the waveguides. Such mode profiles demonstrate the plasmonic processes and thus meet the reviewer's demand for the visualization of field distributions for all resonance modes.

C. Parametric Optimization of the Rose-Inspired Structure

The rose-inspired geometry was defined, and then its dimensions were optimized through a thorough parametric analysis. Initially, the impact of the primary resonator radius (R) was examined. While keeping the small resonator radius constant at r = 140 nm, Fig. 5 contrasts the outcomes for three values of R: 300 nm, 310 nm, and 315 nm. It is evident that the main modes' transmission efficiency (T max) greatly increases as R rises. We specifically achieved the best performance in the R = 315 nm case, with a quality factor (Q-factor) of up to 127.2 and a transmission efficiency of up to 80% (see Table I for full details). Consequently, this arrangement was chosen as the main resonator's ideal radius.

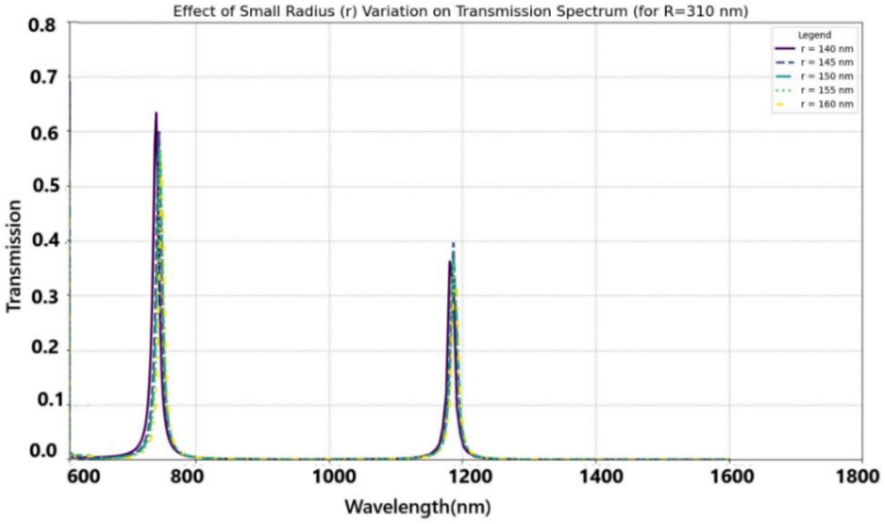

(a)

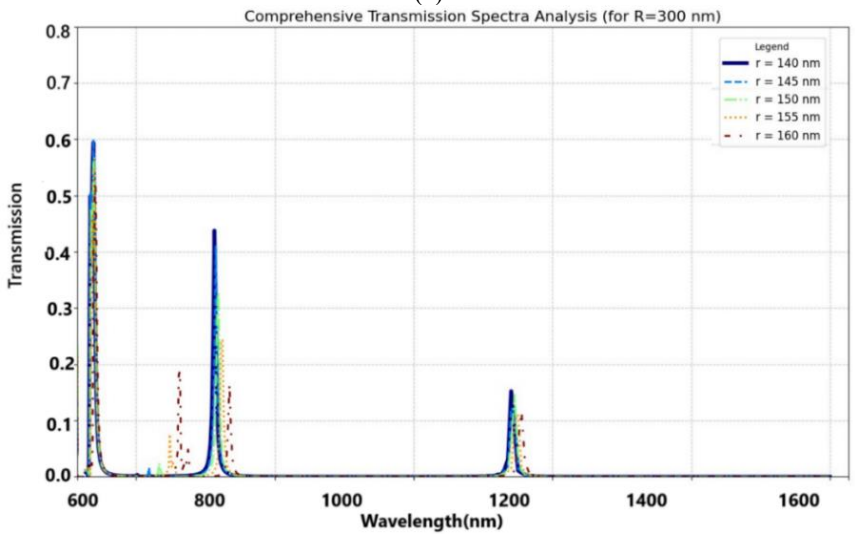

(b)

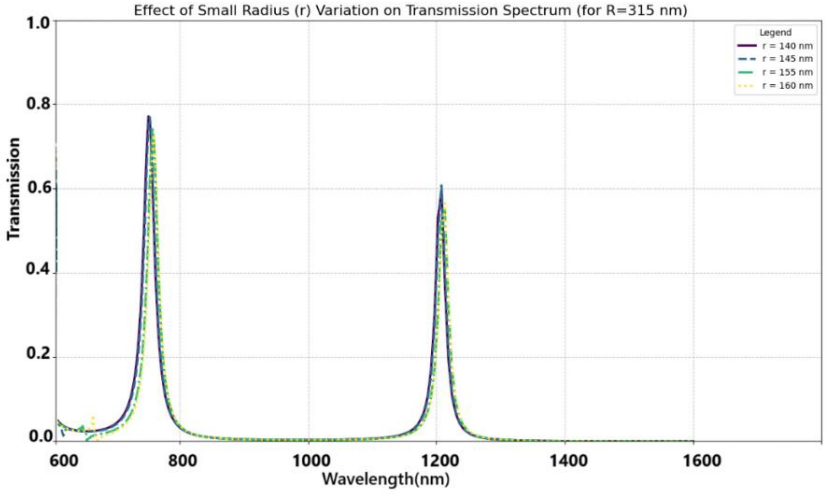

(c)

Fig. 5. Comparison of transmission spectra for three different main resonator radii (R), while keeping the satellite resonator radius constant (r=140 nm): (a) R = 300 nm, (b) R = 310 nm, and (c) R = 315 nm.

In the next step, to evaluate the fabrication tolerance and robustness of the optimized structure (R = 315 nm, r = 140 nm), the effect of variations in the gap (s) between the main waveguide and the resonator system was investigated. Fig. 6 shows that minor variations in this gap (from -10 to +10 nm) create predictable and gradual changes in the transmission spectrum, without disrupting the overall nature of the filter's performance. The plot shows that minor variations in the gap create predictable and gradual shifts in the resonance peaks, indicating the design's robustness against small fabrication processes.

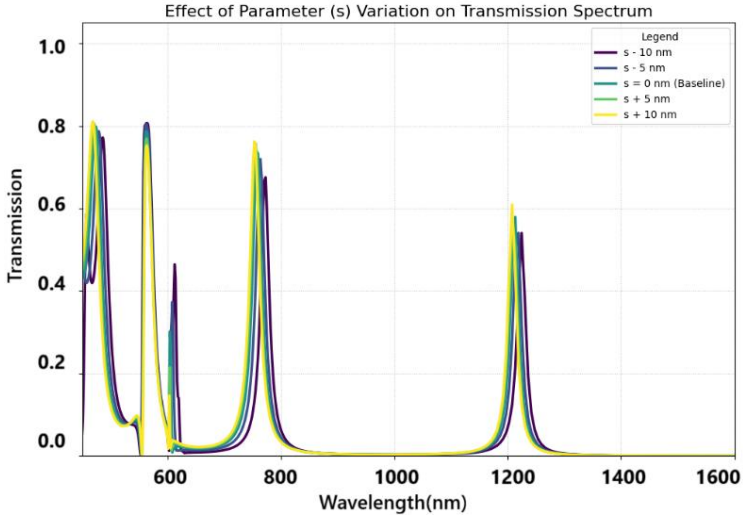

Fig. 6. Analysis of the effect of gap (s) variation on the transmission spectrum of the optimized structure (R = 315 nm, r = 140 nm).

D. The Machine Learning Surrogate Model's Performance

By contrasting the Random Forest model's predictions with FDTD simulation data that was not utilized during training, the model's accuracy was confirmed. As shown in Fig. 7 for the optimal structure (R=315nm), the simulated spectra (solid black line) and the AI-predicted spectra (red dashed line) match very well, achieving an R^2 score of 0.978.

For a more quantitative and detailed assessment of the model's performance, Fig. 8 presents a comparison of heatmaps. Fig. 8(a) shows the percentage prediction error across the parameter space. It is evident that the model performs extremely well in the overwhelming majority of parameter combinations, with a prediction error of less than 5% and reaching a minimum error of just 0.3% (for R=315 nm, r=150 nm). Fig. 8(b) visualizes the model's R^2 scores for the same parameter sweeps. These results quantitatively confirm the high accuracy and robustness of the model, with scores consistently above 0.93 and reaching a peak value of 0.986. This thorough analysis not only demonstrates the model's reliability for design and optimization but also precisely identifies the regimes of its highest performance.

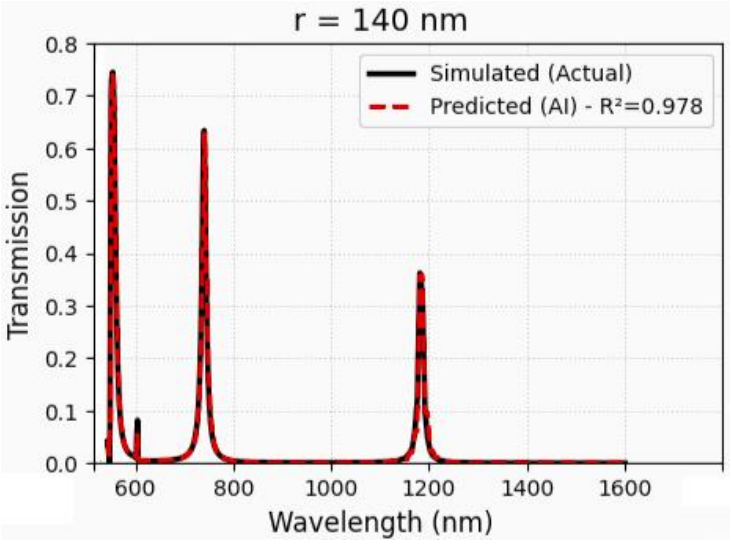

Fig. 7. Comparison of the FDTD-simulated (Actual) and the AI-predicted transmission spectra for the optimal filter configuration (R = 315 nm, r = 140 nm).

The high agreement between the two curves, confirmed by an R^2 score of 0.978, demonstrates the accuracy and reliability of the surrogate mode. Fig. 8 shows the percentage prediction error across the parameter space for a more quantitative and detailed assessment of the model's performance. The radius of the satellite resonator (r) is swept along the vertical axis of each map; however, the error heatmaps for three values of constant principal radii (R = 300, 310, and 315 nm) are compared here. Each cell in these maps shows the relative percentage error between

the FDTD-simulated spectrum and the AI-predicted spectrum. With a prediction error of less than 5%, the model performs extremely well in the overwhelming majority of parameter combinations, as evident from both the numerical values and the color scale (where lower error is indicated by darker color). The high accuracy and robustness of the model, as hinted earlier by the R^2 score, are quantitatively confirmed by these results. However, this thorough study also makes it clear that the error rate very slightly rises as the radius r becomes larger, especially in the case of R = 315 nm. In addition to demonstrating the reliability of the model for design and optimization, this transparency about the model's performance serves to precisely identify the regimes where the model falters.

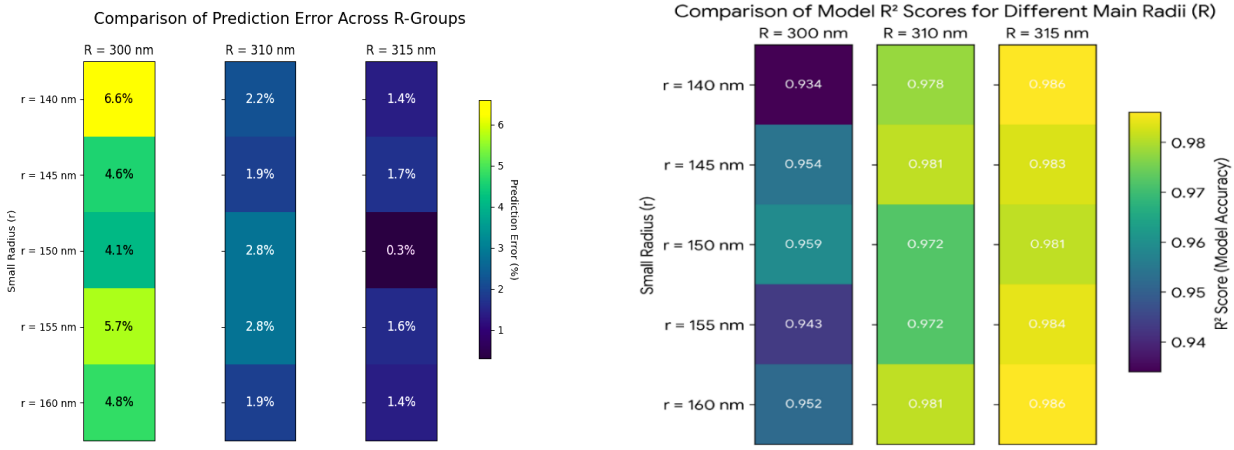

(a) (b)

Fig. 8: Heatmaps comparing the performance of the machine learning model across different geometries. (a) Prediction error percentage, where each column represents a constant main radius (R) and the vertical axis shows the variation of the satellite radius (r). Darker colors indicate lower error and higher agreement with FDTD simulations. (b) Model R^2 Scores for the same parameter sweeps. Brighter/warmer colors indicate higher model accuracy (a score closer to 1).

E. Performance Metrics and Comparison

To quantitatively evaluate the filter's performance, key metrics including the quality factor (Q-factor) and maximum transmission efficiency (T_{max}) were calculated. Table I summarizes these metrics for a set of configurations.

TABLE I
Calculated Performance Metrics for the Rose-Inspired Filter.

R (nm)	r (nm)	Mode	Resonance λ (nm)	Transmission (%)	FWHM (nm)	Q-factor
300	140	1	722.9	44.1	14.1	51.3
		2	1152.1	16.1	9.4	122.6
310	140	1	760.1	62.4	14.9	51.0
		2	1150.1	38.6	9.2	125.0
315	140	1	774.2	80.0	16.5	46.9
		2	1145.5	60.1	9.0	**127.2**

The primary advantage of our design lies in its dual-mode operation, wherein it fulfills two distinct functions within the same structure: a high-selectivity mode for sensing and a high-throughput mode for signal transmission. To numerically assess this unique trade-off, we introduce a Figure of Merit (FOM). The measure is designed to prefer structures that offer both a sharp, high-Q resonance (Mode 2) and another efficient high-transmission passband (Mode 1) simultaneously, encapsulating the practical usefulness in multi-functional integrated circuits. The FOM is expressed as:

$$\text{FOM} = \frac{Q_{mode2} \cdot T_{mode\,1}}{100}, \quad (2)$$

where QMode2 is the Fano sharp Mode 2 quality factor, and TMode1 is the percentage peak transmission of the broad bright-mode (Mode 1) resonance. Because of the requirement that a truly useful dual-mode device must excel in both areas, a multiplicative format was chosen. This FOM prevents the overall score from being seriously penalized if either the Q-factor or transmission is diminished and hence serves as a proper gauge of the device's real-world utility. In our thorough analysis, our proposed filter is tested against several state-of-the-art designs listed in Table II For easier comparison with single-mode filters, we have included the conventional Q × T Product figure of merit.

TABLE II
Comparison of the Proposed Plasmonic Filter with Reported Designs in the Literature

Reference (Year)	Resonator Structure	Resonance Wavelength (λ)	Q-factor	Transmission (T)	Q×T	FOM
This work (Mode 1)	Rose-Inspired Resonator	774.2 nm	46.9	80.0%	3752	101.76
This work (Mode 2)	Rose-Inspired Resonator	1145.5 nm	127.2	60.1%	7645	101.76
Korani et al. (2024) [28]	Ring with silver nanorods	1205.8 nm	207	93%	19251	N/A
Wang et al. (2022) [7]	Double split circular ring	591 nm	~49	~80%	~3920	N/A

Here is a comparison of our filter's performance metrics against other relevant works. As shown in Table II, our proposed filter exhibits competitive performance even in conventional figures of merit such as the Q × T product, especially in its high-Q mode. Although individual Q × T values may exceed those of specific single-mode designs or configurations, our structure is characterized by its double functionality. This distinguished feature is quantitatively reflected by our tailored FOM, which is found at a high level of 10176. This quantitatively points up our design's excellent multifunctional balance at the cost of conventional single-purpose filters.

V.CONCLUSION

In this research, we proposed a new, bio-inspired multichannel plasmonic filter based on a rose-shaped nanostructure and numerically characterized it. Sharp and controllable transmission peaks were attained, and the potential application for use in sophisticated filtering applications was demonstrated. To circumvent the computational expense of typical FDTD calculations, a tractable Random Forest-based surrogate model was formulated and calibrated. It is utilized to estimate the transmission spectra ($R^2 > 0.95$) very accurately, and the application of this model permits rapid design investigation and optimum design. The filter's proposed performance was compared against a number of state-of-the-art designs. Although other designs might provide slightly better transmission or peak Q-factors within a solitary mode, our design stands out due to its double-mode capabilities. Such superiority was numerically encapsulated in a specially-defined FOM, which provided a high number of about 102. This finding verifies the superior trade-off between two distinct operating regimes: a high-Q mode ($Q \approx 127.2$) suited for high-resolution sensing platforms and a high-transmission mode ($T \approx 80.0\%$), suited for applications where stable signal throughput is required. This tunability can be supported further by its comparable performance, rendering the rose-shaped filter a strong component for next-generation PICs, such as WDM systems and on-chip biosensors. Experimental confirmation of performance for the optimized design and exploration in its application in high-sensitivity sensing platforms will be addressed in later work. The dominant resonances at $\lambda \approx 774.2$ nm and $\lambda \approx 1145.5$ nm lie within the technologically important NIR region, making the filter highly suitable for compact wavelength-division multiplexing (WDM) modules and high-resolution refractive-index sensing applications. The coexistence of these modes enables simultaneous signal routing and sensing on the same photonic chip. Future work will focus on experimental validation of the proposed design and its integration into high-sensitivity plasmonic sensing platforms.

ACKNOWLEDGMENTS

This research was supported by Semnan University. Also, the authors would like to thank the editor and reviewers for their valuable comments.

FUNDING

No funding was received for this research.

CONFLICTS OF INTEREST

The third author is an Assistant Editor for Modeling and Simulation in Electrical and Electronics Engineering Journal and was not involved in the editorial review or the decision to publish this article.

DATA AVAILABILITY

All the data analyzed in this study are provided within this published article.

AUTHOR CONTRIBUTIONS

SMMH: Conceptualization, Methodology, Software, Validation, Writing – original draft, review & editing. PR: Methodology, Validation, Supervision, Writing – review and editing. SK: Methodology, Validation, Writing – review and editing.

REFERENCES

[1] S. Khani, P. Rezaei, and M. Rahmanimanesh, "Machine learning analysis of a Fano resonance-based plasmonic refractive index sensor using U-shaped resonators," *Scientific Reports*, vol. 15, p. 23857, 2025.

[2] S. Khani, M. Danaie, and P. Rezaei, "Design of a Single-Mode Plasmonic Bandpass Filter Using a Hexagonal Resonator Coupled to Graded-Stub Waveguides," *Plasmonics*, vol. 13, pp. 2177–2186, 2018.

[3] M. Aftab, M. S. Mansha, T. Iqbal, and M. Farooq, "Surface Plasmon Excitation: Theory, Configurations, and Applications," *Plasmonics*, vol. 19, pp. 1701–1719, 2024.

[4] S. A. Maier, "Plasmonics: Metal Nanostructures for Subwavelength Photonic Devices," *IEEE Journal of Selected Topics in Quantum Electronics*, vol. 12, no. 6, pp. 1214-1220, Nov. 2006.

[5] R. F. Oulton, G. Bartal, D. F. P. Pile, and X. Zhang, "Confinement and propagation characteristics of subwavelength plasmonic modes," *New Journal of Physics*, vol. 10, p. 105018, Oct. 2008.

[6] M. H. Fuad, M. F. Nayan, and R. R. Mahmud, "Advances in Surface Plasmon Resonance-Based PCF and MIM Sensors," *Plasmonics*, 2025.

[7] S Khani, M Hayati, Optical sensing in single-mode filters based on surface plasmon H-shaped cavities, Optics Communications, 2022, 505, 127534.rezaei

[8] M. Z. U. Rahman, T. C. E. Cheng, M. T. Islam, and N. Misran, "Ultra-Wide-Band Band-Pass Filters Using Plasmonic MIM Waveguide-Based Ring Resonators," *IEEE Photonics Technology Letters*, vol. 30, no. 19, pp. 1715-1718, Oct. 2018.

[9] S. Kumar, *et al*., "Nanophotonic Ring Resonator Based on Slotted Hybrid Plasmonic Waveguide for Biochemical Sensing," *IEEE Sensors Journal*, vol. 23, no. 6, pp. 5695-5702, Mar. 2023.

[10] F. Liu, Y. Cui, S. Yan, and B. Huang, "A MIM Waveguide Refractive-Index Construction According to SPPs and Fano Resonance," in *Proc. 5th Int. Conf. Intell. Control, Meas. Signal Process. (ICMSP)*, 2023, pp. 1011-1014.

[11] A. V. Maslov and M. Miyawaki, "Confinement factors and optical gain in subwavelength plasmonic resonators," *Journal of Applied Physics*, vol. 108, no. 8, p. 083105, Oct. 2010.

[12] S.A. Khatami, P. Rezaei, "Coupled mode theory analysis of the graphene-based multi-band superabsorber for selective sensing application," Diamond and Related Materials, vol. 158, 112690, 2025.

[13] A. L. Musgrove, *et al*., "Bio-inspired photonic and plasmonic systems for gas sensing: applications, fabrication, and analytical methods," *Journal of Optical Microsystems*, vol. 4, no. 2, p. 020902, 2024.

[14] Z. Jakšić, M. Obradov, and O. Jakšić, "Bio-Inspired Nanomembranes as Building Blocks for Nanophotonics, Plasmonics and Metamaterials," *Biomimetics*, vol. 7, no. 4, p. 222, Dec. 2022.

[15] A.H. Asl, M. Khajenoori, Green extraction in separation technology, CRC Press, 2021.

[16] S. Chugh, S. Ghosh, A. Gulistan, and B. M. A. Rahman, "Machine Learning Regression Approach to the Nanophotonic Waveguide Analyses," *Journal of Lightwave Technology*, vol. 37, no. 24, pp. 6080-6089, Dec. 2019.

[17] Z. Jakšić, S. Devi, O. Jakšić, and K. Guha, "A Comprehensive Review of Bio-Inspired Optimization Algorithms Including Applications in Microelectronics and Nanophotonics," *Biomimetics*, vol. 8, no. 3, p. 278, Jun. 2023.

[18] S.A. Khatami, P. Rezaei, P. Zamzam, S. Hadipour, S. Khani, "Smith chart analysis for transmission line method validation of a simple graphene-based absorber in sugar molecules detection," Results in Physics, vol. 77, pp. 108464, October 2025.

[19] P. Cheng, *et al*., "Bio-inspired self-assembly of large area 3D Ag@SiO2 plasmonic nanostructures with tunable broadband light harvesting," *Applied Materials Today*, vol. 25, p. 101238, 2021.

[20] M. K. Akbari, *et al*., "Bioinspired patterned photonic junctions for plasmon-enhanced metal photoluminescence and fluorescence: design of optical cavities for near-infrared electronics," *Materials Today Energy*, vol. 26, p. 101003, 2022.

[21] S. Khani, M. Danaie, P. Rezaei, "Tunable single-mode bandpass filter based on metal-insulator-metal plasmonic coupled U-shaped cavities," IET Optoelectronics, vol. 13, no. 4, pp. 161-171, 2019.

[22] H. Geng *et al*., "Symmetry Breaking Induced Multiple Fano Resonances for Plasmonic Nanosensing," *Plasmonics*, 2025, doi: 10.1007/s11468-024-02318-y.

[23] S. Javid, F. Tavakkol Hamedani, P. Rezaei, S. Khani, "Designing scalable single-mode to seven-mode plasmonic filters utilizing disk and ring-shaped resonators," Results in Optics, vol. 21, 100919, 2025.

[24] R. Jaswal, *et al*., "Plasmonic nanoparticle-integrated nanofibers: advancements in nanobiotechnology for biomedical applications," *Journal of Pharmaceutical Investigation*, 2025.

[25] J. Zhou, Z. Wu, C. Jin, and J. X. J. Zhang, "Machine learning assisted dual-functional nanophotonic sensor for organic pollutant detection and degradation in water," *npj Clean Water*, vol. 7, no. 1, p. 3, 2024.

[26] Y. Sharma, B. Joshi, and R. Zafar, "Split Ring Resonators-Based Plasmonics Sensor with Dual Fano Resonances," *IEEE Sensors Journal*, vol. 21, no. 5, pp. 6050-6056, Mar. 2021.

[27] A.R. Jalalvand, Z. Rashidi, M. Khajenoori, "Sensitive and selective simultaneous biosensing of nandrolone and testosterone as two anabolic steroids by a novel biosensor assisted by second-order calibration," Steroids, vol. 189, 109138, 2023.

[28] N. Korani, L. Hajshahvaladi, and M. Danaie, "Realization of a single-mode plasmonic bandpass filter based on a ring-shaped resonator and silver nanorods," *Optical and Quantum Electronics*, vol. 56, no. 23, 2024.

[29] Q. Wang, *et al*., "Research on fiber optic surface plasmon resonance biosensors: A review," *Photonic Sensors*, vol. 14, p. 240201, 2024.

[30] M. H. Ehsani, S. Alamdari, "Biomaterials: Fundamentals, processing, and applications. In: Ikhmayies, S.J. (eds) Advances in Biomaterials Research. Advances in Materials Research and Technology. Springer, 2025.

[31] S.M. Ebadi, S. Khani, Highly-miniaturized nano-plasmonic filters based on stepped impedance resonators with tunable cut-off wavelengths, Plasmonics 18 (4), 1607-1618, 2023.

[32] J. Wang, *et al*., "Bandpass Half-Mode Substrate Integrated Plasmonic Filters with Steep Roll-Offs," *IEEE Photonics Technology Letters*, vol. 37, no. 5, pp. 269-272, Mar. 2025.

[33] Palik, E. D. (Ed.), Handbook of Optical Constants of Solids, Vol. 1, Academic Press, New York, USA, 1985.

Semnan University

Journal of Modeling & Simulation in Electrical & Electronics Engineering (MSEEE)

Journal homepage: **https://mseee.semnan.ac.ir/**

ISSN: 2821-0786

Robust Trajectory Estimation for Maneuvering Targets Using an Adaptive Interacting Multiple Model Extended Kalman Filter

Alireza Jarrah[1], Hadi Asharioun[2]*and Mohammadhossein Hashemi[3]

***Abstract*-- Accurately tracking maneuvering targets remains a significant challenge in fields such as autonomous navigation and surveillance. This paper presents a robust solution using an Interacting Multiple Model Extended Kalman Filter (IMM-EKF). The proposed architecture adaptively combines three distinct kinematic models: a Near Constant Velocity (NCV) model for linear motion, a Coordinated Turn (CT) for constant turn rates, and a Coordinated Turn with Rate and Acceleration (CTRA) to handle aggressive maneuvers. The IMM framework dynamically weights each model's contribution based on the measurement likelihood, producing a fused state estimate that is more reliable than any single-model filter. The algorithm's performance was rigorously validated against ground truth data, demonstrating high precision with a position Root Mean Square Error (RMSE) of 0.3117 m and a yaw RMSE of 2.1614 degrees. Furthermore, the filter's statistical integrity was confirmed through consistency tests, with 94.16% of the Normalized Innovation Squared (NIS) values falling within the 95% confidence interval. These results underscore the effectiveness of the proposed multi-model approach for complex and dynamic trajectory estimation.**

***Index Terms*- State Estimation; Trajectory Estimation; Maneuvering Target Tracking; Extended Kalman Filter; Interacting Multiple Model; Motion Models**

I. INTRODUCTION

THE advent of autonomous systems, particularly in vehicular navigation and advanced driver-assistance systems, has rendered the accurate and reliable tracking of dynamic objects a critical area of research. The ability to precisely estimate the state, including position, velocity, and orientation, of surrounding vehicles is fundamental for safe path planning, collision avoidance, and overall situational awareness. This concept of awareness is multifaceted, extending beyond just the external environment to include the internal state of the driver. For instance, recent research has focused on developing comprehensive Fuzzy Driver Monitoring Systems that integrate parameters such as vehicle speed and driver drowsiness to automatically identify dangerous behaviors [1]. A critical component of such systems is the accurate interpretation of non-verbal cues, where deep learning techniques such as Convolutional and Recurrent Neural Networks are employed to classify facial expressions and infer the driver's level of fatigue [2]. While these technologies focus on the ego-vehicle's driver, the work presented here addresses the complementary challenge of perceiving the state of external maneuvering targets. A primary

Received; 2025-11-05 Revised; 2026-01-21 Accepted; 2026-02-07

1. Faculty of Electrical Engineering, Shahid Beheshti University, Tehran, Iran.
2. Faculty of Electrical Engineering, Shahid Beheshti University, Tehran, Iran.
3. Faculty of Electrical Engineering, Shahid Beheshti University, Tehran, Iran.

*Corresponding author Email: asharioun@sbu.ac.ir

Cite this article as:
Jarrah, A., Asharioun, H. & Hashemi, M H. (2026). Robust Trajectory Estimation for Maneuvering Targets Using an Adaptive Interacting Multiple Model Extended Kalman Filter. *Journal of Modeling & Simulation in Electrical & Electronics Engineering (MSEEE)*. Semnan University Press . *6 (1)*, 53-65.
DOI: https://doi.org/10.22075/MSEEE.2026.39451.1233

challenge in this domain is the ability to maintain tracking precision when a target deviates from simple, predictable motion—that is, when it executes a maneuver. The dynamic nature of these targets, which can seamlessly transition between straight-line motion, coordinated turns, and sharp accelerations, poses a significant challenge to conventional estimation algorithms. Single-model filters, which operate under a fixed set of dynamic assumptions, often fail to adapt to these behavioral shifts, leading to a degradation in accuracy or, in worst-case scenarios, a complete loss of track.

To overcome these limitations, a substantial body of research has been devoted to developing more sophisticated state estimation techniques capable of handling target maneuvers. Study [3] introduces a novel IMM–MCEKF filter for GPS navigation, which combines the IMM and the maximum correntropy criterion. IMM is utilized to alter the covariance parameters of measurement noises in parallel filters to address measurement uncertainty. MCC replaces the minimal mean-square-error optimization criterion in the EKF to specifically enhance performance when dealing with non-Gaussian noise and outlier-type multipath interference. Gadsden et al. [4] introduced a novel SVSF-IMM method for nonlinear target tracking, comparing it with the conventional EKF-IMM approach in an Air Traffic Control scenario. The SVSF-IMM method achieved a 30% improvement in position accuracy and demonstrated robust, stable performance due to the SVSF switching gain. Study [5] compares the EKF and the IMM approach for nonlinear maneuvering target tracking. IMM utilized linear constant velocity and CT models. The study found that IMM is more robust and accurate for large ranges of nonlinearity and high noise, provided the model count is optimized. The IMM5CKF algorithm is proposed [6] to enhance the accuracy and quick response of maneuvering target tracking. Integrating a five-degree Cubature Kalman Filter (CKF) with the IMM framework, it simultaneously handles models via a Markov Chain. Gao et al. [7] propose four improved IMM-based algorithms for nonlinear maneuvering target tracking. They achieve better accuracy and efficiency than traditional methods, with Unscented Kalman Filter (UKF)-MIMM offering the best accuracy and EKF-SIMM the fastest performance.

Additionally, [8] proposes a mobile location estimation algorithm for harsh wireless environments using an interacting multiple model framework with a Markov chain to handle NLOS transitions. The method fuses TOA and RSS data and applies the CKF for nonlinear estimation, achieving accurate tracking of maneuvering mobile stations. An IMM-CKF algorithm is proposed [9] for tracking maneuvering targets using angular measurements. By integrating the CKF into the IMM framework, the method improves tracking accuracy and reduces computation time compared to the IMM-UKF approach. The Autoencoder IMM filter is proposed [10] for maneuvering target tracking. This hybrid framework embeds an IMM, which uses models like NCV and CT, within an autoencoder to facilitate nonlinear transformations. The goal is to help the IMM quickly identify mode changes, leading to improved state estimation compared to classical methods. Study [11] proposes a smart IMM filter using the EKF for bearing-only 2D maneuvering target tracking. To improve state estimation, the algorithm employs a second-order Markov model instead of the first-order IMM, allowing for a more accurate description of the target's maneuvering behavior. Simulation results confirmed that the second-order model provides more efficient tracking with reduced error. The IMM-MOT framework [12] introduces an IMM filter for 3D Multi-Object Tracking, overcoming the limitation of single motion models in fitting complex, varying motion patterns. The tracker dynamically combines models, including constant velocity, constant acceleration, constant turn rate and velocity, and CTRA, employing an EKF for nonlinear models. This approach yields more accurate predictions, achieving high performance on the NuScenes dataset.

The authors in [13] proposed a variational Bayesian adaptive framework that enhances traditional IMM methods by enabling faster model switching through real-time change-point updates. Their approach jointly optimizes state and model posteriors, achieving superior tracking performance, particularly in highly maneuverable target scenarios. Study [14] presents an intelligent tracking framework for highly maneuvering aerial targets by integrating a TCN–LSTM neural prediction model into a UKF. By leveraging recurrent architectures to approximate complex target dynamics and embedding them through the Unscented Transformation, the proposed TCN-LSTM-UKF method mitigates model-construction challenges and transition delays, achieving significantly improved tracking performance under high-maneuver conditions. An adaptive constant acceleration (ACA) model is integrated with a strong tracking square-root CKF (ST-SCKF) to improve maneuvering target tracking. By linking acceleration, velocity, and jerk through Taylor expansion and adaptively adjusting process noise, the ACA-ST-SCKF achieves higher accuracy, better adaptability, and lower computational complexity compared with traditional adaptive and IMM-based filters [15]. Leveraging variational inference, study [16] proposes an adaptive interacting multiple model algorithm for tracking multiple maneuvering extended targets. The method augments the state to capture time-varying orientation and shape and updates model probabilities in real-time, significantly improving tracking accuracy and robustness over conventional IMM approaches.

To address the limitations of single-model estimators in highly dynamic environments [12], this paper presents a comprehensive adaptive tracking framework based on the IMM-EKF. The distinct contribution of this work lies in the rigorous integration and statistical validation of a specialized kinematic model bank— NCV, CT, and CTRA. By explicitly incorporating the CTRA model, the framework accounts for complex dynamics involving simultaneous linear acceleration and variable turn rates, a capability often lacking in standard implementations. Furthermore, unlike studies that rely on position and velocity error metrics [4, 11], this research provides a holistic assessment of tracker reliability through extensive statistical consistency tests (NIS and NEES). This approach ensures the filter remains robust and statistically

sound across a challenging hybrid scenario encompassing both smooth S-curves and sharp 90-degree maneuvers.

The remainder of this paper is organized as follows: Section 2 details the proposed methodology, including the formulation of the motion models and the recursive steps of the IMM-EKF algorithm. Section 3 describes the experimental setup, the dataset generation, and the evaluation metrics. In Section 4, the simulation results are presented and comprehensively analyzed. Finally, Section 5 concludes the paper with a summary of the findings and suggestions for future work.

II. Proposed Method

To address the challenge of tracking maneuvering targets, this paper proposes a hybrid estimation framework based on the IMM architecture [17]. The core philosophy of this approach is to not rely on a single, one-size-fits-all motion model, but to employ instead a bank of specialized estimators that operate in parallel.

The proposed methodology is structurally divided into two key components. First, a set of diverse kinematic models is established, where each model is optimized to describe a specific dynamic behavior, from simple linear motion to complex accelerating turns. Second, the IMM algorithm itself serves as the high-level probabilistic engine. This engine's role is to dynamically weigh the contribution of each specialized model based on real-time measurement data and intelligently fuse their estimates into a single, robust, and highly accurate output.

A. Motion Models

Accurate tracking of a maneuvering target necessitates a model that can adapt to its changing dynamics. A single motion model is often insufficient, as it cannot adequately describe the full spectrum of behaviors, ranging from straight-line trajectories to sudden, aggressive turns. To address this limitation, this research employs a bank of three distinct motion models to cover a wide array of kinematic behaviors. This work integrates the NCV, the CT, and the CTRA models. The subsequent sections will provide a detailed formulation of each of these models.

- *Near Constant Velocity (NCV)*

The NCV model is the simplest representation of target dynamics, designed to describe motion along straight or near-straight paths. It operates under the assumption that the target maintains a constant velocity vector, making it highly effective for non-maneuvering phases of a trajectory. The state of the target is defined in a Cartesian coordinate system by the state vector (1):

$$x_{NCV} = [p_x, p_y, v_x, v_y]^T \tag{1}$$

where (p_x, p_y) represents the target's position, and (v_x, v_y) are the corresponding velocity components along the x and y axes.

The model's dynamics are governed by a linear state transition equation, which projects the state from a previous time step $k-1$ to the current time step k (2):

$$x_k = F_{NCV} x_{k-1} + w_{k-1} \tag{2}$$

The state transition matrix (3), F_{NCV}, is derived from basic kinematic principles, updating the position based on the velocity over the time interval Δt:

$$F_{NCV} = \begin{bmatrix} 1 & 0 & \Delta t & 0 \\ 0 & 1 & 0 & \Delta t \\ 0 & 0 & 1 & 0 \\ 0 & 0 & 0 & 1 \end{bmatrix} \tag{3}$$

The term w_{k-1} represents the process noise, which is modeled as a zero-mean white Gaussian noise with a covariance matrix Q_{NCV}. This noise accounts for slight, unmodeled accelerations or random deviations from a perfectly constant velocity, thereby preventing the filter from becoming overconfident. Despite its simplicity and efficiency, the primary limitation of the NCV model is its inherent inability to accurately track targets during turns or significant maneuvers, resulting in a rapid increase in estimation error.

- *Coordinated Turn (CT)*

For tracking targets during periods of sustained turning, the CT model is employed. This model is specifically designed to describe motion along an arc with a constant turn rate and speed. It provides a more accurate representation of maneuvering behavior compared to the NCV model by adopting a different kinematic state. The state vector for the CT model is defined as (4):

$$x_{CT} = [p_x, p_y, v, \psi, \dot{\psi}]^T \tag{4}$$

where (p_x, p_y) are the Cartesian positions, v is the magnitude of the velocity (speed), ψ is the yaw angle (heading), and $\dot{\psi}$ (also denoted as ω) is the turn rate.

It is important to note that the CT and CTRA models are kinematic and operate under a zero sideslip assumption. Therefore, the vehicle's body orientation, or Yaw (ψ), is assumed to be instantaneously aligned with the velocity vector, or heading.

This zero-sideslip assumption is justified because the proposed method employs kinematic models rather than dynamic ones. In typical urban driving scenarios on paved roads with high friction coefficients, the vehicle's velocity vector aligns closely with its longitudinal axis, making this non-holonomic constraint a valid and computationally efficient approximation for trajectory estimation.

Unlike the NCV model, the state transition for the CT model is non-linear due to the trigonometric relationships governing circular motion. The predicted state is calculated based on the previous state components $(p_x, p_y, v, \psi, \omega)$. For a non-zero turn rate $(\omega \neq 0)$, the position is updated as in (5) and (6):

$$p_{x,k} = p_{x,k-1} + \frac{v}{\omega}\big(sin(\psi + \omega\Delta t) - sin(\psi)\big) \tag{5}$$

$$p_{y,k} = p_{y,k-1} + \frac{v}{\omega}(-cos(\psi + \omega\Delta t) + cos(\psi)) \tag{6}$$

The yaw angle is updated linearly: $\psi_k = \psi_{k-1} + \omega \Delta t$. To be used within the EKF framework, these non-linear equations must be linearized at each time step, which is accomplished by computing the state transition Jacobian matrix, F_{CT}.

The process noise for the CT model, with covariance Q_{CT}, accounts for deviations from the ideal coordinated turn assumption. It models random fluctuations in the target's speed and variations in its turn rate, which are driven by the standard deviations σ_v and $\sigma_{\dot{\omega}}$, respectively. While the CT model significantly improves tracking performance during coordinated turns, its primary limitation is the assumption of constant speed and turn rate. This assumption is violated during aggressive or non-coordinated maneuvers, when the target simultaneously accelerates and changes its rate of turn.

- *Coordinated Turn with Rate and Acceleration (CTRA)*

The CTRA model is the most sophisticated of the three, designed to handle complex scenarios where a target executes aggressive maneuvers. It extends the CT model by incorporating linear acceleration, thus allowing it to accurately describe motions involving simultaneous changes in both speed and turn rate. The state vector is augmented with an acceleration term, a, and is defined as (7):

$$x_{CTRA} = \left[p_x, p_y, v, \psi, \dot{\psi}, a\right]^T \tag{7}$$

The state transition equations for the CTRA model are highly non-linear, as they account for the influence of both the turn rate (ω) and linear acceleration (a) on the target's position. The velocity is predicted as $v_k = v_{k-1} + a\Delta t$, while the position update incorporates the effects of this changing velocity throughout the time interval Δt. For a non-zero turn rate, this results in a complex update mechanism for the position components. As with the CT model, these non-linear dynamics are linearized at each step via a state transition Jacobian matrix, F_{CTRA}, for use within the EKF algorithm.

The process noise in the CTRA model, defined by the covariance matrix Q_{CTRA}, is critical for its adaptability. It is applied to the turn rate and acceleration states, modeling the rate of change of the turn rate and the rate of change of acceleration (jerk). These are driven by the standard deviations $\sigma_{\dot{\omega}}$ and σ_j, respectively. By accounting for these higher-order dynamics, the CTRA model overcomes the limitations of the NCV and CT models, enabling the filter to maintain high tracking accuracy even during the most challenging and dynamic phases of a target's trajectory.

- *Motion Model State Transformations*

The NCV state vector is converted to the CTRA representation to align with a different motion model that allows for more flexible dynamics. This conversion is performed using (8) for the CTRA state x_{CTRA} and (9) for the Jacobian matrix J_{CTRA}, which describes the linearized relationship between the original NCV model and the new CTRA model. This step ensures that the system's kinematic properties are accurately represented in the CTRA model, accounting for both position and velocity components.

$$x_{CTRA} = \begin{bmatrix} p_x \\ p_y \\ v = \sqrt{{v_x}^2 + {v_y}^2} \\ atan2(v_y, v_x) \\ 0 \\ 0 \end{bmatrix} \tag{8}$$

$$J_{CTRA} = \begin{bmatrix} 1 & 0 & 0 & 0 \\ 0 & 1 & 0 & 0 \\ 0 & 0 & v_x/v & v_y/v \\ 0 & 0 & -v_y/v^2 & v_x/v^2 \\ 0 & 0 & 0 & 0 \\ 0 & 0 & 0 & 0 \end{bmatrix} \tag{9}$$

The CT state vector is converted to the CTRA model by augmenting the state with zero acceleration and velocity components. As shown in (10) for x_{CTRA} and (11) for J_{CTRA}, this transformation retains the position and velocity information from the CT model while adding extra states for acceleration (set to zero). This conversion provides a more flexible model that can later represent dynamic changes in velocity or acceleration, even though they are not explicitly present in the original CT model.

$$x_{CTRA} = \begin{bmatrix} x_{CT} \\ 0 \end{bmatrix} \tag{10}$$

$$J_{CTRA} = \begin{bmatrix} I_{5\times5} \\ 0_{1\times5} \end{bmatrix} \tag{11}$$

The CTRA state vector is converted to the NCV representation to project the system's state onto a simpler motion model that describes linear motion with constant velocity. This conversion is performed using (12) for the NCV state x_{NCV} and (13) for the Jacobian matrix J_{NCV}, which captures the linearized relationship between the original CTRA model and the NCV representation. Through this transformation, the position and velocity components of the system are preserved, while higher-order dynamics such as acceleration and turn rate are omitted to align with the NCV model assumptions.

$$x_{NCV} = \begin{bmatrix} p_x \\ p_y \\ v\cos(\psi) \\ v\sin(\psi) \end{bmatrix} \tag{12}$$

$$J_{NCV} = \begin{bmatrix} 1 & 0 & 0 & 0 & 0 & 0 \\ 0 & 1 & 0 & 0 & 0 & 0 \\ 0 & 0 & \cos(\psi) & -v\sin(\psi) & 0 & 0 \\ 0 & 0 & \sin(\psi) & v\cos(\psi) & 0 & 0 \end{bmatrix} \tag{13}$$

To represent the system using a CT model, the CTRA state vector is projected onto a reduced state space that excludes acceleration. Equation (14) defines the resulting CT state x_{CT} while (15) provides the Jacobian matrix J_{CT}, which linearizes the mapping from the original CTRA model to the CT representation. This conversion preserves the system's position, velocity, heading, and turn rate, but deliberately omits the acceleration component to comply with the assumptions of the

CT model.

$$x_{CT} = x_{CTRA}(1:5) \quad (14)$$

$$J_{CT} = [I_{5\times5} \quad 0_{5\times1}] \quad (15)$$

B. IMM-EKF Algorithm

To effectively leverage the bank of motion models described previously, the IMM framework is employed. The core principle of the IMM is the parallel operation of multiple filters, each corresponding to a specific motion model. The final state estimate is then derived from a weighted fusion of the outputs from each filter, where the weights dynamically reflect how well each model describes the target's current behavior. Since the CT and CTRA models are non-linear, the EKF is utilized for their respective filtering steps, leading to the overall IMM-EKF architecture. The algorithm operates as a recursive cycle, executed at each time step, which consists of four fundamental stages: 1) Interaction/Mixing, 2) Parallel Filtering, 3) Model Probability Update, and 4) State Combination.

To facilitate a deeper understanding of the proposed method, the complete architectural flowchart of the IMM-EKF is depicted in Fig. 1. This diagram systematically visualizes the signal flow through the algorithm's four core modules within a single processing cycle. It emphasizes the parallel structure of the filtering bank, where the linear NCV model and the non-linear EKF-based CT and CTRA models operate simultaneously. Although presented as a linear flow, the diagram encapsulates the algorithm's recursive logic; the final posterior model states and probabilities (x_k, P_k, μ_k) generated at the output stage inherently serve as the requisite inputs (k−1) for the interaction step of the subsequent iteration, thereby preserving the diversity of motion modes required for robust tracking.

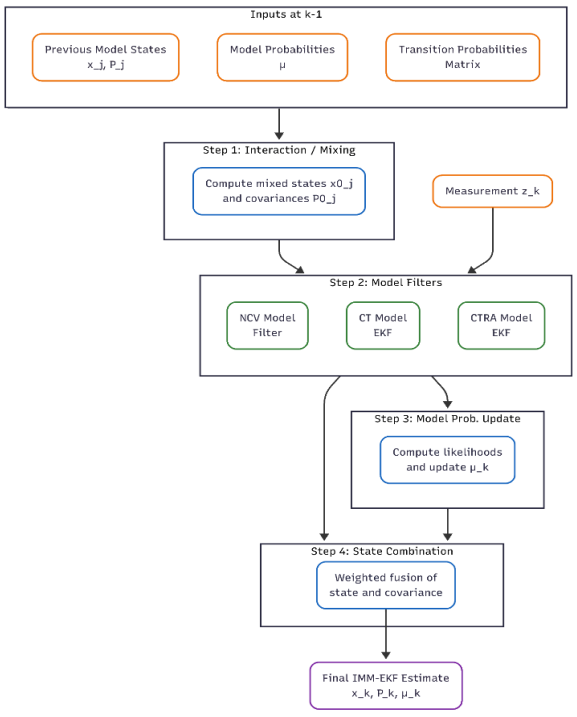

Fig. 1. Architecture of the proposed multi-model IMM-EKF tracking framework

- *Step 1: Interaction / Mixing*

The first stage in the IMM cycle is the interaction, or mixing, of the state estimates from the previous time step. The purpose of this step is to compute a mixed input for each filter based on the outputs of all filters from the prior step. This process ensures that each filter starts its prediction and update cycle with a more informed initial condition. The mixing probability, $\mu_{i|j,k-1}$, is calculated as (16):

$$\mu_{i|j,k-1} = \frac{1}{\bar{c}_j}\pi_{ij}\mu_{i,k-1} \quad (16)$$

where π_{ij} is the transition probability from model i to model j, $\mu_{i,k-1}$ is the probability of model i at the previous step, and $\bar{c}_j$ is a normalization factor.

Using these probabilities, the mixed initial state (17), $\hat{x}_{0j,k-1}$, and covariance (18), $P_{0j,k-1}$, for each filter j, are computed:

$$\hat{x}_{0j,k-1} = \sum_{i=1}^{M} \mu_{i|j,k-1}\,\hat{x}_{i,k-1} \quad (17)$$

$$P_{0j,k-1} = \sum_{i=1}^{M} \mu_{i|j,k-1}[P_{i,k-1} + (\hat{x}_{i,k-1} - \hat{x}_{0j,k-1})(\hat{x}_{i,k-1} - \hat{x}_{0j,k-1})^T] \quad (18)$$

Here, M is the total number of models. It is crucial to note that before being mixed, the state vectors $\hat{x}_{i,k-1}$ and their corresponding covariances $P_{i,k-1}$ must be transformed into the state space of the target model j. This transformation involves a change of basis and requires the calculation of a Jacobian matrix to propagate the covariance correctly.

- *Step 2: Parallel Filtering*

Following the interaction stage, each of the M filters is executed independently. Each filter j takes the mixed initial state, $\hat{x}_{0j,k-1}$, and covariance, $P_{0j,k-1}$, from the previous step as its input. It then performs a standard one-step Kalman filter (for the linear NCV model) or an EKF (for the non-linear CT and CTRA models) cycle using the current measurement, z_k. This cycle consists of a prediction step, where the state is propagated forward in time according to its specific motion model, and an update step, where this prediction is corrected based on the new measurement. For the linear NCV model, a standard Kalman Filter is used. For the non-linear CT and CTRA models, an EKF is employed.

While more advanced nonlinear filters, such as the UKF and CKF exist, which can offer superior accuracy in highly non-linear scenarios by avoiding the calculation of Jacobians [18], the EKF was deliberately chosen for this application. This decision is based on the optimal trade-off between estimation accuracy and computational efficiency.

The non-linearities present in the CT and CTRA motion models are generally smooth and mathematically tractable. Consequently, the first-order linearization used by the EKF

provides a sufficiently accurate approximation [19, 20] while maintaining a significantly lower computational footprint compared to the sigma-point propagation required by UKF or CKF. This reduced complexity is not only vital for ensuring real-time performance, but also translates directly to lower energy consumption, a critical consideration for the power-constrained embedded platforms found in autonomous vehicles [20]. Given that the EKF represents a practical, well-established benchmark with a clear algorithm structure, it was selected as the most appropriate filter for this study.

1. Prediction Step

The prediction step, also known as the time update, projects the state estimate and its uncertainty from the previous time step to the current one, based on the dynamics of the motion model. For each model j, the mixed state estimate $\hat{x}_{0j,k-1}$ is propagated through the non-linear state transition function f_j to compute the a priori state estimate, $\hat{x}_{k|k-1}^{(j)}$ (19):

$$\hat{x}_{k|k-1}^{(j)} = f_j\left(\hat{x}_{0j,k-1}\right) \tag{19}$$

To propagate the covariance, the EKF linearizes this non-linear transformation using a first-order Taylor series expansion, represented by the Jacobian matrix of the state transition function, $F_{j,k}$. The a priori covariance (20), $P_{k|k-1}^{(j)}$, is then calculated as:

$$P_{k|k-1}^{(j)} = F_{j,k}\, P_{0j,k-1} F_{j,k}^{T} + Q_j \tag{20}$$

where Q_j is the process noise covariance for model j, which accounts for the uncertainty inherent in the motion model itself.

2. Update Step

The update step, or measurement update, corrects the a priori estimate using the information from the new measurement z_k. The process begins by computing the measurement residual, or innovation, $y_k^{(j)}$, which quantifies the discrepancy between the actual measurement and the predicted measurement. The predicted measurement is obtained by mapping the a priori state into the measurement space via the non-linear measurement function h_j (21) :

$$y_k^{(j)} = z_k - h_j(\hat{x}_{k|k-1}^{(j)}) \tag{21}$$

The Kalman Gain, $K_k^{(j)}$, is then computed. This gain acts as an optimal weighting factor that minimizes the a posteriori error covariance, effectively balancing the confidence in the predicted state against the confidence in the incoming measurement. It is calculated using the innovation covariance $S_k^{(j)}$ and the linearized measurement matrix (Jacobian) $H_{j,k}$ in (22) and (23):

$$S_k^{(j)} = H_{j,k} P_{k|k-1}^{(j)} H_{j,k}^{T} + R_k \tag{22}$$

$$K_k^{(j)} = P_{k|k-1}^{(j)} H_{j,k}^{T} (S_k^{(j)})^{-1} \tag{23}$$

where R_k is the measurement noise covariance. Finally, the a priori state (24) and covariance (25) are corrected using the innovation and the Kalman Gain to yield the final a posteriori estimates for model j:

$$\hat{x}_{j,k} = \hat{x}_{k|k-1}^{(j)} + K_k^{(j)} y_k^{(j)} \tag{24}$$

$$P_{j,k} = (I - K_k^{(j)} H_{j,k}) P_{k|k-1}^{(j)} \tag{25}$$

This updated state $\hat{x}_{j,k}$ and covariance $P_{j,k}$ represent the final output of the EKF for model j at time step k.

In addition to the updated state and covariance, this filtering stage yields the likelihood of the measurement, $\Lambda_{j,k}$, a value crucial for the model probability update that follows.

- *Step 3: Model Probability Update*

After each filter has processed the latest measurement, the probability of each motion model, $\mu_{j,k}$, is updated to reflect its performance. This update is based on how well each model's prediction matched the actual measurement, a quantity captured by the model-specific likelihood (26), $\Lambda_{j,k}$. The likelihood is calculated using the multivariate Gaussian probability density function of the measurement residual, $y_{j,k}$, with respect to its covariance, $s_{j,k}$:

$$\Lambda_{j,k} = N\left(y_{j,k}; 0, s_{j,k}\right) \tag{26}$$

A higher likelihood value indicates a better fit between the model's prediction and the measurement.

The model probabilities are then updated using a Bayesian framework. The posterior probability of each model j is proportional to its prior probability (the predicted probability, $\bar{c}_j$, from the interaction step) multiplied by its calculated likelihood. The final updated probability (27), $\mu_{j,k}$, is found by normalizing these values:

$$\mu_{j,k} = \frac{\Lambda_{j,k}\bar{c}_j}{\sum_{i=1}^{M} \Lambda_{j,k}\bar{c}_i} \tag{27}$$

This mechanism ensures that models that more accurately describe the target's current dynamics are assigned a higher probability, thereby giving them more influence in the final state estimation.

- *Step 4: State Combination*

The final stage of the IMM cycle is the combination, or fusion, of the state estimates and covariances produced by the individual filters. This step generates a single, comprehensive state estimate that represents the overall output of the IMM filter at the current time step. The combined state (28), $\hat{x}_k$, is computed as a weighted average of the posterior state estimates from each filter, where the weights are the updated model probabilities, $\mu_{j,k}$:

$$\hat{x}_k = \sum_{j=1}^{M} \mu_{j,k}\, \hat{x}_{j,k} \tag{28}$$

Similarly, the overall covariance (29), P_k, is computed by combining the covariances from each filter. This calculation not only includes a weighted sum of the individual posterior covariances but also incorporates a term that accounts for the spread among the different state estimates, thereby providing a more accurate representation of the total uncertainty:

$$P_k = \sum_{j=1}^{M} \mu_{j,k}[P_{j,k} + (\hat{x}_{j,k} - \hat{x}_k)(\hat{x}_{j,k} - \hat{x}_k)^T] \tag{29}$$

Before this fusion, it is essential that all state estimates and covariances, which may exist in different state spaces (e.g., NCV vs. CTRA), are transformed into a common reference frame. The resulting combined state $\hat{x}_k$ and covariance P_k are the final outputs for the time step k and serve as the inputs for the interaction stage of the next cycle.

III. Experimental Setup

To evaluate the proposed algorithm, a simulation was conducted under conditions designed to emulate a real-world application. It is critical to note that the filter was not provided with the ground truth data directly. To simulate a realistic sensor measurement process, the measurement vector z_k at each time step was generated by corrupting the true position and velocity data with zero-mean Gaussian noise. The standard deviations of this noise, σ_p and $\sigma_{v,meas}$, are detailed in the Filter Parameters section

A. Dataset

The dataset used for evaluating the filter performance was synthetically generated using the Driving Scenario Designer toolbox in MATLAB. This approach enabled the generation of a precise ground truth trajectory, which was then exported as a CSV file. The scenario was specifically designed to encompass a diverse range of dynamic behaviors representative of real-world driving conditions. The trajectory includes straight-line segments, gentle S-curves, and sharp turns. In addition to the primary state variables, the ground truth yaw angle (ψ), required for calculating the Yaw RMSE, was derived from the true velocity components (v_x, v_y) using the standard four-quadrant arctangent function.

Furthermore, the ego vehicle's speed profile is intentionally dynamic and context-aware. It realistically simulates higher speeds on straight sections, followed by the necessary decelerations for navigating these turns. This combination of linear and highly non-linear motion, coupled with variable acceleration, provides a challenging and comprehensive test case for validating the adaptive capabilities of the proposed IMM-EKF.

B. Filter Parameters

The performance of the IMM-EKF tracker is critically dependent on the careful selection of its core parameters. These values define the filter's underlying assumptions about the target's motion dynamics (process noise), the sensor's precision (measurement noise), and the probability of transitioning between different behaviors (Transition Probability Matrix). The parameters used in this study were determined based on domain knowledge of typical vehicle dynamics and refined through empirical tuning to achieve optimal performance on the test dataset. The key parameters are summarized in Table I.

TABLE I
Configuration Parameters for the Proposed IMM-EKF Tracker

Category	Parameter	Symbol	Value
IMM Framework	Transition Probability Matrix (TPM)	Π	$\begin{bmatrix} 0.90 & 0.05 & 0.05 \\ 0.05 & 0.90 & 0.05 \\ 0.05 & 0.05 & 0.90 \end{bmatrix}$
	Initial Model Probabilities	μ_0	$[0.90 \quad 0.08 \quad 0.02]^T$
Process Noise	NCV Process Noise Std. Dev.	σ_q	0.6 m/s^2
	CT Speed Noise Std. Dev.	$\sigma_{v,ct}$	2.4 m/s^2
	CT Turn Rate Noise Std. Dev.	$\sigma_{\dot{\omega},ct}$	0.6 rad/s^2
	CTRA Jerk Noise Std. Dev.	σ_j	20.0 m/s^3
	CTRA Turn Rate Noise Std. Dev.	$\sigma_{\dot{\omega},ctra}$	3.0 rad/s^2
Measurement Noise	Position Measurement Std. Dev.	σ_p	0.5 m
	Velocity Measurement Std. Dev.	$\sigma_{v,meas}$	0.5 m/s

The TPM is chosen to be diagonally dominant, reflecting the high likelihood that the target will remain in its current motion state rather than abruptly switching at any given time step. The off-diagonal transition probabilities are set uniformly to 0.05. This uniformity reflects an uninformative prior assumption regarding specific maneuver transitions, since—without map information or knowledge of driver intent—there is no statistical basis to assume that a transition from NCV to CT is more or less likely than a transition to CTRA. Therefore, equal off-diagonal probabilities ensure that the filter remains unbiased and equally responsive to any potential change in dynamics, while still maintaining sensitivity to possible maneuvers.

Furthermore, the initial model probabilities are set with a strong bias toward the NCV model, based on the logical assumption that the vehicle begins its trajectory in a relatively stable, non-maneuvering state. The process and measurement noise parameters have been tuned to achieve a balance between tracking accuracy and filter robustness, enabling the more complex models to react effectively to maneuvers without introducing excessive noise into the final state estimates.

For reproducibility, the filter initialization details are as

follows: The state vectors are initialized using the first ground truth data point to isolate the tracking performance from initial transient errors. The initial error covariance matrices (P_0) are set diagonally. For the NCV model, $P_{0,NCV} = diag(0.5,0.5,1.0,1.0)$. For the CT model, $P_{0,CT} = diag(0.5,0.5,1.0,0.1,0.2)$. For the CTRA model, $P_{0,CTRA} = diag(0.5,0.5,1.0,0.1,0.2,1.0)$. Furthermore, the process noise covariance matrix Q_{NCV} is implemented using the discrete white noise acceleration model, incorporating terms of $\Delta t^3/3$ and $\Delta t^2/2$."

C. Evaluation Metrics

To rigorously assess the performance of the proposed IMM-EKF tracker, a comprehensive set of evaluation metrics is employed. These metrics are categorized into two groups: accuracy metrics, which quantify the closeness of the estimated trajectory to the ground truth, and consistency metrics, which evaluate the statistical validity of the filter's own uncertainty estimates.

- Root Mean Square Error (RMSE)

This is the primary metric for evaluating the overall tracking error. It is calculated for position, velocity, and yaw. For a total of N time steps, the position RMSE is defined as (30):

$$RMSE_{pos} = \sqrt{\frac{1}{N}\sum_{k=1}^{N}\left(p_{x,k} - \hat{p}_{x,k}\right)^2 + \left(p_{y,k} - \hat{p}_{y,k}\right)^2} \quad (30)$$

where (p_x, p_y) is the true position and $(\hat{p}_x, \hat{p}_y)$ is the estimated position.

- Mean Absolute Error (MAE)

This metric (31) measures the average magnitude of position errors and is less sensitive to large, infrequent outliers compared to RMSE.

$$MAE_{pos} = \frac{1}{N}\sum_{k=1}^{N}\sqrt{\left(p_{x,k} - \hat{p}_{x,k}\right)^2 + \left(p_{y,k} - \hat{p}_{y,k}\right)^2} \quad (31)$$

- Final Displacement Error (FDE)

This metric measures the position error at the final time step of the trajectory, providing insight into the long-term drift of the tracker (32).

$$FDE = \sqrt{\left(p_{x,N} - \hat{p}_{x,N}\right)^2 + \left(p_{y,N} - \hat{p}_{y,N}\right)^2} \quad (32)$$

- Normalized Innovation Squared (NIS)

The NIS test evaluates whether the measurement residual (innovation) is consistent with its theoretical covariance. For a measurement of dimension m, the NIS value is calculated as (33):

$$\epsilon_{NIS,k} = y_k^T S_k^{-1} y_k \quad (33)$$

where y_k is the innovation and S_k is its covariance. Under the assumption of a correct model, the NIS values follow a Chi-squared (χ^2) distribution with m degrees of freedom.

- Normalized Estimation Error Squared (NEES)

The NEES test assesses the consistency of the state estimate itself by measuring the squared Mahalanobis distance between the estimated and true states. For a state vector of dimension n, the NEES is given by (34):

$$\epsilon_{NEES,k} = (x_k - \hat{x}_k)^T P_k^{-1} (x_k - \hat{x}_k) \quad (34)$$

where $(x_k - \hat{x}_k)$ is the true state error and P_k is the estimated state covariance. Similar to NIS, the NEES values should follow a χ^2 distribution with n degrees of freedom for a consistent filter.

IV. Results and Analysis

This section presents a comprehensive evaluation of the proposed IMM-EKF tracker by applying it to the synthetically generated trajectory described in the experimental setup. The analysis is structured to provide a multifaceted assessment of the filter's performance. It begins with a qualitative comparison of the estimated trajectory against the ground truth, followed by an in-depth analysis of the IMM framework's core adaptive mechanism—the dynamic evolution of model probabilities in response to target maneuvers. Subsequently, a detailed quantitative analysis of tracking accuracy is conducted by examining the position, velocity, and yaw errors over time. Finally, the statistical consistency of the filter is rigorously validated using the NIS and NEES tests to ensure the reliability of the filter's uncertainty estimates. Collectively, these results demonstrate the robustness and accuracy of the proposed multi-model approach for tracking maneuvering targets.

Fig. 2 presents a visual comparison between the ground-truth trajectory and the path estimated by the proposed IMM-EKF tracker. The true path is depicted by a solid blue line, while the filter's estimate is shown as a dashed red line. The scenario is designed to be challenging, encompassing straight sections, a gentle S-curve, and two sharp 90-degree turns.

A qualitative inspection of the results reveals an exceptionally close correspondence between the estimated and true paths throughout the entire trajectory. This visual evidence is strongly supported by quantitative metrics, with the overall Position RMSE calculated at only 0.3117 m. The tracker demonstrates remarkable robustness, accurately following the target through both the linear motion segments and the highly dynamic maneuvering phases. The minimal deviation, even during the sharp turns where motion models are most likely to fail, highlights the effectiveness of the adaptive IMM framework. In summary, Fig. 2 provides compelling evidence for the high accuracy and stability of the proposed algorithm.

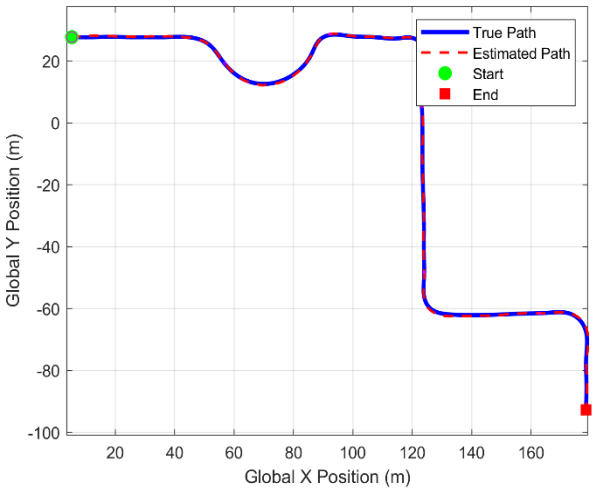

Fig. 2. Comparison of the estimated trajectory (dashed red line) from the IMM-EKF tracker against the ground truth path (solid blue line), demonstrating a high degree of tracking accuracy.

The IMM framework's dynamic adaptation is illustrated in Fig. 3, plotting each model's posterior probability over time. A model's probability increases when its predictions align with sensor measurements, indicating that it best describes the target's current behavior. Following an initial transient phase where the models fluctuate, the NCV model (blue) dominates during the stable straight segments.

Crucially, during complex maneuvers such as the S-curve and the transitional phases entering or exiting turns, transient spikes in the CTRA model's probability (red) demonstrate its essential role in capturing the complex dynamics involving simultaneous changes in speed and turn rate. Conversely, the CT model (green) becomes dominant during periods of sustained turning, such as the steady phases of 90-degree corners. This logical transition of probabilities between models is the fundamental mechanism enabling the IMM-EKF's superior tracking accuracy across the challenging trajectory.

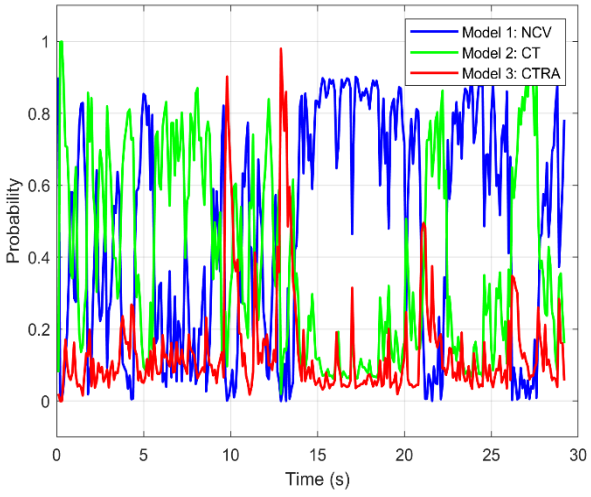

Fig. 3. Time evolution of the model probabilities for the NCV, CT, and CTRA models, illustrating the adaptive weighting mechanism of the IMM-EKF in response to target maneuvers.

A quantitative analysis of the filter's accuracy is provided in Fig. 4, which illustrates the magnitude of the position error over the duration of the trajectory. The error remains well-bounded throughout the entire run, with no evidence of divergence, which confirms the stability of the filter. The peaks observed in the error profile, such as the one around 22 seconds, are associated with the most challenging maneuvers in the trajectory (e.g., sharp turns). These temporary increases in error are expected as the filter adapts its model probabilities in response to abrupt changes in the target dynamics.

Despite these transient peaks, the tracker rapidly reconverges, keeping the error at a consistently low level. The visual data is supported by the overall performance metrics, which show a Maximum Position Error of 0.6722 m—aligning with the highest peak in the figure—and a Position RMSE of only 0.3117 m. The consistently low error magnitude across a trajectory with diverse dynamics underscores the tracker's high precision and its effective use of the multi-model framework to mitigate errors during maneuvers.

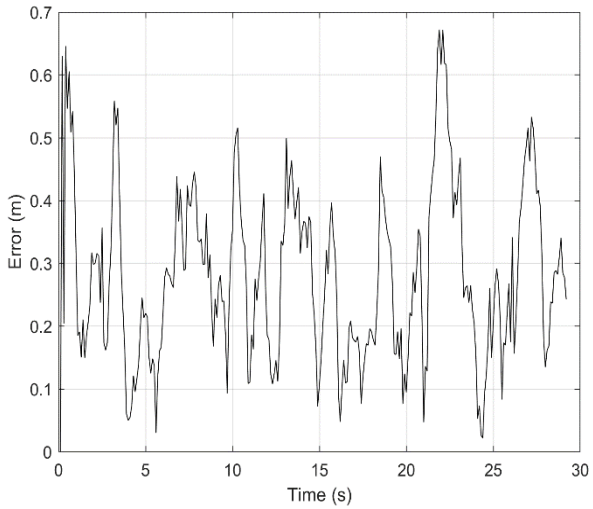

Fig. 4. Position error magnitude of the IMM-EKF tracker over time, demonstrating the filter's stability and high accuracy.

The analysis is extended to kinematic states beyond position in Fig. 5, which compares the true target speed with the IMM-EKF-estimated speed. The figure clearly shows that the estimated speed (dashed red line) accurately tracks the true speed profile (solid blue line) through all its dynamic variations.

The filter demonstrates a high degree of responsiveness, successfully capturing the initial sharp deceleration, the subsequent periods of acceleration and deceleration corresponding to maneuvers, and the final acceleration at the end of the trajectory. The minor oscillations observed in the estimated speed are an inherent artifact of the filtering process, resulting from the continual state update under measurement noise. The excellent tracking performance is quantitatively confirmed by a low Velocity RMSE of 0.5428 m/s. This result validates the effectiveness of including the CTRA model, which explicitly accounts for linear acceleration, enabling the filter to accurately estimate the target's speed profile even during aggressive maneuvers.

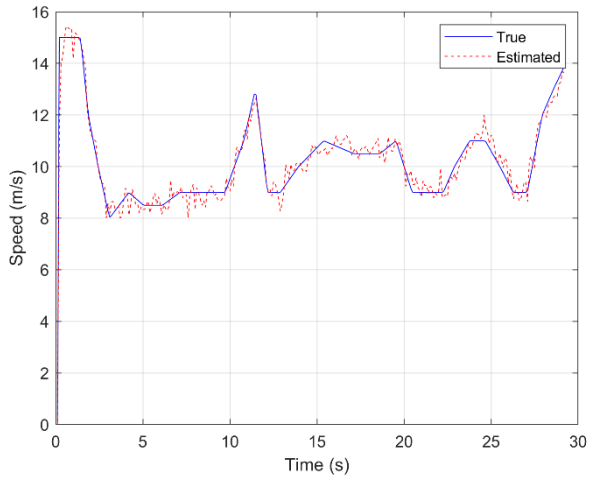

Fig. 5. Comparison of the true and estimated target speed over time, demonstrating the filter's ability to accurately track dynamic changes, including accelerations and decelerations.

Fig. 6 evaluates the filter's performance in estimating the target's orientation by comparing the true yaw (heading) angle with the estimated value. The plot demonstrates very high degree of accuracy, with the estimated heading (dashed red line) closely overlaying the true heading (solid blue line) throughout the entire scenario.

The filter successfully tracks both slow and rapid changes in the target's orientation. Most notably, it accurately captures the large, sweeping changes in yaw corresponding to the sharp 90-degree turns, where the heading changes by approximately 90 degrees in a short time frame. Accurate heading estimation is critical for maneuver recognition and short-term path prediction. The filter's ability to perform well in this regard highlights the effectiveness of the turn-based models (CT and CTRA). This visual assessment is quantitatively substantiated by a very low Yaw RMSE of 2.1614 degrees, confirming that the IMM-EKF provides a reliable and precise estimate of the target's heading, even during aggressive maneuvering.

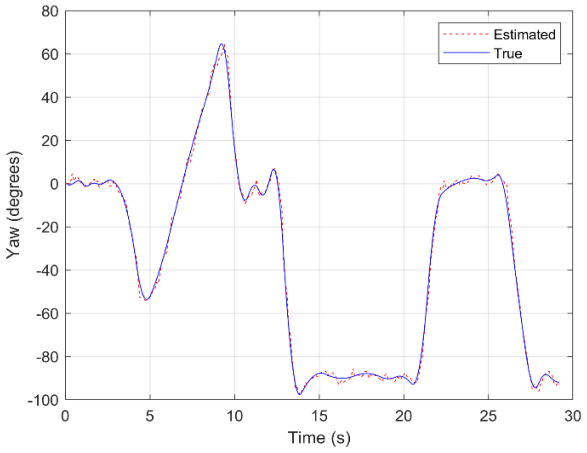

Fig. 6. Comparison of the true and estimated target yaw (heading) over time, highlighting the filter's high fidelity in tracking orientation during maneuvers.

To provide a more granular view of the tracking performance, Fig. 7 decomposes the total position error into its individual Cartesian components along the X and Y axes. Both subplots show that the estimation errors are zero-mean, indicating that the filter is unbiased and does not exhibit any systematic drift in either direction.

The magnitude of the error in both the X and Y components remains well-bounded within approximately ± 0.5 meters for the entire duration. The fluctuations in the error signals are directly correlated with the target's dynamics; larger oscillations are observed during maneuvering periods, while the error tends to be smaller and more stable during straight-line motion. This detailed breakdown confirms that the low overall position error, as previously reported by the RMSE, is not masking poor performance in one dimension with a strong performance in another. Instead, the IMM-EKF demonstrates consistent and robust tracking accuracy in both axes independently, further validating the stability and precision of the estimation process.

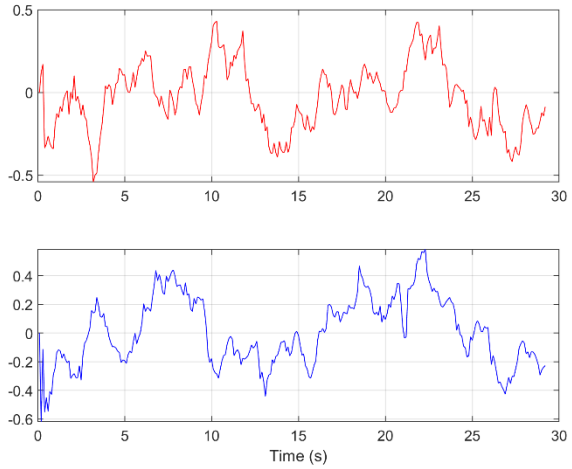

Fig. 7. Position error components along the X-axis (top) and Y-axis (bottom) over time, showing the unbiased and well-bounded nature of the state estimation.

Beyond tracking accuracy, it is crucial to validate the statistical consistency of the filter. Fig. 8 presents the results of the NIS test, which assesses whether the filter's model for measurement uncertainty is accurate. The plot displays the calculated NIS values at each time step against the 95% confidence bound (dashed red line). This bound is derived from a Chi-squared (χ^2) distribution with 4 degrees of freedom, corresponding to the four-dimensional measurement vector (position and velocity).

For a well-tuned and statistically consistent filter, approximately 95% of the NIS values are expected to fall below this confidence threshold. The results show excellent adherence to this condition, with the vast majority of points lying within the valid region. This visual assessment is quantitatively confirmed by the fact that 94.16% of the NIS values are within the 95% confidence interval, a figure remarkably close to the theoretical target. Furthermore, the average NIS value across the trajectory is 4.3941, which is very close to the theoretical mean of 4 for a χ^2 distribution with 4 degrees of freedom. These results collectively confirm that the filter is not over- or underconfident in its predictions and that its innovation covariance is a statistically sound representation of the true measurement uncertainty.

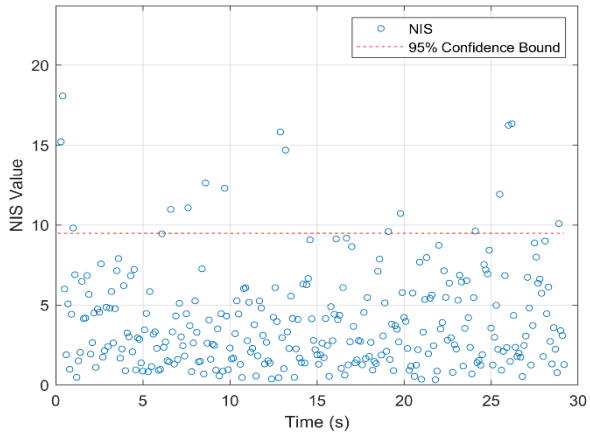

Fig. 8. NIS consistency test results, with NIS values (blue circles) plotted against the 95% confidence bound (dashed red line), confirming the statistical consistency of the filter's measurement uncertainty model.

The final validation step involves the NEES test, which directly assesses the consistency of the filter's state covariance matrix, P_k. Fig. 9 plots the NEES values for the four-dimensional Cartesian state (position and velocity) against the theoretical 95% confidence bound from a χ^2 distribution with 4 degrees of freedom. This test is critical as it confirms whether the filter's own uncertainty estimate is a reliable measure of the true state error.

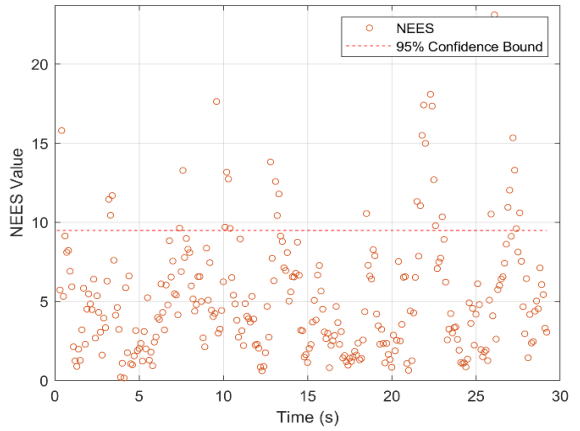

Fig. 9. NEES consistency test results for the 4-DOF Cartesian state. The NEES values (orange circles) are shown against the 95% confidence bound, validating the statistical consistency of the filter's state covariance matrix.

While the observed NEES consistency of 87.29% is below the theoretical 95% confidence level, this deviation arises from several intrinsic factors associated with the filtering process. During aggressive maneuvers or sudden changes in target dynamics, temporary mismatches between the assumed motion models and the actual system behavior can produce transient underestimation or overestimation of the state uncertainty. In addition, NEES is highly sensitive to finite sample effects and the stochastic properties of both process and measurement noise; limited trajectory length, abrupt state transitions, and random fluctuations in measurements naturally introduce variability in NEES values. Model simplifications, such as linearization approximations in the EKF and the finite set of motion models in the IMM framework, can also contribute to the underestimation of uncertainty during highly nonlinear or rapidly changing scenarios. To reduce such deviations, careful selection of model sets, inclusion of more representative motion models, and increasing the effective sample size through longer trajectories or repeated simulations can help stabilize NEES consistency and better align the estimated uncertainty with actual state errors. Despite the observed deviation, the average NEES of 5.5006, reasonably close to the theoretical mean of 4, along with consistent NIS results, confirms that the IMM-EKF provides reliable covariance estimates and maintains a statistically meaningful relationship between estimated uncertainty and actual state error.

Collectively, the analysis presented in Figs 2 through 9 confirms that the proposed IMM-EKF tracker provides a highly accurate, robust, and statistically consistent solution for maneuvering target tracking. The results have demonstrated the filter's capability to maintain low estimation errors while correctly adapting its internal models to the target's dynamics. To provide a concise, holistic view of the tracker's performance, the key quantitative metrics are consolidated and presented in Tables II and III. Table II summarizes the positional estimation accuracy metrics, including RMSE, MAE, and FDE. Meanwhile, Table III covers the wider estimation performance and consistency, detailing velocity error, yaw accuracy, and statistical tests (NEES and NIS). These tables numerically substantiate the qualitative findings from the graphical analysis.

TABLE II
Summary of Positional Estimation Accuracy Metrics

Pos. RMSE (m)	Pos. MAE (m)	Max Pos. Err (m)	FDE (m)
0.3117	0.2794	0.6722	0.2429

TABLE III
Estimation Performance and Consistency

Vel. RMSE (m/s)	Yaw RMSE (deg)	NEES. Cons (%)	NIS. Cons (%)
0.5428	2.1614	87.29	94.16

V. Conclusion and Future Work

This paper presented a robust and adaptive solution for tracking maneuvering targets using an IMM-EKF. By synergistically combining three distinct kinematic models — NCV, CT, and CTRA — the proposed filter demonstrated a remarkable ability to accurately estimate a target's trajectory across a wide range of dynamic behaviors. The effectiveness of the algorithm was rigorously validated on a challenging, synthetically generated dataset that included straight-line motion, sustained turns, and aggressive maneuvers.

The experimental results confirmed the high performance of the tracker, achieving a very low Position RMSE of 0.3117 m and Yaw RMSE of 2.1614 degrees. The analysis of the model probabilities showcased the filter's core adaptive mechanism, which correctly inferred the target's motion mode in real-time. Furthermore, the filter's statistical consistency was successfully

verified through NIS and NEES tests, with an NIS consistency of 94.16%, confirming that the filter's uncertainty estimates are both reliable and statistically sound. In summary, this work validates the IMM-EKF as a highly effective and reliable framework for high-precision trajectory estimation.

While the proposed method has shown excellent results, several avenues for future investigation exist. The EKF can be susceptible to errors from linearization, especially in highly nonlinear systems. Future work could involve replacing the EKF with more advanced non-linear filters, such as the UKF [21] or a Particle Filter [22], which may offer improved accuracy during very aggressive maneuvers. The process and measurement noise covariances were hand-tuned. A significant enhancement would be to implement an adaptive noise estimation algorithm that can adjust these matrices online, making the filter more robust to varying sensor conditions and target behaviors. The current study was based on a synthetic dataset. The next logical step is to validate the algorithm's performance using real-world data collected from sensors such as GPS, IMU, and LiDAR to assess its effectiveness in practical, real-world scenarios.

Funding Statement

This research did not receive any specific grant from funding agencies in the public, commercial, or not-for-profit sectors.

Conflicts of Interest

The author declares that there is no conflict of interest regarding the publication of this article.

STATEMENT ON THE USE OF GENERATIVE AI

Gemini was used for language editing and clarity enhancement.

References

[1] S. Zargari, A. Jarrah, and F. Baghbani, "Fuzzy-based driver monitoring system to assess dangerous driving on roads," *Traffic Injury Prevention*, pp. 1-10, 2025, doi: 10.1080/15389588.2025.2539923.

[2] S. Zargari, A. Jarrah, and F. Baghbani, "Video-based Facial Expression Recognition Using DensNet121 and LSTM," in *The First Conference on Artificial Intelligence and Intelligent Processing*, 2022.

[3] D.-J. Jwo, J.-H. Lai, and Y. Chang, "Interacting multiple model filter with a maximum correntropy criterion for gps navigation processing," *Applied Sciences*, vol. 13, no. 3, p. 1782, 2023, doi: 10.3390/app13031782.

[4] S. A. Gadsden, S. R. Habibi, and T. Kirubarajan, "A novel interacting multiple model method for nonlinear target tracking," in *2010 13th International Conference on Information Fusion*, 2010: IEEE, pp. 1-8, doi: 10.1109/ICIF.2010.5712021.

[5] S. M. Aly, R. El Fouly, and H. Braka, "Extended Kalman filtering and interacting multiple model for tracking maneuvering targets in sensor networks," in *2009 Seventh Workshop on Intelligent solutions in Embedded Systems*, 2009: IEEE, pp. 149-156.

[6] W. Zhu, W. Wang, and G. Yuan, "An improved interacting multiple model filtering algorithm based on the cubature Kalman filter for maneuvering target tracking," *Sensors*, vol. 16, no. 6, p. 805, 2016, doi: 10.3390/s16060805.

[7] L. Gao, J. Xing, Z. Ma, J. Sha, and X. Meng, "Improved IMM algorithm for nonlinear maneuvering target tracking," *Procedia Engineering*, vol. 29, pp. 4117-4123, 2012, doi: 10.1016/j.proeng.2012.01.630.

[8] W. Li and Y. Jia, "Location of mobile station with maneuvers using an IMM-based cubature Kalman filter," *IEEE Transactions on Industrial Electronics*, vol. 59, no. 11, pp. 4338-4348, 2011, doi: 10.1109/TIE.2011.2180270.

[9] M. Wan, P. Li, and T. Li, "Tracking maneuvering target with angle-only measurements using IMM algorithm based on CKF," in *2010 International Conference on Communications and Mobile Computing*, 2010, vol. 3: IEEE, pp. 92-96, doi: 10.1109/CMC.2010.239.

[10] K. Vedula, M. L. Weiss, R. C. Paffenroth, J. R. Uzarski, and D. R. Brown, "Maneuvering target tracking using the autoencoder-interacting multiple model filter," in *2020 54th Asilomar Conference on Signals, Systems, and Computers*, 2020: IEEE, pp. 1512-1517, doi: 10.1109/IEEECONF51394.2020.9443396.

[11] M. Ebrahimi, M. Ardeshiri, and S. A. Khanghah, "Bearing-only 2D maneuvering target tracking using smart interacting multiple model filter," *Digital Signal Processing*, vol. 126, p. 103497, 2022, doi: 10.1016/j.dsp.2022.103497.

[12] X. Liu *et al.*, "IMM-MOT: A Novel 3D Multi-object Tracking Framework with Interacting Multiple Model Filter," *arXiv preprint arXiv:2502.09672*, 2025, doi: 10.48550/arXiv.2502.09672.

[13] J. Wang, X. Wang, Y. Chen, M. Yan, and H. Lan, "Model Adaptive Kalman Filter for Maneuvering Target Tracking Based on Variational Inference," *Electronics*, vol. 14, no. 10, p. 1908, 2025, doi: 10.3390/electronics14101908.

[14] Y. Dong, W. Li, D. Li, C. Liu, and W. Xue, "Intelligent Tracking Method for Aerial Maneuvering Target Based on Unscented Kalman Filter," *Remote Sensing*, vol. 16, no. 17, p. 3301, 2024, doi: 10.3390/rs16173301.

[15] J. Huang, J. Xie, H. Zhai, Z. Li, and W. Feng, "An Adaptive Constant Acceleration Model for Maneuvering Target Tracking," *Remote Sensing*, vol. 17, no. 5, p. 850, 2025, doi: 10.3390/rs17050850.

[16] S. Wang, R. Li, C. Men, Y. Cao, and T.-S. Yeo, "Adaptive IMM Algorithm Based on Variational Inference for Multiple Maneuvering Extended Targets Tracking," *Advances in Astronautics*, pp. 1-15, 2025, doi: 10.1007/s42423-025-00173-7.

[17] H. A. Blom and Y. Bar-Shalom, "The interacting multiple model algorithm for systems with Markovian switching coefficients," *IEEE Transactions on Automatic Control*, vol. 33, no. 8, pp. 780-783, 2002, doi: 10.1109/9.1299.

[18] E. A. Wan and R. Van Der Merwe, "The unscented Kalman filter for nonlinear estimation," in *Proceedings of the IEEE 2000 adaptive systems for signal processing, communications, and control symposium (Cat. No. 00EX373)*, 2000: IEEE, pp. 153-158, doi: 10.1109/ASSPCC.2000.882463.

[19] J. J. LaViola, "A comparison of unscented and extended Kalman filtering for estimating quaternion motion," in *Proceedings of the 2003 American Control Conference, 2003.*, 2003, vol. 3: IEEE, pp. 2435-2440, doi: 10.1109/ACC.2003.1243440.

[20] A. Valade, P. Acco, P. Grabolosa, and J.-Y. Fourniols, "A study about Kalman filters applied to embedded sensors," *Sensors*, vol. 17, no. 12, p. 2810, 2017, doi: 10.3390/s17122810.

[21] S. J. Julier and J. K. Uhlmann, "New extension of the Kalman filter to nonlinear systems," in *Signal processing, sensor fusion, and target recognition VI*, 1997, vol. 3068: Spie, pp. 182-193, doi: 10.1117/12.280797.

[22] N. J. Gordon, D. J. Salmond, and A. F. Smith, "Novel approach to nonlinear/non-Gaussian Bayesian state estimation," in *IEE proceedings F (radar and signal processing)*, 1993, vol. 140, no. 2: IET, pp. 107-113, doi: 10.1049/ip-f-2.1993.0015.

Biographies

Alireza Jarrah received his B.Sc. degree (with Honors) in Electrical Engineering (Control) from Semnan University, Semnan, Iran, in 2023. He is currently pursuing his M.Sc. in Electrical Engineering (Control) at Shahid Beheshti University (SBU), Tehran, Iran. His research interests include autonomous vehicles, fuzzy systems, and artificial intelligence.

Hadi Asharioun is a faculty member at Shahid Beheshti University (SBU) in Tehran, Iran. He earned his B.Sc. from Sharif University of Technology and his M.Sc. from Iran University of Science and Technology. In 2014, he received his Ph.D. from Universiti Sains Malaysia, Pulau Pinang, Malaysia. His research interests include computer and industrial networks, the Internet of Things, artificial intelligence, machine learning, and wireless sensor networks.

Mohammadhossein Hashemi is currently a Ph.D. student in Electrical Engineering (Control) at Shahid Beheshti University (SBU), Tehran, Iran. He received his M.Sc. in Electrical Engineering (Control) and his B.Sc. in Computer Engineering, both from Shahid Beheshti University. His research interests include observer design.